



HHS Public Access

Author manuscript

Prog Retin Eye Res. Author manuscript; available in PMC 2018 July 01.

Published in final edited form as:

Prog Retin Eye Res. 2017 July ; 59: 1–52. doi:10.1016/j.preteyeres.2017.03.001.

The Connective Tissue Phenotype of Glaucomatous Cupping in the Monkey Eye - Clinical and Research Implications

Hongli Yang^{a,b}, Juan Reynaud^{a,b}, Howard Lockwood^{a,b}, Galen Williams^{a,b}, Christy Hardin^{a,b}, Luke Reyes^{a,b}, Cheri Stowell^{a,b}, Stuart K. Gardiner^b, and Claude F. Burgoyne, MD^{a,b}

^aDevers Eye Institute, Optic Nerve Head Research Laboratory, Legacy Research Institute, Portland, Oregon

^bDevers Eye Institute, Discoveries in Sight Research Laboratories, Legacy Research Institute, Portland, Oregon

Abstract

In a series of previous publications we have proposed a framework for conceptualizing the optic nerve head (ONH) as a biomechanical structure. That framework proposes important roles for intraocular pressure (IOP), IOP-related stress and strain, cerebrospinal fluid pressure (CSFp), systemic and ocular determinants of blood flow, inflammation, auto-immunity, genetics, and other non-IOP related risk factors in the physiology of ONH aging and the pathophysiology of glaucomatous damage to the ONH. The present report summarizes 20 years of technique development and study results pertinent to the characterization of ONH connective tissue deformation and remodeling in the unilateral monkey experimental glaucoma (EG) model. In it we propose that the defining pathophysiology of a glaucomatous optic neuropathy involves deformation, remodeling, and mechanical failure of the ONH connective tissues. We view this as an active process, driven by astrocyte, microglial, fibroblast and oligodendrocyte mechanobiology. These cells, and the connective tissue phenomena they propagate, have primary and secondary effects on retinal ganglion cell (RGC) axon and lamellar beam and retrolaminar capillary homeostasis that may initially be “protective” but eventually lead to RGC axonal injury, repair and/or cell death. The primary goal of this report is to summarize our 3D histomorphometric and optical coherence tomography (OCT)-based evidence for the early onset and progression of ONH connective tissue deformation and remodeling in monkey EG. A second goal is to explain the importance of including ONH connective tissue processes in characterizing the phenotype of a glaucomatous optic neuropathy in all species. A third goal is to summarize our current efforts to move from ONH morphology to the cell biology of connective tissue remodeling and axonal insult early in the disease. A final goal is to facilitate the translation of our findings and ideas into neuroprotective interventions that target these ONH phenomena for therapeutic effect.

Corresponding Author: Claude F. Burgoyne, MD, cfburgoyne@deverseye.org, Address: Optic Nerve Head Research Laboratory, Devers Eye Institute, Legacy Research Institute, 1225, NE 2nd Ave, Portland OR 97232.

Publisher's Disclaimer: This is a PDF file of an unedited manuscript that has been accepted for publication. As a service to our customers we are providing this early version of the manuscript. The manuscript will undergo copyediting, typesetting, and review of the resulting proof before it is published in its final form. Please note that during the production process errors may be discovered which could affect the content, and all legal disclaimers that apply to the journal pertain.

Keywords

glaucoma; optic nerve head; lamina cribrosa; monkey; astrocyte

1.0 Introduction

1.1 Background and Goals

While glaucomatous damage to the visual system likely includes pathophysiologies within the retinal photoreceptors (Janssen et al., 1996; Kendell et al., 1995; Nork et al., 2000; Panda and Jonas, 1992; Wygnanski et al., 1995), retinal ganglion cell (RGC) soma (Asai et al., 1987; Garcia-Valenzuela et al., 1995; Quigley, 1995a; Quigley et al., 2000; Quigley et al., 1995; Weber et al., 1998), distal RGC axon (Crish et al., 2010), and lateral geniculate/superior colliculus (Crish and Calkins, 2015; Crish et al., 2013; Crish et al., 2010; Yucel et al., 2000; Yucel et al., 2001, 2003), and visual cortex (Yucel et al., 2003), extensive evidence from ourselves (Bellezza et al., 2003b; Burgoyne et al., 2004; Downs et al., 2007; Roberts et al., 2009; Yang et al., 2007a; Yang et al., 2007b; Yang et al., 2011a; Yang et al., 2011b) and others (Gaasterland et al., 1978; Minckler et al., 1977; Quigley et al., 1981; Quigley and Green, 1979) suggests that damage to the RGC axons within the lamina cribrosa (LC) of the optic nerve head (ONH) is an early pathophysiology underlying glaucomatous neuronal loss in mice, rats, monkeys and humans (Danas et al., 2003; Filippopoulos et al., 2006; Howell et al., 2007; Jakobs et al., 2005; Johansson, 1983; Johnson et al., 2000; Johnson et al., 2007; Johnson et al., 1996; Nguyen et al., 2011; Schlamp et al., 2006; Soto et al., 2011).

However, while RGC axonal insult within the ONH is central to glaucomatous vision loss and its manifestations are the source of all current forms of clinical staging (visual field, retinal nerve fiber layer (RNFL) thickness, etc.), we propose that RGC axonal insult within the ONH is not the pathophysiology that defines the optic neuropathy of glaucoma. In making this statement, we acknowledge the essential need to preserve RGC axons, soma and their peripheral connections in all glaucoma patients, because preservation of vision is the goal of all glaucoma therapy. However, we also emphasize that, to date, selectively killing RGC soma or axons alone, by whatever mechanism, has not been shown to create a glaucomatous optic neuropathy (i.e. glaucomatous ONH cupping) (Brooks et al., 2004; Chauhan et al., 2004; Ing et al., 2016; Joachim et al., 2013; Wax et al., 2008; Yang et al., 2014a).

In this context, we propose that the defining pathophysiology of a glaucomatous optic neuropathy is the deformation, remodeling, and mechanical failure of the ONH connective tissues. This report summarizes 20 years of technique development and study results pertinent to the characterization of ONH connective tissue deformation and remodeling in the unilateral monkey experimental glaucoma (EG) model. We view these phenomena as active, interactive processes, driven by and driving astrocyte, microglial, fibroblast, and oligodendrocyte mechanobiology. These cells, and the neural and connective tissue phenomena they propagate, have primary and secondary effects on RGC axon, lamellar beam and retrolaminar capillary and myelin homeostasis that may initially be “protective” but eventually lead to RGC axonal injury, repair and/or cell death.

The primary goal of this report is to summarize our 3D histomorphometric and optical coherence tomography (OCT)-based evidence for the early onset and progression of ONH connective tissue deformation and remodeling in monkey EG. A second goal is to explain the importance of including ONH connective tissue processes in characterizing the phenotype of a glaucomatous optic neuropathy in all species. A third goal is to summarize our current efforts to move from ONH morphology to the cell biology of connective tissue remodeling and axonal insult early in the disease. A final goal is to facilitate the translation of our findings and ideas into neuroprotective interventions that target these ONH phenomena for therapeutic effect.

1.2 Article Organization and Conventions

This report contains 8 sections. This introduction, (Section 1.0), articulates the goals, organization and conventions of this report. The 7 sections that follow provide: (2.0) a review of pertinent ONH anatomy and biomechanics; (3.0) a review of the experimental evidence for ONH connective tissue deformation and remodeling in monkey EG; (4.0) the logic for including ONH connective tissue phenomena in the phenotype of a glaucomatous optic neuropathy; (5.0) a description of our current attempts to study the cell biology of ONH axonal injury in the monkey EG model; (6.0) a discussion of the clinical implications of our findings for ONH targeted neuroprotection; (7.0) a brief summary; and (8.0) an acknowledgement of the many individuals and organizations that have contributed to this work.

The following articles should be consulted for additional information on the monkey EG model (Burgoyne, 2015b), 3D histomorphometric reconstruction (HMRN) of the ONH (Yang et al., Accepted for publication Nov 2016 Forthcoming 2017), and the phenotype of glaucomatous connective tissue alteration in monkey and human glaucoma (Burgoyne, 2015a). Table 1 provides a list of Abbreviations, Acronyms, Parameters and Definitions used in this report. By convention, all parameters are *italicized* so as to distinguish them from the anatomic landmark or structure they measure. Also by convention, we use the term “ONH” to refer to the tissues that pass through and are contained within the scleral canal as well as those that are immediately adjacent to it (i.e. the peripapillary sclera (pp-sclera), choroid, retina, and retrolaminar optic nerve).

2.0 ONH Anatomy and Biomechanics (Figures 1 – 12)

2.1 Introduction

In a series of previous publications (Bellezza et al., 2000; Bellezza et al., 2003a; Burgoyne, 2015a; Burgoyne, 2011; Burgoyne and Downs, 2008; Burgoyne et al., 2005) we have proposed a framework for conceptualizing the optic nerve head (ONH) as a biomechanical structure (Figures 1 – 12). That framework proposes important roles for intraocular pressure (IOP), IOP-related stress and strain, cerebrospinal fluid pressure (CSFp), systemic and ocular determinants of blood flow, as well as potential roles for inflammation, auto-immunity, genetics and other non-IOP related risk factors in the physiology of ONH aging and the pathophysiology of glaucomatous damage to the ONH. This biomechanical paradigm specifically proposes that IOP-related stress and strain: 1) are substantial within

the neural and connective tissues of the ONH at all levels of IOP (i.e. even when it is low); 2) underlie ONH aging; and 3) underlie the two central pathophysiologies of glaucomatous damage to the ONH — deformation, remodeling, and mechanical failure of the connective tissues and axonal compromise within the LC by a variety of IOP-related and IOP-independent mechanisms.

We have additionally proposed that modeling the ONH as a biomechanical structure provides a logic for classifying the principal components of the susceptibility of an individual ONH to a given level of IOP. While these concepts remain central to the discussion of ONH biomechanics in general, and the pathophysiology of glaucomatous damage to the ONH tissues specifically, a large group of investigators have expanded our understanding of glaucoma through the application of biomechanics and mechanobiology to the cornea (He and Liu, 2009, 2011; Liu and He, 2009; Liu and Roberts, 2005), trabecular meshwork (Braakman et al., 2014; Li et al., 2012; Overby et al., 2009; Stamer et al., 2014; Thomasy et al., 2012; Zhou et al., 2012), sclera (Coudrillier et al., 2013; Coudrillier et al., 2015a, b; Coudrillier et al., 2015c; Dastiridou et al., 2013; Fazio et al., 2014a; Fazio et al., 2014b; Girard et al., 2011b; Grytz et al., 2014; Nguyen and Ethier, 2015; Pijanka et al., 2012; Quigley et al., 2015) and ONH (Clark, 2012; Downs, 2015; Eilaghi et al., 2010; Girard et al., 2016; Girard et al., 2011a; Girard et al., 2013; Grytz et al., 2012a; Lei et al., 2011; Sigal et al., 2012; Sigal and Ethier, 2009; Sigal et al., 2005b, 2009a, b; Sigal and Grimm, 2012; Sigal et al., 2014; Stewart et al., 2014; Wang et al., 2016; Zhang et al., 2015) in health and disease. In sections 2.2 through 2.10, the details of these concepts are reviewed.

2.2 ONH Homeostasis is Influenced by Intraocular Pressure (IOP)-related Stress and Strain at all levels of IOP (Figure 1) (Burgoyne, 2011)

The ONH is made up of prelaminar, laminar and retrolaminar regions. Within the clinically visible surface of the normal ONH (referred to as the optic disc), central retinal vessels enter the eye and RGC axons appear pink due to their capillaries, which are principally supplied by branches from the posterior ciliary arteries. The primary site of RGC axon insult in glaucoma is within the lamina cribrosa, which is schematically depicted with axon bundles in Figure 1D, shown isolated by trypsin digest in a scanning electron micrograph in Figure 1E, and drawn with stippled extracellular matrix, central capillary and surrounding astrocytes in Figure 1F. Blood flow within the ONH, while controlled by autoregulation, can be affected by non-IOP-related effects such as systemic blood pressure fluctuation and vasospasm within the retrobulbar portion of the posterior ciliary arteries. Additional IOP-induced effects may include compression of posterior ciliary artery branches within the pp-sclera due to scleral stress and strain and compression of LC beam capillaries reducing laminar capillary volume flow (Langham, 1980). There is no direct blood supply to the axons within the laminar region. Nor are there astrocyte processes to the LC beam capillaries, though prelaminar and retrolaminar astrocytes send processes to the septal capillaries which are not surrounded by substantial connective tissue (Anderson et al., 1967; Hogan et al., 1971).

To our knowledge, this is the only place in the central nervous system where astrocytes do not have a foot plate on a capillary. Axonal nutrition within the lamina therefore requires diffusion of nutrients from the laminar capillaries, across the endothelial and pericyte basement membranes, through the extracellular matrix (ECM) of the laminar beam, across the basement membranes of the astrocytes, into the astrocytes, and across their processes to the adjacent axons (Figure 1F) (Anderson et al., 1967). Chronic age-related changes in the endothelial cell and astrocyte basement membranes, as well as IOP-induced changes in the laminar ECM and astrocyte basement membranes may diminish nutrient diffusion to the axons in the presence of a stable level of laminar capillary volume flow. The clinical manifestation of IOP-induced damage to the ONH is most commonly “deep cupping” (Figure 1G). While pallor of the rim is not commonly considered to be part of glaucoma, in some eyes cupping can be shallow and accompanied by pallor (Figure 1H), though this is not common.

2.3 The Principle distribution of forces, pressures and the translaminar pressure gradient within the ONH (Figure 2)

Figure 2A provides a cut-away diagram of IOP-induced mechanical stress in an idealized spherical scleral shell with a circular scleral canal spanned by a more compliant lamina cribrosa. In this case, the majority of the stress generated by IOP/orbital pressure difference is transferred into a hoop stress borne within the thickness of the sclera and lamina and is concentrated circumferentially around the scleral canal. Note in Figure 2B that the pressure behind the lamina is not simply cerebrospinal fluid pressure (CSFp) but is retrolaminar tissue pressure which has been demonstrated to be approximately $0.82 \times \text{CSFp} + 2.9 \text{ mm Hg}$ by Morgan, et al in dogs (Morgan et al., 1998). The difference between IOP and the retrolaminar tissue pressure is the translaminar pressure difference, (Figure 1C), which generates both a net posterior (outward) force on the surface of the lamina and a hydrostatic pressure gradient (the translaminar pressure gradient) within the neural and connective tissues of the pre-laminar and laminar regions. Note that the in-plane hoop stress transferred to the lamina from the sclera is much larger than the stresses induced by the translaminar pressure difference.

CSFp directly influences laminar position through its effect on the translaminar pressure difference. CSFp may also effect scleral flange position within the region it projects onto the sclera, but in most eyes, because the projection of the cerebrospinal fluid (CSF) space is minimal this is not likely important (the CSF space within Figures 2B and 2C is greatly expanded due to perfusion fixation). IOP has a similar direct effect on laminar position, but has an additional (and potentially more important) effect on laminar position through the pp-sclera. However, while the magnitude of the translaminar pressure difference may be small relative to the stresses within the sclera and lamina, the axons experience it as the translaminar pressure gradient the steepness of which is influenced by the thickness of the tissues over which it is experienced. The translaminar pressure gradient, as such, may serve as a primary barrier to axon transport and flow within this region and likely is an important physiologic determinant for the ONH axons and cells. Section 4.1 discusses a monkey study of primary CSFp lowering that provides evidence of RGC axon loss without evidence of laminar deformation or remodeling (Yang et al., 2014a).

2.4 The sclera and lamina biomechanically interact at all levels of IOP and CSFp (Figure 3)

IOP generates an expansion of the scleral shell, at all levels of IOP, which generates (and is resisted by) tensile forces within the sclera. These forces act on the scleral canal wall, causing the scleral canal opening to expand, which in turn stretches the lamina within the canal. The magnitude of these effects depend upon the level of IOP and the relative structural stiffnesses of the pp-sclera and lamina, respectively. If the structural stiffness of the sclera is more compliant than the lamina, the lamina will be pulled taut (more anteriorly positioned) and thinned in an eye at IOP 10 compared to the same eye at IOP 0 mmHg. The effects of IOP within the sclera, and the scleral effects on the lamina, are in most models, greater than the direct effects of IOP on the lamina, alone (Bellezza et al., 2000; Clark, 2012; Downs, 2015; Eilaghi et al., 2010; Girard et al., 2016; Girard et al., 2011a; Girard et al., 2013; Grytz et al., 2012a; Lei et al., 2011; Sigal et al., 2012; Sigal and Ethier, 2009; Sigal et al., 2005b, 2009a, b; Sigal and Grimm, 2012; Sigal et al., 2014; Stewart et al., 2014; Wang et al., 2016; Zhang et al., 2015). It is important to recognize that CSFp and IOP have fundamentally different effects on the tissues of the ONH because IOP generates profound scleral tensile effects that are delivered to the lamina. CSFp, in most eyes, is not likely to generate similar scleral tensile forces even when it is elevated, but particularly when it is low. The biomechanical effects of elevated CSFp on the ONH tissues have recently been modeled and discussed (Feola et al., 2016). The lack of laminar deformation in the primary CSFp lowering study support these concepts (Yang et al., 2014a) (Section 4.1).

2.5 The Volume Flow of Blood within the Posterior Ciliary Arteries should be affected by IOP-related Stress and Strain within the PP-sclera and Scleral Flange (Figures 4 – 6)

The posterior ciliary arteries pass through the pp-sclera immediately adjacent to the scleral portion of the neural canal (Figure 4). We refer to this portion of the sclera as the scleral flange (Yang et al., 2007b). The sclera thins here to accommodate an expansion of the scleral canal that occurs in a highly eye-specific fashion. While the large penetrating vessels to the choroid are outside of the flange, the circle of Zinn-Haller and the penetrating branches that pass to the pre-laminar, laminar and retrolaminar nerve pass directly through these tissues and are therefore subject to the compressive and tensile effects of their contained mechanical stress and strain. Within the lamina cribrosa, there is no direct blood supply to the axons or the axon bundles (see Figure 1). Each lamina beam contains a capillary, which are shown in an isolated vascular casting of a monkey eye in Figure 4, (Cioffi and Van Buskirk, 1996). Hayreh (Hayreh et al., 1970) demonstrated sensitivity of the peripapillary choroidal circulation to acute IOP elevation in the monkey ONH using fluorescein angiography (Figure 5). We and others have hypothesized that IOP-related stress and strain within the scleral flange underlie the phenomenon of outward bowing of the pp-sclera and retinal pigment epithelial (RPE) atrophy (Figure 6) in monkey experimental and human glaucoma. Similar blood flow effects may also occur within the peripheral lamina capillary beds, either causing, or contributing to, peripheral lamina beam remodeling (Section 2.7, below) and peripheral axonal susceptibility.

We further propose that the clinical phenomenon of peripapillary hypo and hyper-reflectance (Figure 6) are manifestations of outward bowing of the pp-sclera and decreased peripapillary choroidal blood flow, respectively. In the case of hypo-reflectance, we believe that the local

change in the plane of the underlying pp-sclera as it bows outward alters the reflective properties of the peripapillary retinal surface to the white examination or photographic light. In the case of hyper-reflectance (or “atrophy”), we share the belief of others (Alm and Bill, 1972, 1973; Kubota et al., 1993a, b) that chronic diminution in peripapillary choroidal blood flow underlies peripapillary RPE atrophy (Figure 6). The fact that a “beta” form of peripapillary atrophy (Broadway et al., 1999; Burgoyne, 2015a; Burgoyne and Downs, 2008; Jonas and Grundler, 1996) is present in aged human eyes with and without glaucoma, suggests that compromise of the peripapillary choroidal circulation also occurs over the lifetime of many human eyes and may contribute to age-related glaucoma susceptibility.

The connective tissue components of “senile sclerotic” cupping are discussed in greater detail in Section 3.6, below. We propose that the vascular components of senile sclerotic cupping (see Figure 32), are explained by the concepts discussed, above. Vascular changes in the monkey EG model are described in Section 3.8.

2.6 While Damage to the Neural and Connective Tissues of the ONH is multifactorial in Glaucoma, ONH appearance in the neuropathy is influenced by ONH connective tissue stiffness (Figures 7 – 9) (Burgoyne, 2015a)

In our biomechanical paradigm, IOP-related stress and strain influence the ONH connective tissues, the volume flow of blood (primarily) and the delivery of nutrients (secondarily), through chronic alterations in connective tissue stiffness and diffusion properties (explained in Figures 1–6). Non-IOP related effects such as auto-immune or inflammatory insults and retrobulbar determinants of ocular blood flow can primarily damage the ONH connective tissues and/or axons, leaving them vulnerable to secondary damage by IOP-related mechanisms at normal or elevated levels of IOP (Figure 7). Once damaged, the ONH connective tissues, (which can be compliant or rigid prior to insult), can become more or less rigid depending upon ONH astrocyte, fibroblast and glial response. Once weakened, by whatever mechanism, the ONH connective tissues deform in a predictable manner (Figure 8) which underlies the laminar component of clinical cupping (Figure 9). Differences in the “depth of EG cupping” in young (generally more compliant) and old (generally more stiff) monkey eyes are described in Section 3.6, below.

2.7 ONH Connective Tissue Deformation, Remodeling, Failed Remodeling and Mechanical Failure underlie “Laminar” Cupping (Figures 8 and 9)

While “deep”, “laminar” or “glaucomatous” cupping can be caused by IOP-related or non-IOP related insults, (see Figure 7), regardless of the primary insult to the ONH connective tissues, once weakened their deformation is driven by IOP-related connective tissue stress and strain regardless of its level. Thus the presence of ONH connective tissue deformation in any optic neuropathy is evidence that the level of IOP at which it occurred (whether normal or elevated) is too high for the connective tissues in their present condition. Early IOP-related damage in the monkey eye (Figure 8) (Bellezza et al., 2003b; Burgoyne et al., 2004; Downs et al., 2005; Downs et al., 2007; Yang et al., 2007a; Yang et al., 2007b) includes posterior bowing of the lamina and pp-sclera accompanied by scleral canal expansion, thickening (not thinning) of the lamina, and outward migration of the laminar insertion from the sclera into the pia mater. In our studies to date this appears to represent mechanical yield

(permanent stretching) combined with mechanical failure (physical disruption) of the lamellar beams. We propose that while its onset may be diffuse, failure occurs focally within the anterior most lamellar beam insertions (into the scleral canal wall and Border Tissues of Elschnig) and spreads to adjacent beams (both circumferentially and by depth within the canal wall), as the load from failed or disrupted beams is shifted to neighboring beams making them more susceptible to failure. Progression to end-stage damage is likely along and within the canal wall and eventually includes profound scleral canal wall expansion (which underlies the clinical phenomenon of “excavation”), progressive posterior deformation, and eventual thinning of the lamina. If all other aspects of the neuropathy are identical, the stiffer the lamina (so long as it is not brittle) the more resistant it will be to deformation. Whether a “stiff” lamina is better or worse for the adjacent cells and axons than a “compliant” lamina depends upon several issues that are neither well understood nor well studied. Principal among these are: 1) what is the relationship between LC beam “stiffness” and LC beam nutrient diffusion; 2) how do nutrients get from the LC beam capillaries to the LC beam astrocytes; 3) do LC beam astrocytes have footplates on the LC beam capillaries or are they dependent upon diffusion; 4) how do nutrients get from the LC beam into the center of the RGC axon bundles; 5) if the abundant astrocyte processes within the axon bundles are the source of nutrient delivery, what happens to those processes as the astrocyte basement membranes on the LC beams are deformed, remodeled and disrupted; 6) what is the relationship between LC beam stiffness, axonal deformation and axonal physiology, i.e. how much strain can axons handle even when well nourished?

2.8 All Clinical Cupping, Regardless of Etiology, Manifests “Prelaminar” and “Laminar” Components (Figure 9)

Regardless of the etiology, clinical cupping can be “shallow” or “deep” (Figure 9). A prelaminar or “shallow” form of cupping is primarily due to loss (thinning) of prelaminar neural tissues without important lamellar or ONH connective tissue involvement. Lamellar or “deep” cupping follows ONH connective tissue damage, deformation and remodeling as schematically depicted in Figure 8. While a lamellar component of cupping predominates in a glaucomatous optic neuropathy, it is the prelaminar component that underlies clinical rim thinning. While prelaminar (rim) thinning is a manifestation of neural tissue damage and or “stretching” (Fortune et al., 2016b) alone, we propose that “lamellar” or “deep” cupping can only occur in the setting of ONH connective tissue deformation and remodeling, regardless of the IOP at which these phenomena occur. Section 4.0, below, addresses the need to include a characterization of ONH connective tissue deformation and remodeling in the phenotype of all optic neuropathies.

2.9 Over the Course of a Lifetime, a given eye demonstrates the “Optic Neuropathy of Aging” or the Optic Neuropathy of Glaucoma Based on ONH Susceptibility (Figure 10)

We have previously proposed that the optic neuropathies of aging (i.e. age-related axon loss), glaucoma that occurs at normal levels of IOP and glaucoma that only occurs if IOP is elevated are a biological continuum (Burgoyne and Downs, 2008). By this we mean that they share a common group of risk factors that are present at normal levels of IOP, with each risk factor becoming more (or less) pronounced as IOP is elevated. For a given ONH, IOP (at all levels of IOP) generates low or high levels of stress depending upon the 3D

architecture (geometry) of the ONH connective tissues (size and shape of the canal, thickness of the lamina and sclera). Some ONHs will experience relatively low stress at high IOP, and others will have high stress at low IOP, depending upon the geometry and material properties of their connective tissues. Whether a given level of IOP-related stress is physiologic or pathophysiologic depends upon the ONH's microenvironment. Strong connective tissues, a robust blood supply and stable astrocytes and glia increase the chance of "normal" ONH aging. While the existence of a neuropathy of aging is controversial, the pattern of "normal" age-related axon loss and the development of glaucomatous damage are similar (Chauhan et al., 2015; See et al., 2009; Yang et al., 2017). We propose that age-related ON axon loss and glaucoma are both influenced by IOP, at all levels of IOP, and share the same non-IOP-related risk-factors and mechanisms (Figure 7). Whether an individual develops enough "age-related" axon loss to achieve the diagnosis of glaucoma, in the setting of a statistically "normal" level of IOP is a matter of ONH susceptibility and the skills of the clinician examiner.

2.10 Connective Tissue Deformation and Remodeling is Unique to the Optic Neuropathy of Glaucoma and should be part of its staging (Figures 11 and 12)

We propose that the defining pathophysiology of a glaucomatous optic neuropathy is the deformation, remodeling, and mechanical failure of the ONH connective tissues described above and in Figures 11 and 12. These phenomena have yet to be detected in any other human or experimental form optic neuropathy as discussed in Section 4, below (Burgoyne, 2015a). We also propose that the cellular processes that underlie these morphologic connective tissue phenomena not only underlie the clinical appearance and behaviour of glaucomatous cupping (i.e. the depth and excavation of the "cup"), but they also underlie the classic patterns of RGC axonal injury and visual field loss that define the neuropathy whether it occurs at normal or elevated levels of IOP. We further propose that because mechanobiology drives these cellular processes, ONH biomechanics should allow us to eventually predict eye-specific regional susceptibility (i.e. where ONH damage will occur first in a given eye) and at what levels of IOP-related and/or IOP-independent risk factors that damage will occur.

We have identified five morphologically recognizable components of ONH connective tissue alteration in the monkey EG model (Figure 12 and Section 3.0, below) (Yang et al., 2015a): 1) posterior (outward) lamellar deformation; 2) scleral canal expansion; 3) posterior (outward) migration of the anterior lamellar insertion (ALI) and posterior lamellar insertion (PLI) (from the sclera into the pial sheath); 4) lamellar thickness change; and 5) posterior (outward) bowing of the pp-sclera. We propose that these five components provide a strategy for morphometrically staging ONH connective tissue change in monkey EG that is independent from the state of RGC axon health. While such a strategy will require careful clinical study, it will lay the scientific foundation for treating certain forms of ONH connective tissue structural abnormality or change as early "structural glaucoma", having determined their power to predict subsequent progression to detectable visual field loss. We argue for the term "structural glaucoma" rather than "pre-perimetric glaucoma" to separate the question of whether there is disease present from the question of whether to treat early disease. In this conceptual framework, "structural glaucoma" will be glaucoma, defined both

by the magnitude and character of its difference from normative data bases, and by its power to predict both subsequent structural progression and eventual visual field loss.

3.0 Experimental Evidence of ONH Connective Tissue Deformation, Remodeling and Mechanical Failure in the Monkey EG Model

3.1 Background (Figure 12)

The connective tissue components of glaucomatous cupping in the monkey and human eye have been classically described to include lamellar deformation, scleral canal expansion and progressive lamellar thinning (Furuyoshi et al., 2000; Jonas et al., 2011; Kalvin et al., 1966; Quigley and Addicks, 1980). In a previous review article (Burgoyne et al., 2005) we hypothesized that focal mechanical failure of the anterior lamellar beams at their insertion into the sclera, followed by circumferential (radial) and posterior (outward) extension of this failure could explain these phenomena. However, in a series of subsequent publications characterizing early ONH connective tissue change in monkeys with unilateral experimental glaucoma (EG), we described posterior deformation and thickening of the lamina (Yang et al., 2007a; Yang et al., 2007b), accompanied by scleral canal expansion (Downs et al., 2007), outward bowing of the pp-sclera (Yang et al., 2007a; Yang et al., 2007b), and outward migration of the lamellar insertion into the retrobulbar pial sheath (Yang et al., 2011b). These phenomena, together suggested that the lamina was not just deforming in response to chronic IOP elevation but was “remodeling” itself into a new shape in response to its altered biomechanical environment (Burgoyne, 2011; Hernandez, 2000; Roberts et al., 2009; Yang et al., 2011b). One aspect of the increase in lamellar thickness appeared to be the addition of new beams (Roberts et al., 2009), which, combined with evidence for lamellar insertion migration (Yang et al., 2011b), suggested that recruitment of the longitudinally oriented retrolamellar optic nerve septa into more transversely oriented structures may be part of the lamina’s initial remodeling response in early monkey EG (Roberts et al., 2009). This section summarizes key 3D histomorphometric, OCT, blood flow, and scleral material property changes within the monkey unilateral EG model.

3.2 3D Histomorphometric Evidence to support the Five Morphologic Connective Tissue Components of Glaucomatous Cupping (Yang et al., 2015a)

3.2.1 Our Method for Quantifying ONH anatomy within 3D Histomorphometric Reconstructions (HMRNs) (Figures 13 – 15)—Our method for 3D HMRN, delineation (Figure 13) and parameterization (Figures 14–15) of the monkey ONH has been described within a series of previous reports (Burgoyne et al., 2004; Downs et al., 2007; Lockwood et al., 2015; Pazos et al., 2016; Reynaud et al., 2016; Yang et al., 2007a; Yang et al., 2009a; Yang et al., 2007b; Yang et al., 2011b) and is summarized in detail in a recent book chapter (Yang et al., Accepted for publication Nov 2016 Forthcoming 2017). After, sacrifice and 3D reconstruction of a 6 mm trephine that contains the ONH and pp-sclera, 40 radial digital section images (4.5° degrees apart) of the reconstruction are manually delineated (Figure 13) and global values for 19 standard 3D HMRN parameters (Figures 14–15) are quantified as previously described (Downs et al., 2007; Yang et al., 2007a; Yang et al., 2009a; Yang et al., 2007b; Yang et al., 2011b). Our parameter *Post-BMO Total*

Prelaminar Volume is defined to be the volume beneath the BMO zero reference plane, above the lamina cribrosa and within the neural canal wall (light green in Figures 12 and 14). We use EG versus Control eye differences in this parameter as a single measure of the overall EG eye connective tissue component of cupping, because it captures EG eye lamina deformation, lamina insertion migration, and scleral canal expansion in a single parameter.

3.2.2 Connective Tissue alterations within 21 unilateral EG Monkeys (Figures 16 – 19) (Yang et al., 2015a)—Figure 12 displays matched digital cross-section images from the Control and EG eyes of Monkeys which span the full range of EG versus Control eye *Post-BMO Total Prelaminar Volume Difference* (36 to 578%) present within the 21 EG eyes of a previous report (Yang et al., 2015a). Taken together these images depict the most consistent components of ONH connective tissue alteration in monkey EG: 1) posterior (outward) lamina deformation; 2) scleral canal expansion; 3) posterior (outward) migration of the ALI and PLI (from the sclera into the pial sheath); 4) lamina thickness change (increased in most eyes demonstrating the least deformation and less thickened or thinned in most eyes demonstrating the greatest deformation); and 5) posterior (outward) bowing of the pp-sclera; and their range. Schematic plots of the global Control and EG eye 3D histomorphometric data for each animal are shown in Figure 16. These plots allow the differences among the 21 Control eyes and the full range of EG versus Control eye differences among the 21 study animals to be appreciated.

Figure 17 depicts the range of animal-specific, *Post-BMO Total Prelaminar Volume* change within all 21 EG eyes. *Lamina position change*, anterior scleral canal opening expansion, ALI expansion and migration are plotted relative to it. These data together illustrate how EG versus Control eye *Post-BMO Total Prelaminar Volume Difference* incorporates each of these phenomena and in so doing serves as a surrogate of overall connective tissue deformation.

Figure 18 depicts the range of lamina thickness parameter alteration. Figure 18D makes clear that animal specific changes in lamina thickness were bimodal, being: 1) significantly thickened in 11 of the 15 EG eyes demonstrating 36% to 240% EG eye expansions in *Post-BMO Total Prelaminar Volume* (Animals 1–15); 2) less thickened in animals demonstrating from 241 to 279% EG eye expansions in *Post-BMO Total Prelaminar Volume*; and 3) significantly thinned in 2 of the 3 animals demonstrating the greatest overall deformations. These data suggest that while the lamina was thickened in most eyes with minimal and moderate deformation, it was less thickened and then thinned in the most deformed eyes. It also suggests that the transition from (mostly) thickened to less thickened and then thinned in the 21 monkeys of this report, appears to have occurred at or around overall deformations yielding EG eye *Post-BMO Total Prelaminar Volume* expansions of 240%.

Significant anterior (inward) migration of the ALI (Figure 18E) was present in the 2 EG eyes with the least global deformation as characterized by *Post-BMO Total Prelaminar Volume Change*. Progressively larger posterior migration of the ALI was detected in the 16 EG eyes demonstrating the largest global deformation. LI migration (Figure 18F) was detected in 17 of 21 EG eyes and was progressively outward, though this occurred in an early diminishing (Monkeys 1–6) and later increasing (Monkeys 7–21) manner.

Outward bowing of the peripapillary sclera, detected as significant increases in the parameter *pp-scleral Position*, (Figure 19), was present in 11 EG eyes, with a 12th demonstrating a significant decrease. Similar to scleral canal expansion, outward bowing of the pp-sclera was not progressive through the full range of overall deformation, achieving its maximum value in eyes with early levels of *Post-BMO Total Prelaminar Volume* expansion.

3.2.3 Implications of These Connective Tissue Alterations for Staging and Phenotyping

—These cross-sectional findings are important for two reasons. First, they suggest that a single volumetric parameter like *Post-BMO Total Prelaminar Volume* (Figures 12 and 17A) may, by itself or by its change over time, provide a measure that “orders” overall lamina/scleral connective tissue deformation and remodeling and in so doing allows for its staging and phenotyping in glaucoma. Second, they identify the principal components of connective tissue alteration that allows for their respective mechanisms and respective links to RGC axonal insult to be the subject of future studies.

We have previously proposed that lamina thickness change as well as ALI and PLI migration are separate manifestations of glaucomatous ONH connective tissue remodeling and/or mechanical failure (Burgoyne, 2011; Yang et al., 2011b). Previous finite element (FE) modeling (Grytz et al., 2012b) has predicted that the lamina should thicken in response to elevated IOP, that its anterior insertion should migrate anteriorly, and its posterior insertion should migrate posteriorly as part of this process. The fact that the two EG eyes with the least amount of overall deformation (Monkeys 1 and 2) demonstrate inward ALI migration (Figure 18E), suggests that inward migration of the ALI represents *an initial stage of connective tissue remodeling* (Grytz et al., 2012b). These data also suggest, but do not prove, that as global ONH connective tissue deformation increases, inward ALI migration transitions to outward migration that is subsequently progressive. The longitudinal detection of ALI migration (Lee et al., 2014b) is therefore important for two reasons. First, using current OCT imaging, it may be linked to nerve fiber layer (NFL) hemorrhages (Lee et al., 2014a), NFL defects (Tatham et al., 2013), visual field progression (Faridi et al., 2014), and the development of acquired optic disc pits (You et al., 2013). Second, it may confirm the relative timing of its direction (i.e. inward during initial deformation, outward as deformation progresses) suggested by our cross-sectional findings.

Regarding PLI migration, we propose that outward PLI migration is a prominent component of lamina remodeling in response to chronic IOP elevation in the monkey eye. While it is possible that ALI and PLI migrations are completely independent, it is also possible that outward ALI migration contributes to the mechanisms driving outward PLI remodeling. In this regard, the suggestion in our data (Figure 18F) that outward migration of the PLI occurs in an initial phase that diminishes and is followed by a phase that progressively increases, may reflect a transition from ALI and PLI remodeling that stabilizes the insertions to PLI remodeling that is driven by outward migration of the ALI.

The implications of these connective tissues findings for phenotyping the optic neuropathy of glaucoma are discussed in Section 4.0.

3.3 The Lamina Cribrosa Pores Increase and Beams both Increase and Decrease in Monkey early EG (Figures 20 – 27) (Reynaud et al., 2016) (Lockwood et al., 2015)

3.3.1 Background—Our method for quantifying laminar microarchitecture (LMA) has been described in previous publications (Grau et al., 2006); (Lockwood et al., 2015; Reynaud et al., 2016) and is schematically depicted in Figure 20. Each step of the method is briefly outlined in the sections that follow and is illustrated in Figures 21–24. EG versus Control eye differences and percent differences for *beam diameter (BD)*, *pore diameter (PD)*, *Connective Tissue Volume Fraction (CTVF)*, *Connective Tissue Volume (CTV)* and *Laminar Volume (LV)* are generated for each animal. Animal specific EG versus Control eye differences are compared with the maximum value of the *Physiologic Inter-eye Percent Difference (PIPD)* within bilateral normal animals to determine significance. A gamma distribution function (Carolynne, 2014), is used to fit the frequency data of the *BD* and *PD* voxels in each eye to generate distribution parameters which were used to compare overall EG versus Control eye distribution differences. A detailed description of the overall (experiment-wide) and animal-specific (comparison of the EG to the Control eye within each individual animal) is contained within our previous paper (Reynaud et al., 2016).

3.3.2 LMA Alterations Within 14 Early EG Monkeys (Figures 25–26) (Reynaud et al., 2016)—By distribution analysis, pores were on average 17% larger in the EG eyes, with this increase being consistent across all pore diameters. EG versus Control eye differences in *BD shape, scale, estimated mean* and *estimated standard deviation* did not achieve significance (all $p > 0.05$, paired t-test). Figure 25 graphically depicts the overall (experiment-wide) *BD* and *PD shape* and *scale* data.

Figure 26 graphically summarizes animal-specific EG versus Control eye difference data for each LMA parameter both by full thickness and laminar depth. EG eye *BD* was significantly larger than the Control eye (14.1% and 16.5%) in two animals and significantly smaller (10.4% – 31.5%) in three animals, while *PD* was significantly larger (17.1% to 37.6%) in six animals and decreased in none. In addition, *CTVF* was significantly smaller in one animal (–32.8%) while *CTV* was significantly larger in eight animals (20.7% – 127.9%) and significantly smaller in one animal (–22.4%). *LV* was increased (15.4% – 145.5%) in 10 of the 14 EG animals.

3.3.3 Implications of early LMA change in Monkey EG—LC beam and pore anatomy have long been thought to underlie the pattern of glaucomatous RGC axon loss in glaucoma (Quigley and Addicks, 1981; Radius and Gonzales, 1981). However, little is known about the nature of longitudinal change in early monkey experimental or human glaucoma. Within the distribution analyses, *PD* was on average 17% larger in early EG versus Control eyes and this increase occurred equally across all sizes of *PD*. While EG versus Control eye differences in *BD* were not significant, the volume of EG eye Beam voxels was on average increased by 26.5% as manifested in increased *CTV*. This increase in Beam voxels was equally distributed across all *BD* sizes. These EG eye increases in mean *PD* and *CTV* occurred in the setting of mean *LV* increases of 40%. As in our earlier study (Roberts et al., 2009), EG eye alterations in global *CTV* and *LV* occurred in such a way that global *CTVF* was unaltered. Separate from these overall EG versus Control eye LMA

parameter differences, animal-specific, EG eye alterations were variable, such that overall LMA parameter change does not reflect the behavior of every individual EG eye.

LMA alterations in monkey early EG are important for several reasons. First, it has been shown that the lamina cribrosa is a site of axonal transport and flow blockade at all levels of IOP in the normal and glaucomatous monkey eye (Anderson and Hendrickson, 1974; Gaasterland et al., 1978; Minckler et al., 1977; Quigley and Addicks, 1980; Quigley et al., 1979). Second, the lamina cribrosa and pp-sclera are the major load bearing connective tissue of the ONH and the combination of their micro / macro-architecture and material properties determine their respective structural stiffness, macroscopic behavior and the microscopic distribution of IOP-related stress and strain within their tissues (Girard et al., 2009c; Roberts et al., 2010a; Sigal et al., 2009b). Each of these bioengineering phenomena likely generate primary and secondary effects on the connective tissues, contained blood vessels (and their autoregulation) and their constituent cells (activation, proliferation, migration, phagocytosis) that contribute to the mechanisms of axonal insult.

However, the fact that our post-mortem data suggests that pore diameters increased substantially and *BD* increases did not occur in the majority of EG eyes must be carefully interpreted. We emphasize that our post-mortem analyses cannot speak to the longitudinal behavior of the EG eye LC beams. A scenario of acute or sub-acute posterior deformation of the LC within an expanded scleral canal following initial IOP elevation, may have led to profound acute or sub-acute expansion of the LC pores accompanied by LC beam thinning. In eyes capable of mounting a cellular response, new connective tissue synthesis and remodeling may have resulted in the recovery of beam diameters that were not detectably different from baseline. In this scenario, the return to a baseline beam architecture combined with the achievement of “stiffer” connective tissue material properties would have left the beam stiff enough to stabilize the LC in its deformed state without the additional connective tissue synthesis required for detection as a beam diameter “increase”, relative to the contralateral control. Our *BD* data therefore require additional longitudinal studies to be properly interpreted.

Figure 27 depicts our hypotheses regarding the factors influencing EG eye-specific, LMA parameter change. We propose that these factors do so through their contributions to two principal determinants of ONH connective tissue homeostasis: 1) how much the ONH connective tissues deform in the setting of an acute or sub-acute change in the translaminal pressure difference (more specifically the magnitude of macroscopic connective tissue deformation and its associated microscopic tissue strain that is generated); and 2) how robust and/or protective is the cellular response elicited by a given amount of tissue strain. Animal age (or cellular senescence and connective tissue stiffness at all ages) and the magnitude of IOP insult may independently influence both the magnitude of deformation and the character of the connective tissue response (ranging from no response, to synthesis, to remodelling, to degradation, or some combination of each).

For a given ONH the magnitude of deformation, and the magnitude of connective tissue synthesis and remodeling, govern the character of detected post-mortem EG versus Control eye differences in LC microarchitecture. Animal age (as a surrogate for stiff versus

compliant tissues and/or senescent versus robust cells at any age) and the magnitude of IOP insult independently influence both the magnitude of deformation and the character of the connective tissue response. In the absence of any active connective tissue response, LC deformation, alone, should result in passive thinning of the LC beams and passive expansion of the pores. Once deformed, mechanoreceptors within LC beam fibroblasts and astrocytes should drive connective tissue synthesis and remodeling.

From a beam that was acutely thinned due to deformation, if beam synthesis leads to a return to pre-deformation beam diameter, there will be no detected EG versus Control eye *BD* difference – yet the number of connective tissue voxels will have increased. Beyond synthesis, alone, where there is connective tissue remodeling and recruitment, there may be increases or decreases in the number of detected connective tissue voxels. Finally, where connective tissue synthesis and remodeling are not adequate, mechanical failure and connective tissue degradation may ensue leading to a reduction in detected connective tissue voxels. Where beams have disappeared, pore enlargement that is not due to passive pore expansion may be detected.

Age may thus influence both connective tissue material properties (more compliant when young, stiffer when old) and the vigor of the synthesis/remodeling response (more robust in the young, senescent when old). This suggests that for a given magnitude of post-laser IOP insult, age should both influence the magnitude of deformation and the character of the connective tissue response.

3.4 Lamellar Insertion Migration (Figure 12) in Early Monkey EG Appears to Include Remodeling of the Retrolaminar Orbital Septa (Roberts et al., 2009)

3.4.1 Background—One aspect of the increase in lamellar thickness as well as the profound increases in *LV* and *CTV*, without detectable increases in *BD* reported in Section 3.3 above, appears to be the addition of new lamellar beams (Roberts et al., 2009) which, combined with evidence for lamellar insertion migration (Yang et al., 2011b), led Roberts and colleagues to hypothesize that recruitment of the longitudinally oriented retrolaminar optic nerve septa into more transversely oriented structures may occur (Roberts et al., 2009). In their study, they described the textural anisotropy that results from the LMA arrangement of beams and pores and employed the mean intercept length method (Ketcham and Ryan, 2004; Oda, 1983; Odgaard et al., 1997; Turner, 1992) to locally characterize fabric in terms of the predominant orientation of the lamina cribrosa beams and the relative strength of that orientation.

3.4.2 Mean Intercept Length data suggests an increase in LC beam number in early EG—Laminar segmentations from both eyes of three early EG animals underwent a post hoc analysis to estimate the number of lamellar beams aligned in the plane of the LC of each eye. For this analysis the lamellar volume was subdivided into 45 “elements” or sub-volumes, and “probe lines” or “rays” were cast through each element in the anterior-to-posterior direction to determine the average number of connective-to-non-connective tissue transitions per number of rays cast. This measurement provided an estimate of the average number of lamellar beams through the thickness of the LC within each lamellar sub-volume

of each EG and Control eye. When comparing the number of laminar beam intercepts within the EG versus Control eye of each animal, the mean number of laminar beams through the thickness of the LC was greater (46%, 18%, and 17%, respectively) in the three EG eyes.

While these data support the hypothesis that pre-laminar or retrolaminar septa are “recruited” or “remodeled into” transverse, load-bearing, lamina-like beams, this method could not determine the location of the “new” beams (i.e. if they were “added” to the anterior or posterior surface of the post-laser LC).

3.4.3 Implications of laminar insertion migration and retrolaminar septal

recruitment—Previous modeling studies by Grytz, et al. (Grytz et al., 2012b) predicted the lamina should add new beams both anteriorly and posteriorly as part of its early remodeling response. The strong 3D histomorphometric evidence for outward (posterior) migration of both the ALI and PLI in early EG, suggests that if recruitment of the prelaminar glial column connective tissues occurs, these new beams are themselves either quickly remodeled away or undergo mechanical failure and dissolution. While both laminar insertion migration (Yang et al., 2011b) and mean intercept length analyses (Roberts et al., 2009) support retrolaminar septal recruitment they do not prove that it is the sole form of laminar beam remodeling. Interestingly, Hayreh and coworkers reported retrolaminar fibrosis in the monkey model of EG (Hayreh et al., 1999). This observation is compatible with retrolaminar septal recruitment, although Hayreh made no comment about the orientation of beams or their insertion into the pia, and the animals in his study were at a more advanced stage of glaucomatous damage.

It is reasonable to believe that the presence of retrolaminar septal recruitment and remodeling would increase the homeostatic demands on the retrolaminar astrocytes, microglia and oligodendrocytes and in so doing contribute to early RGC axon injury. In two recent papers, collaborative work from the Marsh-Armstrong and Ellisman laboratories (Davis et al., 2014; Nguyen et al., 2011) has shown that myelin transition zone astrocytes phagocytose myelin and RGC axonal mitochondria, within the myelin transition zone (immediately behind the cellular lamina of the mouse eye) as part of the support they provide to the RGC axons. We have shown proteomic (Burgoyne et al., 2014) and immunohistochemistry (IHC) data (Stowell et al., 2014) that suggest expression of myelin-related proteins is decreased within the retrolaminar optic nerve in monkey early EG. We are actively studying the contribution of myelin homeostasis to the mechanisms of axonal injury in monkey early EG (see Section 5.7, below).

3.5 Longitudinal Detection of Laminar Deformation by OCT Precedes Retinal Nerve Fiber Alteration in Monkey Early EG (Figures 28 – 31) (He et al., 2014b)

3.5.1 Background—If ONH connective tissue deformation and remodeling is a defining pathophysiology of glaucomatous damage to the visual system, can we use longitudinal OCT imaging to detect it, and if so, when is it detectable relative to OCT-detected RNFL thickness (RNFLT) change? We previously reported the presence of OCT-detected deep ONH change at the time of confocal scanning laser tomography (CSLT) ONH surface change within the pre-sacrifice OCT data sets of 9 rhesus macaque monkeys with chronic,

laser-induced, unilateral IOP elevations (Strouthidis et al., 2011). That study suggested several promising OCT parameters for assessing longitudinal change, but was limited by not utilizing the complete set of baseline and post-laser imaging sessions preventing trend-based change detection, and did not make comparisons to scanning laser polarimetry (SLP) imaging and multifocal electroretinography (mfERG) testing.

In a follow up study, both eyes from 4 young and 4 old monkeys were tested 3 times at baseline, and then every 2 weeks following laser-induced, chronic unilateral IOP elevation until CSLT-detected ONH surface change was detected and confirmed on two subsequent occasions, at which point each animal was sacrificed. Event and trend-based definitions of onset in both the control and EG eyes for 11 OCT, CSLT, SLP and mfERG parameters were explored (Figures 28–31) (He et al., 2014b).

3.5.2 Results—For both event and trend-based analyses, onsets were achieved earliest and most frequently within the ONH neural and connective tissues using OCT and at the ONH surface using CSLT. OCT ONH neural and connective tissue parameter change preceded or coincided with CSLT ONH surface change in most EG eyes (Figure 31). OCT and SLP measures of RNFLT and mfERG measures of visual function demonstrated similar onset rates, but occurred later than OCT ONH and CSLT surface change and in fewer eyes (Figure 31). Using event-based analysis, only OCT Anterior Laminal Surface Depth relative to BMO reference plane (*ALCSD-BMO*, Figure 29) and *Rim Volume (Rim V)* detected change onset in all 8 EG eyes. Using trend-based analysis, OCT *ALCSD-BMO*, *ALCSD-BM*, *Rim V* and *CSLT mean position of the disk (MPD)* detected change onset prior to sacrifice in all 8 EG eyes. OCT RNFL parameters, SLP and mfERG detected less frequent change onsets in both the EG and Control eyes (data not shown). Posterior (outward) movement of BMO relative to a peripheral BM reference plane was detected in 4 of the 8 EG eyes (Figure 31).

3.5.3 Implications—The conversion from experimental ocular hypertension to glaucomatous damage to the monkey visual system within the EG eyes of these 8 animals was detected earliest, most frequently, and with the greatest specificity within the ONH neural and deep connective tissues using OCT. These data demonstrate that detectable deep and surface ONH change precedes detectable RNFL and retinal functional change in the monkey EG model – and that in 6 of the 8 studied EG eyes these changes occurred at levels of global post-mortem orbital optic nerve axon loss (+2 to –19%) that may precede visual field loss (Harwerth et al., 2007). In addition, in 4 of the 8 animals, outward deformation of the BMO was detected relative to a peripheral BM reference plane by OCT. Outward movement of BMO may be due to choroidal thinning and/or pp-scleral outward bowing. Definitive separation of these two phenomena will require anterior scleral visualization and parameterization, which is currently under development. Until proven otherwise, we believe that both phenomena are present in these 4 eyes.

While the lack of detectable change in both the RNFLT and in retinal function does not mean that pathology was not present, these data support the notion that very early events in the pathophysiology of glaucoma in the monkey eye occur within the ONH and pp-sclera. These data also suggest that events within the RGC axons and soma are either secondary to these

ONH events and occur later or, if they are occurring earlier than the ONH events, they are progressing more slowly relative to the sensitivity of the methods used for their detection. These data contribute to the growing body of evidence that suggests that the ONH is a primary site of early insult to the visual system in glaucoma (Burgoyne, 2011; Quigley et al., 1981). In addition, they confirm that early glaucomatous damage to the monkey ONH includes both neural and connective tissue components (Yang et al., 2007a; Yang et al., 2009a). This finding is important because it identifies OCT-detectable ONH connective tissue endpoints for other monkey experimental optic neuropathy models including chronic experimental CSFp lowering (Yang et al., 2014a), endothelin (Brooks et al., 2004), optic nerve transection (Ing et al., 2016) and anterior ischemic optic neuropathy (AION) (Miller et al., 2014) which are discussed in Section 4.0, below.

3.6 Age Effects on OCT-detected Laminal Deformation in Monkey Early EG (Figures 32 – 33) (Yang et al., 2014b)

3.6.1 Background—Deep and shallow forms of human glaucomatous cupping occur at all ages and IOP levels but are classically seen in youthful and elderly eyes, respectively. We have proposed that the ONH connective tissues “harden” with age and that on average aged eyes should demonstrate a shallower form of cupping (i.e. a shallower “phenotype”) as a result (Burgoyne and Downs, 2008). As discussed in Section 2.0, above, eye-specific differences in structural stiffness and/or remodeling, regardless of age, should contribute to the glaucomatous phenotype expressed by an individual eye (Figures 4 and 32) (Burgoyne and Downs, 2008). In a follow up study on the 4 young and 4 old animals studied in Section 3.5, above (Yang et al., 2014b), we analyzed the same longitudinal OCT data sets to test the hypothesis that OCT-detected ONH structural change was greater in the 4 young as compared with the 4 old monkey EG eyes at similar post-laser time intervals, similar levels of post-laser cumulative IOP insult, and at the onset of CSLT ONH surface change.

3.6.2 Old Monkey Laminas Deform Less at the Onset of OCT Detected ONH Change in Monkey EG—The median age of the 4 young animals was 1.9 years (range 1.4 to 2.6) at study initiation, and the median length of post-laser follow-up was 33 weeks (range 26 to 34 weeks). The median age of the 4 old animals was 20.95 years (range 18.6 to 21.9) at study initiation, and the median length of post-laser follow-up was 23 weeks (range 21 to 39 weeks) ($p=0.34$ for post-laser follow-up times, Wilcoxon rank sum test). In these 4 young and 4 old animals, the magnitude of OCT ONH parameter change was greater in the young compared to the old eyes both at the point of CSLT-detected ONH surface change and also when measured as continuous variables relative to post-laser time (in days) and post-laser cumulative IOP insult (in mmHg \times days). The data also suggest that structural change was greater for both the ONH rim and deep connective tissues in the young eyes. Regarding the ONH deep connective tissues, when compared by age group versus time or versus cumulative IOP insult, lamina cribrosa deformation relative to BMO (*ALCSD-BMO*) and BMO deformation relative to peripheral BM (BMO Depth) were both greater in young compared to old monkey eyes. Change from baseline data at each post-laser imaging session is plotted for a subset of parameters relative to the imaging session cumulative IOP insult in Figure 33. In general, it is evident that the young eyes were followed to lower levels of cumulative IOP insult than the old eyes, in that the young eye data points (red dots) end at

less than 600 mmHg×day while the old eye data points (blue dots) extend to more than 1200 mmHg×day).

Finally, for a given increase in cumulative IOP insult, the anterior lamina surface deformed posteriorly at magnitudes that were 3.64 times faster in the young compared to the old EG eyes. BMO Depth relative to BM (a measure of outward peripapillary bowing) also demonstrated age related differences in IOP responsiveness.

3.6.3 Implications of Age Related Differences in the Phenotype of

Glaucomatous Cupping—These findings suggest that at similar levels of cumulative IOP insult and at the onset of CSLT ONH surface change, OCT detected ONH prelaminar and connective tissue structural change is greater in young compared to old monkey eyes. These data support the concept that age related differences in ONH connective tissue structural stiffness and/or remodeling may contribute to age-related differences in the appearance of early glaucomatous cupping in a given eye. Our findings also suggest that while OCT detectible ONH change that precedes detectible RNFL change was associated with minimal optic nerve axon loss in 2 eyes, it was associated with modest to moderate (12 to 29%) axon loss in the remaining 6 monkey eyes.

3.7 Longitudinal OCT Detection of Laminal Hypercompliance in Monkey Early EG (Figures 34 – 37) (Ivers et al., 2016)

3.7.1 Background—We have previously used simultaneous videography (Burgoyne et al., 1995a, b), CSLT ONH surface imaging (Heickell et al., 2001), post-mortem histology (Bellezza et al., 2003a, b), and 3D histomorphometric reconstruction (Yang et al., 2009b; Yang et al., 2011a) to study ONH compliance in response to acute IOP elevation in monkey Control and EG eyes. These studies indirectly suggested laminal and pp-scleral hypercompliance were present at the onset of monkey EG, however each study was either not specific to the lamina cribrosa (Burgoyne et al., 1995a, b; Heickell et al., 2001), or was post-mortem and therefore could not separate “fixed deformation” from “acute compliance” within each individual study eye (Bellezza et al., 2003b; Yang et al., 2011a).

In a recent study, we defined ONH compliance to be the magnitude of OCT-detected ONH neural and connective tissue deformation following acute IOP elevations of fixed magnitude (IOP 10 to 30 mmHg) and duration (30 minutes). We then used in vivo OCT imaging to compare EG versus Control eye ONH morphology change following acute IOP elevation from 10 to 30 mmHg in both eyes of 15 monkeys at the onset of unilateral EG (EG onset) (Ivers et al., 2016). Our hypothesis was that the majority of animals would demonstrate greater acute posterior deformation of the lamina cribrosa and pp-sclera within the EG eye as compared to the contralateral Control eye, and in so doing, provide direct evidence for laminal and pp-scleral hypercompliance in early monkey EG.

IOP was chronically elevated in one eye of each animal using a laser. EG onset was identified using CSLT. OCT ONH imaging (40 radial B-scans) was performed at 10 mmHg prior to (pre) and following (post) laser. At EG onset, OCT scans were obtained at IOP 10 and 30 mmHg. OCT landmarks within both the IOP 10 and IOP 30 OCT data sets were delineated to quantify IOP 10/30 differences (*compliance*) for the following OCT parameters

(Figures 28–31): (*ALCSD-BMO*), ALCSD relative to peripheral BM (*ALCSD-BM*) and BMO depth relative to peripheral BM (*BMOD-BM*).

3.7.2 OCT detected laminar hypercompliance occurs early in monkey EG—

Figure 34 uses representative B-scans from the Control and EG eyes of one study animal to illustrate ONH and retinal anatomy delineated within images acquired at baseline (pre-laser) IOP 10 mmHg and at EG eye onset (at which time point B-scans from IOP 10 and 30 mmHg data sets are shown). For both the Control and EG eyes, OCT-detected fixed deformation and acute compliance at EG onset are defined and demonstrated. The effect of elevating IOP from 10 to 30 mmHg was greater in EG vs. Control eyes for *ALCSD-BMO* ($-46 \pm 45 \mu\text{m}$ vs. $-8 \pm 13 \mu\text{m}$, $P=0.0042$) and *ALCSD-BM* ($-92 \pm 64 \mu\text{m}$ vs. $-42 \pm 22 \mu\text{m}$, $P=0.0075$) within linear mixed effects models. EG eye specific *ALCSD-BMO* and *ALCSD-BM* compliance exceeded the range of Control eye compliance in 9 and 8 of the 15 EG eyes, respectively. Figure 35 reports similar distribution data for each neural and connective tissue parameter. Figure 36 displays EG eye acute compliance that exceeds Control eye acute compliance in the study animal that demonstrates the greatest amount of Control eye acute compliance. Figure 37 schematically depicts EG eye acute compliance that exceeds Control eye acute compliance in the study animal demonstrating the greatest amount of EG eye acute compliance.

3.7.3 Implications of Early Laminar Hypercompliance in Monkey EG—In this study, OCT compliance testing detected tissue deformation, not structural stiffness. In vivo measurements of structural stiffness will require in vivo measurements of connective tissue architecture, material properties, and/or deformation. Using in vivo OCT ONH imaging to detect ONH connective tissue hypercompliance at the onset of monkey EG is important for two reasons. First, it is a likely manifestation of underlying ONH connective tissue remodeling, failed remodeling, or mechanical failure (Yang et al., 2015a) that suggests it may be a biomarker for the presence of these processes and therefore a means of identifying underlying mechanisms and treatment interventions in future studies. Second, if present and detectable in human ocular hypertensive patients, it may be evidence of an early connective tissue response to the level of mechanical stress and strain they are experiencing, which precedes and/or predicts subsequent RGC injury and loss. In this context it might represent a “structural” precursor not only to “functional” loss, but also to clinically significant “structural” involvement of the neural tissues.

Regarding the mechanistic implications of these findings, we have reviewed the evidence for laminar thickening, scleral canal expansion, posterior laminar bowing, laminar insertion migration, and laminar beam thickness increases and decreases that are present at the detectable onset of unilateral EG in the monkey eye, in the sections above. We have also reviewed the evidence for an increase in the number of laminar beams in early EG as well as the LMA data supporting profound increases in the number of laminar connective tissue voxels. The biomechanical and cellular mechanisms contributing to a decrease of laminar and pp-scleral structural stiffness in the setting of these dramatic increases in laminar connective tissue voxels and volume are currently under study in our laboratory.

3.8 ONH Blood Flow and Blood Flow Autoregulation are Altered Early in Monkey EG

The blood supply to the monkey ONH and retrolaminar optic nerve as determined by vascular casting (Sugiyama et al., 1994) is derived primarily from the central retinal artery for the prelaminar neural and peripapillary RNFL, and from the short posterior ciliary arteries for the lamina beam and retrolaminar circulation (Hayreh, 2001; Sugiyama et al., 1994) (Figures 1, 4 and 5). However, the capillary beds of all three ONH regions are continuously connected (Hayreh, 2001; Sugiyama et al., 1994). Blood flow is autoregulated within the monkey ONH and retina (Alm and Bill, 1973; Liang et al., 2009; Wang et al., 2014a). Choroidal autoregulation in the monkey has not been studied. ONH autoregulation is maintained until the perfusion pressure falls below 30 mmHg (Gejjer and Bill, 1979), and is diminished more by lower levels of blood pressure than by increased levels of IOP (Liang et al., 2009). Following acute IOP elevation, breakdown of the monkey ONH blood brain barrier (Radius and Anderson, 1980) and selective compromise of the immediate peripapillary choroidal circulation (Hayreh and Jonas, 2000), have been described (Figure 5). A large literature has reported a variety of blood flow alterations in monkey EG (Hamasaki and Fujino, 1967; Quigley et al., 1984; Quigley et al., 1985). More recently, laser speckle flowgraphy has been used to demonstrate both blood flow and autoregulation change early in monkey EG (Cull et al., 2013; Liang et al., 2009; Wang et al., 2014b; Wang et al., 2015; Wang et al., 2012).

3.9 Hypercompliance and Stiffening of the Peripapillary and Posterior Sclera in Monkey Early EG by Material Property Testing (Girard et al., 2009c, 2011b)

3.9.1 Background—The sclera is an important factor in ONH biomechanics (Section 2.3, above, Figures 2 and 3). Previous work by a variety of investigators has strongly suggested that the biomechanics of the posterior sclera and lamina cribrosa are tightly coupled (Bellezza et al., 2003a; Girard et al., 2009b; Grytz et al., 2011; Norman et al., 2011; Sigal et al., 2005a; Sigal et al., 2004; Sigal et al., 2011). The pp-sclera contains a circumpapillary ring of collagen and elastin that provides the mechanical boundary conditions for the lamina cribrosa at its insertion into the scleral canal wall (Figure 2) (Hernandez et al., 1987; Quigley et al., 1991). Computational models suggest that scleral stiffness (Sigal et al., 2011) and scleral collagen fiber organization (Girard et al., 2009b; Grytz et al., 2011) dictate the IOP-induced deformation exhibited by the ONH. Interestingly, the sclera exhibits significant biomechanical changes with age (Coudrillier et al., 2015a, b; Fazio et al., 2014a; Fazio et al., 2014b; Girard et al., 2009c), ethnicity (Fazio et al., 2014b), and following exposure to chronic IOP elevation (Coudrillier et al., 2015c; Downs et al., 2005; Girard et al., 2011b), both of which being major risk factors in human glaucoma.

3.9.2 Uniaxial and Inflation pp-scleral Material Property Testing—Downs and co-workers described early alterations in the biomechanical properties of the pp-sclera in monkey early EG using uniaxial testing and linear viscoelastic theory (Downs et al., 2005). That study demonstrated a significant increase in the equilibrium modulus of the pp-sclera from glaucomatous monkey eyes, but no changes were seen in the time-dependent viscoelastic parameters. Girard, working in Downs laboratory, developed an *ex-vivo* method to experimentally measure the 3D deformation pattern and thickness of posterior sclera and used it to study eyes of four young and four old bilaterally normal monkeys following IOP

elevation from 5 to 45 mm Hg (Girard et al., 2009c). In that report, they modeled the posterior sclera as a nonlinear, anisotropic, inhomogeneous soft-tissue using a fiber-reinforced constitutive theory that included stretch-induced stiffening and multi-directionality of the collagen fibers. They then derived eye-specific sets of scleral biomechanical properties based on the experimental observations using an inverse FE method (Girard et al., 2009a). Their results showed that posterior and pp-sclera in old monkeys was significantly stiffer than that from young monkeys and is therefore subject to higher stress but lower strain at all levels of IOP.

Girard and Downs (Girard et al., 2011b), then used the same techniques (Girard et al., 2009a; Girard et al., 2009b; Girard et al., 2009c) to characterize peripapillary and posterior scleral biomechanics in both eyes of eight adult monkeys in which one eye had been exposed to chronic, laser-induced IOP elevations of modest to substantial magnitude and duration. They found that for all EG and Control eyes, the posterior sclera exhibited inhomogeneous, anisotropic, nonlinear biomechanical behavior. Biomechanical changes caused by chronic IOP elevation in the EG eyes were complex and eye-specific.

Specifically, they observed that 1) EG eyes in which the contralateral Control eye displayed a large modulus or thickness were less prone to biomechanical changes; 2) the scleral modulus of EG eyes associated with an inflation pressure of IOP of 10 mmHg was less than that of the contralateral Control eye if the EG eye had experienced a minimal level of chronic IOP elevation; 3) the scleral modulus of EG eyes associated with inflation pressures of 30 and 45 mmHg was greater than that of the contralateral Control eyes in EG eyes that had experienced moderate levels of chronic IOP elevation; and FE modeling based estimates of collagen fiber orientation demonstrated no differences in the EG eyes compared to their contralateral Control eyes. They concluded that stiffening of the sclera follows exposure to moderate levels of chronic experimental IOP elevation in the majority of monkey eyes. However, scleral hypercompliance may precede stiffening or be a unique response to minimal levels of chronic experimental IOP elevation in some monkey eyes.

3.9.3 Implications of Monkey pp-scleral Structural Stiffness Changes in Monkey EG—We have shown that posterior (outward) bowing of the pp-sclera is a principal component of ONH cupping in the monkey EG model by 3D histomorphometry (Figure 19). We have additionally demonstrated that bowing occurs early in the neuropathy within longitudinal post-laser OCT imaging (Section 3.5.3, above) and is eventually accompanied by OCT detected laminar and pp-scleral hypercompliance as measured following acute, manometer-controlled IOP elevations from 10 to 30 mmHG (Section 3.7, above). We have proposed that this outward bowing of the pp-sclera can manifest as a decrease in peripapillary retinal reflectance within both CSLT images and standard clinical disc photographs (Figure 6) (Mackenzie et al., 2009). Finally, we have proposed that alterations in the connective tissue material properties and architecture of the scleral flange should, eventually, influence the volume flow of blood through the posterior ciliary arteries (Burgoyne, 2011) (Figures 5 and 6), and that the peripapillary choroidal atrophy of aging and glaucoma can be explained on this basis, alone (Figures 5 and 32), as originally suggested by Hayreh (Hayreh and Jonas, 2000). Taken together, the data summarized herein

strongly support the importance of the pp-sclera in the optic neuropathy of glaucoma in the monkey and human eye.

4.0 Phenotyping the Optic Neuropathy of Glaucoma in the Monkey and Human Eye Should Include the ONH Connective Tissues (Figures 11, 38, 39)

4.1 Background

Monkey models for unilateral AION (Chen et al., 2008; Miller et al., 2014), optic nerve transection (Burgoyne et al., 1995a; Ing et al., 2016; Morrison et al., 1990; Quigley and Anderson, 1977) and chronic, optic nerve endothelin exposure (Brooks et al., 2004; Cioffi and Sullivan, 1999; Cioffi et al., 2004; Orgul et al., 1996a), as well as bilateral optic neuropathy following primary CSFp lowering (Yang et al., 2014a), have been described. Of these, the neuropathies in the AION and optic nerve transection models both demonstrate mild (transection) to profound (AION) disc swelling followed by diffuse pallor without evident “cupping”. In a longitudinal OCT study in 5 unilaterally transected monkeys, we report anterior rather than posterior laminar deformation within weekly post-transection, OCT data sets acquired through the first 60 days post-transection (Figure 38) (Ing et al., 2016). However, thinning of the RNFL and prelaminar rim tissue was profound (Figure 39), strongly supporting the concept that “prelaminar” or “shallow” forms of “cupping” can be present in “non-glaucomatous” optic neuropathies, due to prelaminar and rim tissue thinning that is not accompanied by laminar deformation and remodeling (Figures 9, 11 and 12).

In the implanted endothelin pump model of unilateral optic nerve vasoconstriction, after preliminary studies in rabbits (Cioffi et al., 1995; Orgul et al., 1996b), optic nerve blood flow reduction in monkeys was characterized (Cioffi and Sullivan, 1999) and localized optic nerve axon loss in the setting of diffuse RNFL loss with shallow cupping was reported in a subset of 12 monkeys (Cioffi et al., 2004). Chauhan then reported optic nerve axon and RGC loss, but infrequent (1 of 21 eyes) ONH topographic change, in the rat endothelin optic neuropathy model (Chauhan et al., 2004). A follow-up monkey study designed to detect longitudinal CSLT and SLP change as well as post-mortem laminar deformation within the endothelin-treated eyes of a separate group of animals failed to achieve detectable optic nerve axon loss in the endothelin eyes, and its results were therefore uninterpretable (personal communication from the co-principal investigators, Jack Cioffi and Claude Burgoyne). In a later study in 5 rhesus macaques unilaterally implanted with endothelin pumps and followed for 1.5 years (Brooks et al., 2004), no significant changes in ONH morphology or ONH blood flow velocity were detected by CSLT and laser Doppler flowmetry, respectively. In that study, while optic nerve axon counts were also not significantly decreased in the endothelin treated eyes, IHC evidence of altered metabolic activity was detected in the contralateral visual cortex.

Yang and co-authors recently reported diffuse RNFL and optic nerve rim thinning in 2 of 4 monkeys following primary surgical CSFp lowering (Yang et al., 2014a). A third monkey demonstrated a single nerve fiber hemorrhage but no other change. While quantitative assessment was not reported, no qualitative evidence of laminar deformation was present

within the published OCT images. Subsequent unpublished quantification has confirmed that there was no OCT-detected laminar deformation within the four studied animals (Personal communication, Ningli Wang). While the appearance of this neuropathy is not glaucomatous by the criteria suggested above, the model is important because it demonstrates that primary CSFp lowering at “normal” levels of IOP is a risk factor for RGC axon loss in a subset of monkey eyes. It therefore also suggests that in a given eye, a relative increase in the translaminar pressure gradient (by whatever cause) may be a risk factor for RGC axon loss at all levels of IOP. However, the fact that primary CSFp lowering in these eyes did not result in laminar deformation and remodeling is also important. It supports the notion that scleral tensile effects on the lamina (Section 2.4, above, Figure 3) even at normal levels of IOP, likely exceed the direct effects of the increased translaminar pressure difference on the lamina that results from CSFp lowering.

Interestingly, though it was not reported in the original study, the RNFL thinning that occurred in 2 of the 4 monkeys stopped after 3 to 6 months of low CSFp, though low CSFp persisted for the full 2 years of post CSFp lowering observation (personal communication, Ningli Wang). The investigators have hypothesized that perhaps only a subset of the ONH RGC axons in a given ONH are susceptible to this magnitude of increase in the translaminar pressure gradient. If this is true, does this model have the potential to identify those axons that are most susceptible to the translaminar pressure gradient in a larger group of animals? Is this susceptibility higher in old compared to young animals? Is the regional pattern of this axon loss similar to age-related axon loss in the monkey eye? Is the pattern similar to the pattern of axon loss in early EG? Finally, apart from the pattern of axon loss, what is the size distribution of the remaining axons? These questions are now important to address.

4.2 Implications for Phenotyping in all Experimental Glaucoma Models

As noted above, there are no experimental models of a glaucomatous optic neuropathy that do not require IOP elevation (i.e. “normal tension glaucoma” models) in the monkey or any other species. Those that have so far been suggested have either presented no characterization of the ONH phenotype (Joachim et al., 2013; Wax et al., 2008), or have been shown to possess an ONH phenotype that is non-glaucomatous (Brooks et al., 2004; Yang et al., 2014a). Creating a “normal tension glaucoma model” remains an important research target for our field because it will provide insight into how a primary, non-IOP-related insult, such as inflammation (Tezel and Wax, 2004; Tezel et al., 2012) or autoimmunity (Grus et al., 2008), can influence the physiology of the ONH tissues in such a way that the connective tissues become susceptible to deformation and remodeling at “normal levels” of IOP-related stress and strain. The data summarized in this report emphasize the importance of ONH connective tissue deformation and remodeling to the phenotype of glaucoma in the monkey eye. The models of primary CSFp lowering and optic nerve transection, as well as clinical experience with peripheral retinal photocoagulation in humans tell us that primary insult to the RGC soma and axons outside of the ONH (pan retinal photocoagulation and optic nerve transection) or within it (CSFp) leads to a pale optic nerve that is non-glaucomatous in appearance and behaviour.

It is therefore interesting to note that the arteritic form of AION has often been described to create “glaucomatous” cupping in a subset of arteritic AION eyes (Greenfield, 1999; Trobe et al., 1980a; Trobe et al., 1980b). While in some AION eyes this may be shallow, “prelaminar” cupping that does not demonstrate a connective tissue component, if clear laminar deformation can be demonstrated in arteritic AION, does it suggest that inflammation may be an agent that is capable of primarily (or secondarily) altering ONH connective tissue homeostasis? OCT phenotyping strategies that include the ONH connective tissues are necessary to determine if candidate “*normal tension glaucoma*” optic neuropathies in monkeys and humans are, in fact, “glaucomatous” or “non-glaucomatous”.

5.0 Next Steps and New Directions

5.1 Foveal-BMO Regionalization of 3D HMRN Data Sets (Figures 40–41) (Burgoyne, 2015b; Lockwood et al., 2015)

The 3D histomorphometric and OCT ONH connective tissue data summarized in Section 3.0, above, are “global” in nature, meaning data from the entire ONH was analyzed without addressing clinical quadrants or regions. The purpose of this section is to introduce the logic for foveal-BMO (FoBMO) regionalization of post-mortem and in vivo posterior pole data sets as it has been implemented in our laboratory for monkey and human eyes.

To date, there has been no anatomic logic for the assignment of “superior”, “inferior”, “nasal” and “temporal” to ONH anatomy within clinical imaging or post mortem tissues. In most post-mortem studies this assignment, when described, has been done based on the clinical appearance of the ONH and vascular arcades within in vivo or post-mortem fundus images. Clinical images are regionalized relative to a nasal temporal axis that is assumed to be parallel to the horizontal axis of the acquired image frame without regard to the anatomic relationship between the ONH and the fovea. We have argued for linking ONH as well as peripapillary retinal and macula regionalization to the axis between the centroid of BMO and the fovea (the FoBMO axis), (Figure 40) (Chauhan and Burgoyne, 2013).

Within the monkey EG model it is imperative to regionalize the EG and Control eye identically so as to most fairly compare EG eye regional change to the appropriate region of the Control eye. The logic for using the FoBMO axis to regionalize ONH, RNFL, and macular anatomy has been suggested by previous studies of RNFL anatomy and its relationship to structure-function correlation (Garway-Heath et al., 2000; Harwerth et al., 2010; Hood and Kardon, 2007; Jansonius et al., 2009; Jonas et al., 1989; Patel et al., 2012; Schiefer et al., 2003; Turpin et al., 2009). As per our 2015 publication describing our LMA method (Lockwood et al., 2015), we estimate the location of the FoBMO axis relative to the vertical and horizontal axes of the embedded 3D HMRN so as to impose a consistent grid of twelve 30° sectors on the 3D HMRN LC anatomy of each eye (Figure 40). Left eye data is digitally converted to right eye orientation (Figure 41) allowing defensible sectoral and subsectoral EG versus Control eye LMA comparisons to occur (Figure 42). The reproducibility of this process has been previously reported to be ± 3.8 degrees (Lockwood et al., 2015), suggesting that the variability of FoBMO 30° sectoral assignment is small compared to the size of each sector.

Our use of the FoBMO axis to regionalize ONH anatomy within post-mortem tissues (Lockwood et al., 2015) marks a demarcation from all of our own and other characterizations of the monkey ONH which have been regionalized through clinical inspection of in vivo or ex vivo fundus photos without regard for the fovea (Burgoyne et al., 2004; Yang et al., 2009b). Accomplishing FoBMO regionalization of post-mortem 3D HRMN data is allowing us to pursue new techniques (outlined in the sections that follow) that require anatomically consistent regionalization within in vivo and post-mortem data from the same eye. The implementation of FoBMO orientation for OCT data sets has recently been accomplished both retrospectively (He et al., 2014a) and at the time of OCT data set acquisition (Section 5.3, below) (Chauhan and Burgoyne, 2013; Chauhan et al., 2015).

5.2 Foveal-BMO Pattern of Laminar Microarchitecture Change (Figure 42)

Our method for reporting EG versus Control eye LMA differences within FoBMO-based, 30° sub-sectors is depicted in Figure 42. We will soon report (Burgoyne et al., 2015), the FoBMO sub-sectoral character of EG eye LMA parameter change in the 14 early EG animals of Section 3.3, above (manuscript in preparation) (Reynaud et al., 2016). These analyses will form the foundation for future studies (outlined below) in which Control eye LMA data and/or sub-sectoral IOP-related stress and strain (from FE models) (Roberts et al., 2009) will be used to predict the FoBMO location of greatest EG eye LMA change (Burgoyne et al., 2015), post-laser OCT change (Yang et al., 2015b), and/or retrolaminar optic nerve axon loss (Reynaud et al., 2012).

5.3 Foveal-BMO OCT Phenotyping in Monkey and Human eyes (Figures 43–47) (Burgoyne, 2015a; Chauhan and Burgoyne, 2013; He et al., 2014a)

Based in part on our findings in monkey imaging (Strouthidis et al., 2009a), and also on the same studies of RNFL anatomy and its relationship to structure-function correlation mentioned previously (Garway-Heath et al., 2000; Harwerth et al., 2010; Hood and Kardon, 2007; Jansonius et al., 2009; Jonas et al., 1989; Patel et al., 2012; Schiefer et al., 2003; Turpin et al., 2009), we have suggested (Burgoyne, 2015b; Chauhan and Burgoyne, 2013) that OCT data sets of the ONH, RNFL and macula should not only be regionalized relative to the FoBMO axis, but OCT data acquisition should be organized relative to it as well. Figures 43–47 illustrate our strategy for OCT phenotyping the ONH, RNFL and Macula of the monkey (and human) (Burgoyne, 2015a) eye. In our laboratory, post-mortem 3D HRMN, IHC, optic nerve axon counts, and scanning block face electron microscopy (SBFEM) 3D reconstructions of the monkey EG eye are being colocalized to the pre-sacrifice, OCT EG eye change-from-baseline map (Figure 48) (Yang et al., 2015b). Other laboratories are employing OCT phenotyping using similar strategies in their work (Patel et al., 2014a; Patel et al., 2014b). This approach to OCT data set acquisition and parameterization has now been fully implemented for clinical OCT imaging in humans (Chauhan and Burgoyne, 2013) and its normative database is beginning to be characterized (Chauhan et al., 2015).

5.4 Timing and Foveal-BMO Pattern of OCT ONH/RNFL/Macula Change

Figure 48 demonstrates our use of FoBMO sectoral characterization of OCT change onset and rates of change in the 4 young and 4 old early EG animals carried to a CSLT onset point,

summarized in Section 3.5, (for global ONH and RNFL data), above (He et al., 2014b). In this figure, the FoBMO sectoral prevalence of event based onset and rates of change are summarized for all 8 animals. However eye-specific EG and Control eye maps for each animal, (not shown), can also be generated and compared to post-mortem LMA, EG eye versus Control eye differences, FE modelling outputs and retrolaminar axon counts. In methods that are under development, quantitative IHC (Figure 49) (Stowell et al., 2016), will be co-localized to longitudinal OCT change (Figure 50, section 5.9 below) as will quantitative SBFEM, (Figure 51, section 5.10 below).

5.5 Timing and Foveal-BMO Pattern of RGC Axon Loss

Diffuse and focal patterns of RNFL loss has been reported in monkey EG (Jonas and Hayreh, 1999; Yang et al., 2015b). Early descriptions of monkey EG eye optic nerve axon loss suggested the superior and inferior axons were most susceptible to injury from chronic IOP elevation (Quigley and Addicks, 1980). A greater susceptibility of large versus small RGCs and RGC axons has also been suggested (Dandona et al., 1991; Desatnik et al., 1996; Glovinsky et al., 1991; Glovinsky et al., 1993; Wagnanski et al., 1995) but the interpretation of these findings continues to be challenged (Cooper et al., 2016; Morgan et al., 2000). We are currently processing the control and EG eye axon counts from more than 60 unilateral EG animals employing 100% axon counting techniques (Reynaud et al., 2012). While an overall superior and inferior susceptibility may emerge, preliminary analyses suggest that the EG eye-specific pattern of axon loss is quite variable. Comparisons to underlying laminar microarchitecture (Lockwood et al., 2015), prelaminar OCT ONH and RNFLT change (He et al., 2014b; Yang et al., 2015b) and continuum FEM outputs (Roberts et al., 2009; Roberts et al., 2010a; Roberts et al., 2010b) are underway. The question of axon size-related susceptibility will also be revisited.

5.6 Age Effects on the Neuropathy

Three age-related issues are currently under study in our laboratory. First, we have demonstrated that older (18.6 – 21.9 yrs) monkey eyes demonstrate less laminar deformation for a given magnitude of cumulative IOP insult than young (1.4 – 2.6 yrs) monkey eyes – when measurements are made both (longitudinally) up to and (cross-sectionally) at the onset of early EG (Yang et al., 2014b) (Section 3.6 and Figures 32 – 33). These data indirectly suggest that there are structural stiffness differences in young and old monkey and human eyes (Ren et al., 2014) that influence the “depth” of manifest “cupping” early in monkey EG.

We are separately characterizing the FoBMO pattern of OCT minimum rim width (MRW) and RNFLT change (Figure 48) within 8 young versus 8 old animals (manuscript in preparation) (Yang et al., 2015b). The purpose of this study is two-fold. First to document the FoBMO sectoral pattern of OCT MRW and RNFLT change in early EG to compare it to the FoBMO sectoral pattern of cross-sectional age effects in normal monkeys, as has been done for humans (Chauhan et al., 2015; See et al., 2009). Second, to assess the relative susceptibilities of the young and old eyes to RNFLT and orbital optic nerve axons loss, to their given cumulative IOP insults, through early onset and progression of RGC damage. The initial analyses of these data, for the first 4 young and 4 old animals, suggest that age-

related differences in RGC axon susceptibility between 2 – 3 year old animals compared to 18 – 22 year old animals are not obvious (He et al., 2014b; Yang et al., 2014b). More extensive studies of “very old” monkeys (aged 28 – 40 yrs) and/or telemetric IOP insult characterization (Downs et al., 2011) may be necessary to detect these differences in the monkey eye. Finally, studies to detect age-related differences in connective tissue remodeling (separate from axon loss) are also underway.

5.7 Laminar Deformation, Migration and Retrolaminar Septal Recruitment Should Influence Retrolaminar Astrocyte Myelin Remodeling and Transmitophagy in Aging and Glaucoma (Figure 49)

We hypothesize that astrocyte retrolaminar myelin phagocytosis plays an essential part in the dynamic between oligodendrocytes and astrocytes that halts myelin at the back of the lamina in all normal primate eyes. Myelin remodeling should be linked to early EG connective tissue remodeling through the process of retrolaminar septal recruitment (Section 3.4, above, Figure 49) (Roberts et al., 2009). In addition to phagocytosing myelin, retrolaminar astrocytes also internalize and degrade mitochondria from adjacent RGC axons in a process called “transmitophagy” (Davis et al., 2014; Nguyen et al., 2011). Marsh-Armstrong and Ellisman have shown that transmitophagy and myelin phagocytosis are homeostatic processes in normal mice and hypothesize that they may be overwhelmed in mouse glaucoma models (Davis et al., 2014; Nguyen et al., 2011). We are currently testing the hypotheses that they are diminished in aged monkeys and overwhelmed in early monkey EG using the proteomic, IHC and electron microscopic (EM) techniques as outlined in Sections 5.8 – 5.10, below.

5.8 Quantitative ONH Proteomics in Monkey Early EG

State of the art iTRAQ Mass Spec quantification of ONH (Burgoyne et al., 2014), pp-scleral (Crabb et al., 2014), retinal (Jang et al., 2014) and ON (Zhang et al., 2014) tissues from the Control and EG eyes of 3 adult early EG animals have been completed using iTRAQ tagging Liquid Chromatography Tandem Mass Spectrometry (Bollinger et al., 2011, 2012; Crabb et al., 2015; Crabb et al., 2010; Yuan et al., 2010). To date, more than 1100 proteins have been identified, with 55 and 68 proteins achieving our most stringent criteria for increased and decreased expression, respectively. Ingenuity pathway analysis of our proteomic data suggest that leukocyte migration, cell movement of leukocytes, cell death, cell movement of phagocytes, cellular infiltration, and cell movement of myeloid cells are most strongly supported by increased EG eye protein expression. Microtubule dynamics, formation of plasma membrane protrusions and projections, morphology of neuroglia, neuritogenesis, morphology of neurites, development of neurons, and branching of neurites are the most important annotations for decreased protein expression. A manuscript is in preparation reporting the ONH proteomic findings which will include quantitative IHC (Section 5.9, below) confirmation of expression changes for 10 proteins identified by proteomics within tissues from a separate group of 4 early EG animals. Early EG proteomic analyses will be expanded to 12 young and 12 old animals in work that has just been funded. This work will be linked to the proteomic analysis of longitudinally acquired serum and CSF samples from the same animals to seek serum biomarkers of these ONH processes.

5.9 OCT Co-localized FoBMO Quantitative IHC in Monkey Early EG (Figures 50–51)

Our method to regionally quantify four IHC signals and detect animal-specific and experiment-wide, between-eye signal differences within six ONH tissues is in preparation for publication and is summarized in Figure 50. This technique was developed for serial vertical sagittal sections of an ONH trephine in a group of animals in which high-resolution OCT data sets on the day of sacrifice could not be obtained. However, in a separate group of 4 young and 4 old IHC-dedicated early EG animals that have been longitudinally OCT imaged relative to the FoBMO axis, the ONH trephine tissues have been serial sectioned parallel to the same (FoBMO) axis (Figure 51). In future studies using these tissues, the EG and Control eye sections will be selected such that protein expression changes will be precisely co-localized to FoBMO-oriented 30 degree (clock hour) sectors (Figure 51).

Such co-localization will allow the comparison of both longitudinal OCT ONH/RNFL change and retrobulbar optic nerve axon counts (each quantified within the same FoBMO 30 degree segments) to EG versus Control eye differences in protein expression. Because a monkey that has been sacrificed at the detection of 7 to 10% global RNFL thinning by OCT may have 30 degree sectoral axon loss that ranges from 0 to 25% (Fortune et al., 2015; Fortune et al., 2016a), paraffin sections from EG eye 30 degree sectors with 0–10% and 11–20% axon loss (compared to the contralateral control) may eventually provide meaningful insights into protein expression changes that precede, coincide and progress from the onset of detectable axonal injury and or loss. Changes in protein expression that precede detectable axon loss (by counts), may then be staged by co-localized IHC markers of axon cytoarchitecture disruption (Fortune et al., 2014). Taken together, a long-term goal of this work will be to use these techniques to inform our mechanistic studies while enhancing the interpretation of clinical OCT imaging to better inform human glaucoma patient care.

5.10 OCT Co-localized FoBMO Quantitative Scanning Block-Face Electron Microscopy in Monkey Early EG (Figure 52)

We are currently studying a separate group of 4 young and 4 old, EM-dedicated, early EG animals that have also been longitudinally OCT imaged relative to the FoBMO axis. In these animals, the ONH trephine tissues have been vibratome sectioned (100 μ m thick) parallel to the same (FoBMO) axis (Figure 52). As described in Section 5.7, above, Ellisman has previously used EM (Berlanga et al., 2011; Mills et al., 2015; West et al., 2010; Wilhelmsson et al., 2006) to characterize astrocyte, axon and myelin interactions including phagocytosis of myelin (Nguyen et al., 2011) and transmitophagy of axonal mitochondria (Davis et al., 2014) (in collaboration with Marsh-Armstrong). Our strategy for sectioning FoBMO parallel, 100 μ m thick vibratome sections, μ CT scanning each section, acquiring a peripheral or central transmission electron microscopy (TEM) montage scan (containing the prelaminar, laminar, and retrolaminar tissues) (n=2) to position a single peripheral (or central) 200 \times 200 \times 50 μ m scanning block face EM region of interest relative to known axon loss (by counts) is illustrated in Figure 52. We are developing stereological and 3D delineation approaches to grade or measure TEM and/or scanning block face EM phenomena of interest including myelin phagocytosis, transmitophagy, tissue invasion by blood borne myeloid cells, axonal cytoarchitectural disruption, and laminar beam fibroblast myofibroblast transformation. Our studies of EG and Control eye EM regions of interest will

also focus on EG eye FoBMO sectors with 0–10% and 11–20% axon loss relative to their Control eyes. Similar to the IHC strategies outlined above, EM changes that precede detectible axon loss (by counts) will be staged by co-localized EM markers of axon cytoarchitecture disruption. Correlations to co-localized longitudinal OCT change will then be sought.

6.0 Implications for ONH Neuroprotective Targets in Glaucoma

To date, most neuroprotective interventions in glaucoma have been focused on preserving the retinal ganglion cell soma and/or its axonal connection to the brain. Because enhancing RGC axon function and RGC somal survival are essential to vision preservation in glaucoma, we expect these studies to generate important candidates for human neuroprotection, whether their targets are in the retina, the ONH, the orbital optic nerve, or the brain.

Recently, treatment interventions to stiffen (Spoerl et al., 2005; Strouthidis and Girard, 2013; Terai et al., 2012; Thornton et al., 2009), soften (Spoerl et al., 2005), and alter the wound healing properties of the posterior scleral tissues (Quigley et al., 2015) have been employed in a number of laboratories. Quigley and colleagues (Quigley et al., 2015), used losartan (an inhibitor of TGF β signalling) in mice given experimental IOP elevations and unilateral optic nerve transections, respectively, and prevented significant RGC loss compared to treatments with a variety of control agents. They additionally demonstrated that losartan inhibited effects of experimental glaucoma including reduction in extracellular signal related kinase activity and modification of glaucoma-related changes in scleral thickness and creep under controlled IOP. While the specific mechanisms responsible for neuroprotection in these studies were not clear, the authors proposed that the neuroprotective effect of osartan in mouse glaucoma is associated with adaptive changes in the sclera expressed at the ONH.

A series of genomic studies in the DBA2J mouse model of glaucoma by Howell and colleagues (Howell et al., 2011; Howell et al., 2013; Howell et al., 2012) have reported important roles for ONH inflammation, monocyte infiltration, and the complement and endothelin pathways early in the optic neuropathy of chronic IOP elevation in this species. Johnson and colleagues (Johnson et al., 2015; Johnson et al., 2011) have reported ONH genomic data in the induced unilateral rat model that strongly support inflammation, cellular proliferation and migration. We have reviewed the work of Marsh-Armstrong and Ellisman on retrolaminar astrocyte phagocytosis and transmitophagy in Section 5.7 Our preliminary proteomic (Section 5.8), IHC (Section 5.9) and EM (Section 5.10) data, strongly suggest that similar cellular processes are present within the monkey ONH early in the neuropathy.

We predict that the outcomes of our current studies will contribute to the development of ONH neuroprotective interventions as follows. First, altered proteins in monkey early EG will contribute to the molecular staging of early structural damage in human glaucoma and candidate biomarkers for its systemic detection. Second, establishing connective tissue remodeling, retrolaminar myelin alteration, phagocytosis, inflammation, and monocyte invasion as core ONH components of monkey aging and early EG will generate novel ONH neuroprotective targets for human glaucoma. Third, identifying important mechanisms of

ONH aging will contribute to these neuroprotective targets. Fourth, IHC and electron microscopic validation of early OCT ONH structural glaucoma detection in monkey EG will contribute to the establishment of early longitudinal OCT change (independent of visual field criteria) as a legitimate early outcome measure for ONH targeted neuroprotective clinical trials in glaucoma.

7.0 Summary of Core Findings, Concepts and Predictions

- Biomechanically, the ONH is a unique environment, wherein the energy demands of the RGC axon mitochondria are high and the mechanisms of nutrient delivery from the capillaries to the center of the axon bundles are not known.
- ONH aging, glaucoma at normal levels of IOP, and glaucoma that only occurs at elevated levels of IOP represent a continuum of ONH susceptibility to a common set of IOP-related and non-IOP-related risk factors experienced over a lifetime.
- RGC axonal insult is central to vision loss in glaucoma but it is not the organizing pathophysiology of ONH aging or the optic neuropathy of glaucoma.
- Optic nerve head blood flow, connective tissue deformation and remodeling, astrocyte nutrient delivery to the RGC axon, astrocyte myelin phagocytosis, and astrocyte transmitophagy should be central determinants of ONH homeostasis at all ages and are therefore targets for ONH neuroprotection in aging and glaucoma.
- Achieving stable vision in glaucoma, as well as RGC axon regeneration through glaucomatous ONH tissues, will require neuroprotective treatments directed to these ONH phenomena.
- The genetic contributions to ONH biomechanics, ONH homeostasis, ONH aging, and ONH susceptibility to glaucomatous damage are, at present, unknown.

8.0 Acknowledgements and Disclosures

Portions of the Tables, Figures and text of this manuscript have been taken from publications in which Dr. Burgoyne is the senior author (He et al., 2014b; Ing et al., 2016; Ivers et al., 2016; Lockwood et al., 2015; Reynaud et al., 2016; Yang et al., 2015a). For figures, this is stated clearly in the legend. For text, the original manuscript is cited.

The work reported herein has been supported in part by USPHS grants R01EY011610 (CFB) and R01EY021281 (CFB) from the National Eye Institute, National Institutes of Health, Bethesda, Maryland; a grant from the American Health Assistance Foundation, Rockville, Maryland (CFB); a grant from The Whitaker Foundation, Arlington, Virginia (CFB); a Career Development Award (CFB); The Legacy Good Samaritan Foundation, Portland, Oregon; and the Sears Trust for Biomedical Research, Mexico, Missouri.

The authors are grateful to the following individuals for their contributions to this work. Richard Hart, PhD was Chairman of the Department of Biomechanical Engineering at Tulane University in 1993 and agreed to collaborate to study the monkey ONH using

engineering principles. His support brought with it his colleague J. K. Francis Suh, PhD to study the sclera and our first two PhD students, Anthony Bellezza and Crawford Downs. Both made important contributions, to 3D histomorphometric reconstruction and quantification and Dr. Downs to scleral material properties.

A series of Engineering PhD students and Post-Docs in Dr. Downs' Laboratory made essential contributions to the performance, quantification and interpretation of ONH 3D histomorphometric reconstructions including Vincente Grau, PhD, Mike Roberts, PhD; Michael Girard, PhD; Ian Sigal, PhD, and Rafael Grytz, PhD. A separate group of Dr. Burgoyne's post-doctoral fellows have worked on CSLT, 3D Histomorphometric or OCT quantification and these have included: Aurora Heickel, MD; Nicholas Strouthidis, MD, PhD; Ruojin Ren MD, PhD; Marta Pazos, MD, PhD; Camilla Zangali, MD; Jonathan He, PhD; and Kevin Ivers, PhD. Among these Nicholas Strouthidis was integral to the early translation of 3D histomorphometric techniques to monkey and human OCT imaging. Conversations with our current collaborators, Ross Ethier, PhD, Andrew Feola, PhD, Chris Girkin, MD, Massimo Fazio, PhD, John Morrison, MD, Elaine Johnson, PhD, John Crabb, PhD, Mark Ellisman, PhD, Eric Bushong, PhD, and Nick Marsh-Armstrong, PhD have greatly influenced the direction and interpretation of our most recent 3D histomorphometric, finite element modelling, proteomic, electron microscopic, and immunohistochemical work.

The Optic Nerve Head Research Laboratory has benefited from a long line of dedicated technicians, research engineers, computer scientists and research scientists without whom none of the science summarized herein would have been possible. Technicians have included Liqian Qui, MD, Stephanie Haggard, Pris Zhou, and Wenxia Wang. Computer scientists have included Thomas Jones, Budd Hiron and Jonathan Grimm. It has also received essential ideas and support from an extraordinary group of Devers collaborators that includes Brad Fortune, PhD, Lin Wang, MD, PhD, Grant Cull, Shaban Demirel, PhD and Steve Mansberger, MD. Our work is only possible because of the many dedicated animal care workers and veterinarians at the Louisiana State University Health Center in New Orleans and the Legacy Research Institute in Portland who have provided excellent support to our animals.

The laboratory is fortunate to be in its 20th year of NIH funding to study aging and EG in the monkey eye. Dr Burgoyne is a consultant to and receives unrestricted research support from Heidelberg Engineering to translate monkey findings to human glaucoma patient imaging as part of a second NIH R01. In this work, Balwantray Chuanhan, PhD and Gerhard Zinser, PhD have been close collaborators. Dr. Burgoyne receives occasional travel support but holds no patents or intellectual property of any form and receives no honorarium or personal income from this collaboration.

It is not possible to cite all colleagues and collaborators who have made important contributions to the conception, design, execution and interpretation of this work. For those we have missed, we sincerely apologize. Finally the authors would like to thank Joanne Couchman for her dedicated assistance in editing and submitting this manuscript.

References

- Alm A, Bill A. The oxygen supply to the retina. II. Effects of high intraocular pressure and of increased arterial carbon dioxide tension on uveal and retinal blood flow in cats. A study with radioactively labelled microspheres including flow determinations in brain and some other tissues. *Acta Physiol Scand.* 1972; 84:306–319. [PubMed: 4553229]
- Alm A, Bill A. Ocular and optic nerve blood flow at normal and increased intraocular pressures in monkeys (*Macaca irus*): a study with radioactively labelled microspheres including flow determinations in brain and some other tissues. *Exp Eye Res.* 1973; 15:15–29. [PubMed: 4630581]
- Anderson DR, Hendrickson A. Effect of intraocular pressure on rapid axoplasmic transport in monkey optic nerve. *Invest Ophthalmol.* 1974; 13:771–783. [PubMed: 4137635]
- Anderson DR, Hoyt WF. Ultrastructure of intraorbital portion of human and monkey optic nerve. *Arch Ophthalmol.* 1969; 82:506–530. [PubMed: 4981187]
- Anderson DR, Hoyt WF, Hogan MJ. The fine structure of the astroglia in the human optic nerve and optic nerve head. *Trans Am Ophthalmol Soc.* 1967; 65:275–305. [PubMed: 4965878]
- Asai T, Katsumori N, Mizokami K. Retinal ganglion cell damage in human glaucoma. 2. Studies on damage pattern. *Nihon Ganka Gakkai Zasshi.* 1987; 91:1204–1213. [PubMed: 3448905]
- Bellezza AJ, Hart RT, Burgoyne CF. The optic nerve head as a biomechanical structure: initial finite element modeling. *Invest Ophthalmol Vis Sci.* 2000; 41:2991–3000. [PubMed: 10967056]
- Bellezza AJ, Rintalan CJ, Thompson HW, Downs JC, Hart RT, Burgoyne CF. Anterior scleral canal geometry in pressurised (IOP 10) and non-pressurised (IOP 0) normal monkey eyes. *Br J Ophthalmol.* 2003a; 87:1284–1290. [PubMed: 14507767]
- Bellezza AJ, Rintalan CJ, Thompson HW, Downs JC, Hart RT, Burgoyne CF. Deformation of the lamina cribrosa and anterior scleral canal wall in early experimental glaucoma. *Invest Ophthalmol Vis Sci.* 2003b; 44:623–637. [PubMed: 12556392]
- Berlanga ML, Phan S, Bushong EA, Wu S, Kwon O, Phung BS, Lamont S, Terada M, Tasdizen T, Martone ME, Ellisman MH. Three-dimensional reconstruction of serial mouse brain sections: solution for flattening high-resolution large-scale mosaics. *Front Neuroanat.* 2011; 5:17. [PubMed: 21629828]
- Bollinger KE, Crabb JS, Yuan X, Putliwala T, Clark AF, Crabb JW. Quantitative proteomics: TGFbeta(2) signaling in trabecular meshwork cells. *Invest Ophthalmol Vis Sci.* 2011; 52:8287–8294. [PubMed: 21917933]
- Bollinger KE, Crabb JS, Yuan X, Putliwala T, Clark AF, Crabb JW. Proteomic similarities in steroid responsiveness in normal and glaucomatous trabecular meshwork cells. *Mol Vis.* 2012; 18:2001–2011. [PubMed: 22876128]
- Braakman ST, Pedrigo RM, Read AT, Smith JA, Stamer WD, Ethier CR, Overby DR. Biomechanical strain as a trigger for pore formation in Schlemm's canal endothelial cells. *Exp Eye Res.* 2014; 127:224–235. [PubMed: 25128579]
- Broadway DC, Nicoleta MT, Drance SM. Optic disk appearances in primary open-angle glaucoma. *Surv Ophthalmol.* 1999; 43(Suppl 1):S223–243. [PubMed: 10416767]
- Brooks DE, Kallberg ME, Cannon RL, Komaromy AM, Ollivier FJ, Malakhova OE, Dawson WW, Sherwood MB, Kuekerichkina EE, Lambrou GN. Functional and structural analysis of the visual system in the rhesus monkey model of optic nerve head ischemia. *Invest Ophthalmol Vis Sci.* 2004; 45:1830–1840. [PubMed: 15161847]
- Burgoyne C. The morphological difference between glaucoma and other optic neuropathies. *J Neuroophthalmol.* 2015a; 35(Suppl 1):S8–S21. [PubMed: 26274837]
- Burgoyne CF. A biomechanical paradigm for axonal insult within the optic nerve head in aging and glaucoma. *Exp Eye Res.* 2011; 93:120–132. [PubMed: 20849846]
- Burgoyne CF. The non-human primate experimental glaucoma model. *Exp Eye Res.* 2015b; 141:57–73. [PubMed: 26070984]
- Burgoyne CF, Downs JC. Premise and prediction-how optic nerve head biomechanics underlies the susceptibility and clinical behavior of the aged optic nerve head. *J Glaucoma.* 2008; 17:318–328. [PubMed: 18552618]

- Burgoyne CF, Downs JC, Bellezza AJ, Hart RT. Three-dimensional reconstruction of normal and early glaucoma monkey optic nerve head connective tissues. *Invest Ophthalmol Vis Sci*. 2004; 45:4388–4399. [PubMed: 15557447]
- Burgoyne CF, Downs JC, Bellezza AJ, Suh JK, Hart RT. The optic nerve head as a biomechanical structure: a new paradigm for understanding the role of IOP-related stress and strain in the pathophysiology of glaucomatous optic nerve head damage. *Prog Retin Eye Res*. 2005; 24:39–73. [PubMed: 15555526]
- Burgoyne CF, Lockwood H, Reynaud J, Gardiner SK, Grimm J, Libertaux V, Downs JC, Yang H. Eye-Specific Lamina Cribrosa (LC) Microarchitectural (LMA) Change in Non-Human Primate (NHP) Early Experimental Glaucoma (EG) by Region. *IOVS*. 2015; 56 ARVO E-Abstract 6153.
- Burgoyne CF, Quigley HA, Thompson HW, Vitale S, Varma R. Early changes in optic disc compliance and surface position in experimental glaucoma. *Ophthalmology*. 1995a; 102:1800–1809. [PubMed: 9098280]
- Burgoyne CF, Quigley HA, Thompson HW, Vitale S, Varma R. Measurement of optic disc compliance by digitized image analysis in the normal monkey eye. *Ophthalmology*. 1995b; 102:1790–1799. [PubMed: 9098279]
- Burgoyne CF, Stowell C, Jang G, Zhang L, Willard B, Crabb JS, Crabb JW. Non-Human Primate (NHP) Optic Nerve Head (ONH) Proteomic Change In Early Experimental Glaucoma (EEG). *IOVS*. 2014; 55 ARVO E-Abstract 4555.
- Carolynne, AK. Chapter III: Two Parameter Gamma Distribution. In: Carolynne, AK., editor. *Gamma and Related Distributions*. Books on Demand. Norderstedt, Germany: 2014. p. 6-27.
- Chauhan BC, Burgoyne CF. From clinical examination of the optic disc to clinical assessment of the optic nerve head: a paradigm change. *Am J Ophthalmol*. 2013; 156:218–227. e212. [PubMed: 23768651]
- Chauhan BC, Danthurebandara VM, Sharpe GP, Demirel S, Girkin CA, Mardin CY, Scheuerle AF, Burgoyne CF. Bruch's Membrane Opening Minimum Rim Width and Retinal Nerve Fiber Layer Thickness in a Normal White Population: A Multicenter Study. *Ophthalmology*. 2015; 122:1786–1794. [PubMed: 26198806]
- Chauhan BC, LeVatte TL, Jollimore CA, Yu PK, Reitsamer HA, Kelly ME, Yu DY, Tremblay F, Archibald ML. Model of endothelin-1-induced chronic optic neuropathy in rat. *Invest Ophthalmol Vis Sci*. 2004; 45:144–152. [PubMed: 14691166]
- Chauhan BC, O'Leary N, Almobarak FA, Reis AS, Yang H, Sharpe GP, Hutchison DM, Nicolela MT, Burgoyne CF. Enhanced detection of open-angle glaucoma with an anatomically accurate optical coherence tomography-derived neuroretinal rim parameter. *Ophthalmology*. 2013; 120:535–543. [PubMed: 23265804]
- Chauhan BC, Sharpe GP, Hutchison DM. Imaging of the temporal raphe with optical coherence tomography. *Ophthalmology*. 2014; 121:2287–2288. [PubMed: 25156139]
- Chen CS, Johnson MA, Flower RA, Slater BJ, Miller NR, Bernstein SL. A primate model of nonarteritic anterior ischemic optic neuropathy. *Invest Ophthalmol Vis Sci*. 2008; 49:2985–2992. [PubMed: 18326695]
- Chen TC. Spectral domain optical coherence tomography in glaucoma: qualitative and quantitative analysis of the optic nerve head and retinal nerve fiber layer (an AOS thesis). *Trans Am Ophthalmol Soc*. 2009; 107:254–281. [PubMed: 20126502]
- Cioffi GA, Orgul S, Onda E, Bacon DR, Van Buskirk EM. An in vivo model of chronic optic nerve ischemia: the dose-dependent effects of endothelin-1 on the optic nerve microvasculature. *Curr Eye Res*. 1995; 14:1147–1153. [PubMed: 8974844]
- Cioffi GA, Sullivan P. The effect of chronic ischemia on the primate optic nerve. *Eur J Ophthalmol*. 1999; 9(Suppl 1):S34–36. [PubMed: 10230604]
- Cioffi, GA., Van Buskirk, EM. Vasculature of the anterior optic nerve and peripapillary choroid. In: Ritch, R.Shields, MB., Krupin, T., editors. *The Glaucomas*. 2. Mosby; St. Louis: 1996. p. 177-197.
- Cioffi GA, Wang L, Fortune B, Cull G, Dong J, Bui B, Van Buskirk EM. Chronic ischemia induces regional axonal damage in experimental primate optic neuropathy. *Arch Ophthalmol*. 2004; 122:1517–1525. [PubMed: 15477464]

- Clark AF. The cell and molecular biology of glaucoma: biomechanical factors in glaucoma. *Invest Ophthalmol Vis Sci.* 2012; 53:2473–2475. [PubMed: 22562844]
- Cooper ML, Crish SD, Inman DM, Horner PJ, Calkins DJ. Early astrocyte redistribution in the optic nerve precedes axonopathy in the DBA/2J mouse model of glaucoma. *Exp Eye Res.* 2016; 150:22–33. [PubMed: 26646560]
- Coudrillier B, Boote C, Quigley HA, Nguyen TD. Scleral anisotropy and its effects on the mechanical response of the optic nerve head. *Biomech Model Mechanobiol.* 2013; 12:941–963. [PubMed: 23188256]
- Coudrillier B, Pijanka J, Jefferys J, Sorensen T, Quigley HA, Boote C, Nguyen TD. Collagen structure and mechanical properties of the human sclera: analysis for the effects of age. *J Biomech Eng.* 2015a; 137:041006. [PubMed: 25531905]
- Coudrillier B, Pijanka J, Jefferys J, Sorensen T, Quigley HA, Boote C, Nguyen TD. Effects of age and diabetes on scleral stiffness. *J Biomech Eng.* 2015b:137.
- Coudrillier B, Pijanka JK, Jefferys JL, Goel A, Quigley HA, Boote C, Nguyen TD. Glaucoma-related Changes in the Mechanical Properties and Collagen Micro-architecture of the Human Sclera. *PLoS One.* 2015c; 10:e0131396. [PubMed: 26161963]
- Crabb JS, Stowell C, Jang G-F, Zhang L, Willard B, Burgoyne C, Crabb JW. Quantitative Proteomic Analysis of Non-Human Primate (NHP) Peripapillary (PP) Sclera in Early Experimental Glaucoma (EEG). *IOVS.* 2014; 55 ARVO E-Abstract 5704.
- Crabb JW, Hu B, Crabb JS, Triozzi P, Saunthararajah Y, Tubbs R, Singh AD. iTRAQ Quantitative Proteomic Comparison of Metastatic and Non-Metastatic Uveal Melanoma Tumors. *PLoS One.* 2015; 10:e0135543. [PubMed: 26305875]
- Crabb JW, Yuan X, Dvorianchikova G, Ivanov D, Crabb JS, Shestopalov VI. Preliminary quantitative proteomic characterization of glaucomatous rat retinal ganglion cells. *Exp Eye Res.* 2010; 91:107–110. [PubMed: 20412794]
- Crish SD, Calkins DJ. Central visual pathways in glaucoma: evidence for distal mechanisms of neuronal self-repair. *J Neuroophthalmol.* 2015; 35(Suppl 1):S29–37. [PubMed: 26274834]
- Crish SD, Dapper JD, MacNamee SE, Balaram P, Sidorova TN, Lambert WS, Calkins DJ. Failure of axonal transport induces a spatially coincident increase in astrocyte BDNF prior to synapse loss in a central target. *Neuroscience.* 2013; 229:55–70. [PubMed: 23159315]
- Crish SD, Sappington RM, Inman DM, Horner PJ, Calkins DJ. Distal axonopathy with structural persistence in glaucomatous neurodegeneration. *Proc Natl Acad Sci U S A.* 2010; 107:5196–5201. [PubMed: 20194762]
- Cull G, Burgoyne CF, Fortune B, Wang L. Longitudinal hemodynamic changes within the optic nerve head in experimental glaucoma. *Invest Ophthalmol Vis Sci.* 2013; 54:4271–4277. [PubMed: 23737471]
- Dandona L, Hendrickson A, Quigley HA. Selective effects of experimental glaucoma on axonal transport by retinal ganglion cells to the dorsal lateral geniculate nucleus. *Invest Ophthalmol Vis Sci.* 1991; 32:1593–1599. [PubMed: 1707861]
- Danias J, Lee KC, Zamora MF, Chen B, Shen F, Filippopoulos T, Su Y, Goldblum D, Podos SM, Mittag T. Quantitative analysis of retinal ganglion cell (RGC) loss in aging DBA/2NNia glaucomatous mice: comparison with RGC loss in aging C57/BL6 mice. *Invest Ophthalmol Vis Sci.* 2003; 44:5151–5162. [PubMed: 14638711]
- Dastiridou AI, Tsironi EE, Tsilimbaris MK, Ginis H, Karyotakis N, Cholevas P, Androudi S, Pallikaris IG. Ocular rigidity, outflow facility, ocular pulse amplitude, and pulsatile ocular blood flow in open-angle glaucoma: a manometric study. *Invest Ophthalmol Vis Sci.* 2013; 54:4571–4577. [PubMed: 23761082]
- Davis CH, Kim KY, Bushong EA, Mills EA, Boassa D, Shih T, Kinebuchi M, Phan S, Zhou Y, Bihlmeyer NA, Nguyen JV, Jin Y, Ellisman MH, Marsh-Armstrong N. Transcellular degradation of axonal mitochondria. *Proc Natl Acad Sci U S A.* 2014; 111:9633–9638. [PubMed: 24979790]
- Desatnik H, Quigley HA, Glovinsky Y. Study of central retinal ganglion cell loss in experimental glaucoma in monkey eyes. *J Glaucoma.* 1996; 5:46–53. [PubMed: 8795733]
- Dougherty, RP, Kunzelmann, K-H. Computing Local Thickness of 3D Structures with ImageJ. *Microscopy & Microanalysis Meeting; Ft. Lauderdale, Florida.* 2007.

- Downs JC. Optic nerve head biomechanics in aging and disease. *Exp Eye Res.* 2015; 133:19–29. [PubMed: 25819451]
- Downs JC, Burgoyne CF, Seigfreid WP, Reynaud JF, Strouthidis NG, Sallee V. 24-hour IOP telemetry in the nonhuman primate: implant system performance and initial characterization of IOP at multiple timescales. *Invest Ophthalmol Vis Sci.* 2011; 52:7365–7375. [PubMed: 21791586]
- Downs, JC., Roberts, MD., Burgoyne, CF. Mechanical Strain and Restructuring of the Optic Nerve Head. In: Shaarawy, T.Sherwood, MB.Hitchings, RA., Crowston, JG., editors. *Glaucoma*. 1. Saunders; London: 2009.
- Downs JC, Suh JK, Thomas KA, Bellezza AJ, Hart RT, Burgoyne CF. Viscoelastic material properties of the peripapillary sclera in normal and early-glaucoma monkey eyes. *Invest Ophthalmol Vis Sci.* 2005; 46:540–546. [PubMed: 15671280]
- Downs JC, Yang H, Girkin C, Sakata L, Bellezza A, Thompson H, Burgoyne CF. Three-dimensional histomorphometry of the normal and early glaucomatous monkey optic nerve head: neural canal and subarachnoid space architecture. *Invest Ophthalmol Vis Sci.* 2007; 48:3195–3208. [PubMed: 17591889]
- Eilaghi A, Flanagan JG, Simmons CA, Ethier CR. Effects of scleral stiffness properties on optic nerve head biomechanics. *Ann Biomed Eng.* 2010; 38:1586–1592. [PubMed: 20039133]
- Faridi OS, Park SC, Kabadi R, Su D, De Moraes CG, Liebmann JM, Ritch R. Effect of focal lamina cribrosa defect on glaucomatous visual field progression. *Ophthalmology.* 2014; 121:1524–1530. [PubMed: 24697910]
- Fazio MA, Grytz R, Morris JS, Bruno L, Gardiner SK, Girkin CA, Downs JC. Age-related changes in human peripapillary scleral strain. *Biomech Model Mechanobiol.* 2014a; 13:551–563. [PubMed: 23896936]
- Fazio MA, Grytz R, Morris JS, Bruno L, Girkin CA, Downs JC. Human scleral structural stiffness increases more rapidly with age in donors of African descent compared to donors of European descent. *Invest Ophthalmol Vis Sci.* 2014b; 55:7189–7198. [PubMed: 25237162]
- Feola AJ, Myers JG, Raykin J, Mulugeta L, Nelson ES, Samuels B, Ethier CR. Finite Element Modeling of Factors Influencing Optic Nerve Head Deformation Due to Intracranial Pressure. *Invest Ophthalmol Vis Sci.* 2016; 57:1901–1911. [PubMed: 27088762]
- Filippopoulos T, Danias J, Chen B, Podos SM, Mittag TW. Topographic and morphologic analyses of retinal ganglion cell loss in old DBA/2NNia mice. *Invest Ophthalmol Vis Sci.* 2006; 47:1968–1974. [PubMed: 16639004]
- Fortune B, Cull G, Reynaud J, Wang L, Burgoyne CF. Relating Retinal Ganglion Cell Function and Retinal Nerve Fiber Layer (RNFL) Retardance to Progressive Loss of RNFL Thickness and Optic Nerve Axons in Experimental Glaucoma. *Invest Ophthalmol Vis Sci.* 2015; 56:3936–3944. [PubMed: 26087359]
- Fortune B, Hardin C, Reynaud J, Cull G, Yang H, Wang L, Burgoyne CF. Comparing Optic Nerve Head Rim Width, Rim Area, and Peripapillary Retinal Nerve Fiber Layer Thickness to Axon Count in Experimental Glaucoma. *Invest Ophthalmol Vis Sci.* 2016a; 57:OCT404–412. [PubMed: 27409499]
- Fortune B, Lusardi TA, Reynaud J, Choe TE, Cull G, Burgoyne CF, Wang L. Evidence of axonopathy during early-stage experimental glaucoma: relationship between in vivo imaging and histological findings. *IOVS.* 2014; 55 ARVO E-Abstract 2644.
- Fortune B, Reynaud J, Hardin C, Wang L, Sigal IA, Burgoyne CF. Experimental Glaucoma Causes Optic Nerve Head Neural Rim Tissue Compression: A Potentially Important Mechanism of Axon Injury. *Invest Ophthalmol Vis Sci.* 2016b; 57:4403–4411. [PubMed: 27564522]
- Furuyoshi N, Furuyoshi M, May CA, Hayreh SS, Alm A, Lutjen-Drecoll E. Vascular and glial changes in the retrolaminar optic nerve in glaucomatous monkey eyes. *Ophthalmologica.* 2000; 214:24–32. [PubMed: 10657742]
- Gaasterland D, Tanishima T, Kuwabara T. Axoplasmic flow during chronic experimental glaucoma. 1. Light and electron microscopic studies of the monkey optic nervehead during development of glaucomatous cupping. *Invest Ophthalmol Vis Sci.* 1978; 17:838–846. [PubMed: 81192]
- Garcia-Valenzuela E, Shareef S, Walsh J, Sharma SC. Programmed cell death of retinal ganglion cells during experimental glaucoma. *Exp Eye Res.* 1995; 61:33–44. [PubMed: 7556468]

- Garway-Heath DF, Poinosawmy D, Fitzke FW, Hitchings RA. Mapping the visual field to the optic disc in normal tension glaucoma eyes. *Ophthalmology*. 2000; 107:1809–1815. [PubMed: 11013178]
- Geijer C, Bill A. Effects of raised intraocular pressure on retinal, prelaminar, laminar, and retrolaminar optic nerve blood flow in monkeys. *Invest Ophthalmol Vis Sci*. 1979; 18:1030–1042. [PubMed: 90027]
- Girard MJ, Beotra MR, Chin KS, Sandhu A, Clemo M, Nikita E, Kamal DS, Papadopoulos M, Mari JM, Aung T, Strouthidis NG. In Vivo 3-Dimensional Strain Mapping of the Optic Nerve Head Following Intraocular Pressure Lowering by Trabeculectomy. *Ophthalmology*. 2016
- Girard MJ, Dahlmann-Noor A, Rayapureddi S, Bechara JA, Bertin BM, Jones H, Albon J, Khaw PT, Ethier CR. Quantitative mapping of scleral fiber orientation in normal rat eyes. *Invest Ophthalmol Vis Sci*. 2011a; 52:9684–9693. [PubMed: 22076988]
- Girard MJ, Downs JC, Bottlang M, Burgoyne CF, Suh JK. Peripapillary and posterior scleral mechanics--part II: experimental and inverse finite element characterization. *J Biomech Eng*. 2009a; 131:051012. [PubMed: 19388782]
- Girard MJ, Downs JC, Burgoyne CF, Suh JK. Peripapillary and posterior scleral mechanics--part I: development of an anisotropic hyperelastic constitutive model. *J Biomech Eng*. 2009b; 131:051011. [PubMed: 19388781]
- Girard MJ, Strouthidis NG, Desjardins A, Mari JM, Ethier CR. In vivo optic nerve head biomechanics: performance testing of a three-dimensional tracking algorithm. *J R Soc Interface*. 2013; 10:20130459. [PubMed: 23883953]
- Girard MJ, Suh JK, Bottlang M, Burgoyne CF, Downs JC. Scleral biomechanics in the aging monkey eye. *Invest Ophthalmol Vis Sci*. 2009c; 50:5226–5237. [PubMed: 19494203]
- Girard MJ, Suh JK, Bottlang M, Burgoyne CF, Downs JC. Biomechanical changes in the sclera of monkey eyes exposed to chronic IOP elevations. *Invest Ophthalmol Vis Sci*. 2011b; 52:5656–5669. [PubMed: 21519033]
- Glovinsky Y, Quigley HA, Dunkelberger GR. Retinal ganglion cell loss is size dependent in experimental glaucoma. *Invest Ophthalmol Vis Sci*. 1991; 32:484–491. [PubMed: 2001923]
- Glovinsky Y, Quigley HA, Pease ME. Foveal ganglion cell loss is size dependent in experimental glaucoma. *Invest Ophthalmol Vis Sci*. 1993; 34:395–400. [PubMed: 8440594]
- Grau V, Downs JC, Burgoyne CF. Segmentation of trabeculated structures using an anisotropic Markov random field: application to the study of the optic nerve head in glaucoma. *IEEE Trans Med Imaging*. 2006; 25:245–255. [PubMed: 16524082]
- Greenfield DS. Glaucomatous versus nonglaucomatous optic disc cupping: clinical differentiation. *Semin Ophthalmol*. 1999; 14:95–108. [PubMed: 10758217]
- Grus FH, Joachim SC, Wuenschig D, Rieck J, Pfeiffer N. Autoimmunity and glaucoma. *J Glaucoma*. 2008; 17:79–84. [PubMed: 18303391]
- Grytz R, Fazio MA, Libertiaux V, Bruno L, Gardiner S, Girkin CA, Downs JC. Age- and race-related differences in human scleral material properties. *Invest Ophthalmol Vis Sci*. 2014; 55:8163–8172. [PubMed: 25389203]
- Grytz R, Girkin CA, Libertiaux V, Downs JC. Perspectives on biomechanical growth and remodeling mechanisms in glaucoma. *Mech Res Commun*. 2012a; 42:92–106. [PubMed: 23109748]
- Grytz R, Meschke G, Jonas JB. The collagen fibril architecture in the lamina cribrosa and peripapillary sclera predicted by a computational remodeling approach. *Biomech Model Mechanobiol*. 2011; 10:371–382. [PubMed: 20628781]
- Grytz R, Sigal IA, Ruberti JW, Meschke G, Downs JC. Lamina Cribrosa Thickening in Early Glaucoma Predicted by a Microstructure Motivated Growth and Remodeling Approach. *Mech Mater*. 2012b; 44:99–109. [PubMed: 22389541]
- Hamasaki DI, Fujino T. Effect of intraocular pressure on ocular vessels. Filling with India ink. *Arch Ophthalmol*. 1967; 78:369–379. [PubMed: 4962803]
- Harwerth RS, Vilupuru AS, Rangaswamy NV, Smith EL III. The Relationship between Nerve Fiber Layer and Perimetry Measurements. *Invest Ophthalmol Vis Sci*. 2007; 48:763–773. [PubMed: 17251476]

- Harwerth RS, Wheat JL, Fredette MJ, Anderson DR. Linking structure and function in glaucoma. *Prog Retin Eye Res.* 2010; 29:249–271. [PubMed: 20226873]
- Hayreh SS. The blood supply of the optic nerve head and the evaluation of it - myth and reality. *Prog Retin Eye Res.* 2001; 20:563–593. [PubMed: 11470451]
- Hayreh SS, Jonas JB. Optic disk and retinal nerve fiber layer damage after transient central retinal artery occlusion: an experimental study in rhesus monkeys. *Am J Ophthalmol.* 2000; 129:786–795. [PubMed: 10926989]
- Hayreh SS, Pe'er J, Zimmerman MB. Morphologic changes in chronic high-pressure experimental glaucoma in rhesus monkeys. *J Glaucoma.* 1999; 8:56–71. [PubMed: 10084276]
- Hayreh SS, Revie IH, Edwards J. Vasogenic origin of visual field defects and optic nerve changes in glaucoma. *Br J Ophthalmol.* 1970; 54:461–472. [PubMed: 4988400]
- He L, Ren R, Yang H, Hardin C, Reyes L, Reynaud J, Gardiner SK, Fortune B, Demirel S, Burgoyne CF. Anatomic vs. acquired image frame discordance in spectral domain optical coherence tomography minimum rim measurements. *PLoS One.* 2014a; 9:e92225. [PubMed: 24643069]
- He L, Yang H, Gardiner SK, Williams G, Hardin C, Strouthidis NG, Fortune B, Burgoyne CF. Longitudinal detection of optic nerve head changes by spectral domain optical coherence tomography in early experimental glaucoma. *Invest Ophthalmol Vis Sci.* 2014b; 55:574–586. [PubMed: 24255047]
- He X, Liu J. A quantitative ultrasonic spectroscopy method for noninvasive determination of corneal biomechanical properties. *Invest Ophthalmol Vis Sci.* 2009; 50:5148–5154. [PubMed: 19516014]
- He X, Liu J. Correlation of corneal acoustic and elastic properties in a canine eye model. *Invest Ophthalmol Vis Sci.* 2011; 52:731–736. [PubMed: 20926820]
- Heickell AG, Bellezza AJ, Thompson HW, Burgoyne CF. Optic disc surface compliance testing using confocal scanning laser tomography in the normal monkey eye. *J Glaucoma.* 2001; 10:369–382. [PubMed: 11711833]
- Helb HM, Charbel Issa P, Fleckenstein M, Schmitz-Valckenberg S, Scholl HP, Meyer CH, Eter N, Holz FG. Clinical evaluation of simultaneous confocal scanning laser ophthalmoscopy imaging combined with high-resolution, spectral-domain optical coherence tomography. *Acta Ophthalmol.* 2010; 88:842–849. [PubMed: 19706019]
- Hernandez MR. The optic nerve head in glaucoma: role of astrocytes in tissue remodeling. *Prog Retin Eye Res.* 2000; 19:297–321. [PubMed: 10749379]
- Hernandez MR, Luo XX, Igoe F, Neufeld AH. Extracellular matrix of the human lamina cribrosa. *Am J Ophthalmol.* 1987; 104:567–576. [PubMed: 3318474]
- Hildebrand T, Rügsegger P. A new method for the model-independent assessment of thickness in three-dimensional images. *Journal of Microscopy.* 1997; 185:67–75.
- Hogan, JJ., Alvarado, JA., Weddell, JE. *Histology of the Human Eye.* WB Saunders Co; Philadelphia: 1971.
- Hood DC, Kardon RH. A framework for comparing structural and functional measures of glaucomatous damage. *Prog Retin Eye Res.* 2007; 26:688–710. [PubMed: 17889587]
- Howell GR, Libby RT, Jakobs TC, Smith RS, Phalan FC, Barter JW, Barbay JM, Marchant JK, Mahesh N, Porciatti V, Whitmore AV, Masland RH, John SW. Axons of retinal ganglion cells are insulted in the optic nerve early in DBA/2J glaucoma. *J Cell Biol.* 2007; 179:1523–1537. [PubMed: 18158332]
- Howell GR, Macalinao DG, Sousa GL, Walden M, Soto I, Kneeland SC, Barbay JM, King BL, Marchant JK, Hibbs M, Stevens B, Barres BA, Clark AF, Libby RT, John SW. Molecular clustering identifies complement and endothelin induction as early events in a mouse model of glaucoma. *J Clin Invest.* 2011; 121:1429–1444. [PubMed: 21383504]
- Howell GR, Soto I, Ryan M, Graham LC, Smith RS, John SW. Deficiency of complement component 5 ameliorates glaucoma in DBA/2J mice. *J Neuroinflammation.* 2013; 10:76. [PubMed: 23806181]
- Howell GR, Soto I, Zhu X, Ryan M, Macalinao DG, Sousa GL, Caddle LB, MacNicol KH, Barbay JM, Porciatti V, Anderson MG, Smith RS, Clark AF, Libby RT, John SW. Radiation treatment inhibits monocyte entry into the optic nerve head and prevents neuronal damage in a mouse model of glaucoma. *J Clin Invest.* 2012; 122:1246–1261. [PubMed: 22426214]

- Ing E, Ivers KM, Yang H, Gardiner SK, Reynaud J, Cull G, Wang L, Burgoyne CF. Cupping in the Monkey Optic Nerve Transection Model Consists of Prelaminar Tissue Thinning in the Absence of Posterior Laminal Deformation. *Invest Ophthalmol Vis Sci.* 2016; 57:2598–2611.
- Ivers KM, Yang H, Gardiner SK, Qin L, Reyes L, Fortune B, Burgoyne CF. In Vivo Detection of Laminal and Peripapillary Scleral Hypercompliance in Early Monkey Experimental Glaucoma. *Invest Ophthalmol Vis Sci.* 2016; 57:OCT388–403. [PubMed: 27409498]
- Jakobs TC, Libby RT, Ben Y, John SW, Masland RH. Retinal ganglion cell degeneration is topological but not cell type specific in DBA/2J mice. *J Cell Biol.* 2005; 171:313–325. [PubMed: 16247030]
- Jang G-F, Stowell C, Zhang L, Crabb JS, Willard B, Burgoyne C, Crabb JW. Quantitative Proteomic Analysis Of Non-Human Primate (NHP) Retina In Early Experimental Glaucoma (EEG). *IOVS.* 2014; 55 ARVO E-Abstract 4524.
- Jansson NM, Nevalainen J, Selig B, Zangwill LM, Sample PA, Budde WM, Jonas JB, Lagreze WA, Airaksinen PJ, Vonthein R, Levin LA, Paetzold J, Schiefer U. A mathematical description of nerve fiber bundle trajectories and their variability in the human retina. *Vision Res.* 2009; 49:2157–2163. [PubMed: 19539641]
- Janssen P, Naskar R, Moore S, Thanos S, Thiel HJ. Evidence for glaucoma-induced horizontal cell alterations in the human retina. *Ger J Ophthalmol.* 1996; 5:378–385. [PubMed: 9479522]
- Joachim SC, Reinehr S, Kuehn S, Laspas P, Gramlich OW, Kuehn M, Tischoff I, von Pein HD, Dick HB, Grus FH. Immune response against ocular tissues after immunization with optic nerve antigens in a model of autoimmune glaucoma. *Mol Vis.* 2013; 19:1804–1814. [PubMed: 23946635]
- Johansson JO. Inhibition of retrograde axoplasmic transport in rat optic nerve by increased IOP in vitro. *Invest Ophthalmol Vis Sci.* 1983; 24:1552–1558. [PubMed: 6197389]
- Johnson EC, Cepurna WO, Choi D, Choe TE, Morrison JC. Radiation pretreatment does not protect the rat optic nerve from elevated intraocular pressure-induced injury. *Invest Ophthalmol Vis Sci.* 2015; 56:412–419.
- Johnson EC, Deppmeier LM, Wentzien SK, Hsu I, Morrison JC. Chronology of optic nerve head and retinal responses to elevated intraocular pressure. *Invest Ophthalmol Vis Sci.* 2000; 41:431–442. [PubMed: 10670473]
- Johnson EC, Doser T, Cepurna WO, Dyck J, Jia L, Guo Y, Lambert W, Morrison JC. Cell proliferation and interleukin-6-type cytokine signaling are implicated by gene expression responses in early optic nerve head injury in rat glaucoma. *Invest Ophthalmol Vis Sci.* 2011; 52:504–518. [PubMed: 20847120]
- Johnson EC, Jia L, Cepurna WO, Doser TA, Morrison JC. Global Changes in Optic Nerve Head Gene Expression after Exposure to Elevated Intraocular Pressure in a Rat Glaucoma Model. *Invest Ophthalmol Vis Sci.* 2007; 48:3161–3177. [PubMed: 17591886]
- Johnson EC, Morrison JC, Farrell S, Deppmeier L, Moore CG, McGinty MR. The effect of chronically elevated intraocular pressure on the rat optic nerve head extracellular matrix. *Exp Eye Res.* 1996; 62:663–674. [PubMed: 8983948]
- Jonas JB, Grundler A. Optic disc morphology in “age-related atrophic glaucoma”. *Graefes Arch Clin Exp Ophthalmol.* 1996; 234:744–749. [PubMed: 8986446]
- Jonas JB, Hayreh SS. Localised retinal nerve fibre layer defects in chronic experimental high pressure glaucoma in rhesus monkeys. *Br J Ophthalmol.* 1999; 83:1291–1295. [PubMed: 10535860]
- Jonas JB, Hayreh SS, Yong T. Thickness of the lamina cribrosa and peripapillary sclera in Rhesus monkeys with nonglaucomatous or glaucomatous optic neuropathy. *Acta Ophthalmol.* 2011; 89:e423–427. [PubMed: 21332675]
- Jonas JB, Nguyen NX, Naumann GO. The retinal nerve fiber layer in normal eyes. *Ophthalmology.* 1989; 96:627–632. [PubMed: 2748120]
- Kalvin NH, Hamasaki DI, Gass JD. Experimental glaucoma in monkeys. I. Relationship between intraocular pressure and cupping of the optic disc and cavernous atrophy of the optic nerve. *Arch Ophthalmol.* 1966; 76:82–93. [PubMed: 4957379]
- Kendell KR, Quigley HA, Kerrigan LA, Pease ME, Quigley EN. Primary open-angle glaucoma is not associated with photoreceptor loss. *Invest Ophthalmol Vis Sci.* 1995; 36:200–205. [PubMed: 7822147]

- Ketcham RA, Ryan TM. Quantification and visualization of anisotropy in trabecular bone. *J Microsc.* 2004; 213:158–171. [PubMed: 14731299]
- Kubota T, Jonas JB, Naumann GO. Decreased choroidal thickness in eyes with secondary angle closure glaucoma. An aetiological factor for deep retinal changes in glaucoma? *Br J Ophthalmol.* 1993a; 77:430–432. [PubMed: 8343472]
- Kubota T, Jonas JB, Naumann GO. Direct clinico-histological correlation of parapapillary chorioretinal atrophy. *Br J Ophthalmol.* 1993b; 77:103–106. [PubMed: 8435408]
- Langham M. The temporal relation between intraocular pressure and loss of vision in chronic simple glaucoma. *Glaucoma.* 1980; 2:427–435.
- Lee EJ, Kim TW, Kim M, Girard MJ, Mari JM, Weinreb RN. Recent structural alteration of the peripheral lamina cribrosa near the location of disc hemorrhage in glaucoma. *Invest Ophthalmol Vis Sci.* 2014a; 55:2805–2815. [PubMed: 24677111]
- Lee KM, Kim TW, Weinreb RN, Lee EJ, Girard MJ, Mari JM. Anterior lamina cribrosa insertion in primary open-angle glaucoma patients and healthy subjects. *PLoS One.* 2014b; 9:e114935. [PubMed: 25531761]
- Lei Y, Rajabi S, Pedrigi RM, Overby DR, Read AT, Ethier CR. In vitro models for glaucoma research: effects of hydrostatic pressure. *Invest Ophthalmol Vis Sci.* 2011; 52:6329–6339. [PubMed: 21693606]
- Li P, Reif R, Zhi Z, Martin E, Shen TT, Johnstone M, Wang RK. Phase-sensitive optical coherence tomography characterization of pulse-induced trabecular meshwork displacement in ex vivo nonhuman primate eyes. *J Biomed Opt.* 2012; 17:076026. [PubMed: 22894509]
- Liang Y, Downs JC, Fortune B, Cull G, Cioffi GA, Wang L. Impact of systemic blood pressure on the relationship between intraocular pressure and blood flow in the optic nerve head of nonhuman primates. *Invest Ophthalmol Vis Sci.* 2009; 50:2154–2160. [PubMed: 19074806]
- Liu J, He X. Corneal stiffness affects IOP elevation during rapid volume change in the eye. *Invest Ophthalmol Vis Sci.* 2009; 50:2224–2229. [PubMed: 19151396]
- Liu J, Roberts CJ. Influence of corneal biomechanical properties on intraocular pressure measurement: quantitative analysis. *J Cataract Refract Surg.* 2005; 31:146–155. [PubMed: 15721707]
- Lockwood H, Reynaud J, Gardiner S, Grimm J, Libertaux V, Downs JC, Yang H, Burgoyne CF. Lamina cribrosa microarchitecture in normal monkey eyes part 1: methods and initial results. *Invest Ophthalmol Vis Sci.* 2015; 56:1618–1637. [PubMed: 25650423]
- Mackenzie PJ, Pham H, Stouthidis NG, Mansberger SL, Gardiner SK, Burgoyne CF. Peripapillary HRT Reflectance Changes in Non-Human Primate Experimental Glaucoma. *IOVS.* 2009; 50 ARVO E-Abstract 2785.
- Mari JM, Strouthidis NG, Park SC, Girard MJ. Enhancement of lamina cribrosa visibility in optical coherence tomography images using adaptive compensation. *Invest Ophthalmol Vis Sci.* 2013; 54:2238–2247. [PubMed: 23449723]
- Miller NR, Johnson MA, Nolan T, Guo Y, Bernstein AM, Bernstein SL. Sustained neuroprotection from a single intravitreal injection of PGJ(2) in a nonhuman primate model of nonarteritic anterior ischemic optic neuropathy. *Invest Ophthalmol Vis Sci.* 2014; 55:7047–7056. [PubMed: 25298416]
- Mills EA, Davis CH, Bushong EA, Boassa D, Kim KY, Ellisman MH, Marsh-Armstrong N. Astrocytes phagocytose focal dystrophies from shortening myelin segments in the optic nerve of *Xenopus laevis* at metamorphosis. *Proc Natl Acad Sci U S A.* 2015; 112:10509–10514. [PubMed: 26240339]
- Minckler DS, Bunt AH, Johanson GW. Orthograde and retrograde axoplasmic transport during acute ocular hypertension in the monkey. *Invest Ophthalmol Vis Sci.* 1977; 16:426–441. [PubMed: 67096]
- Morgan JE, Uchida H, Caprioli J. Retinal ganglion cell death in experimental glaucoma. *Br J Ophthalmol.* 2000; 84:303–310. [PubMed: 10684843]
- Morgan WH, Yu DY, Alder VA, Cringle SJ, Cooper RL, House PH, Constable IJ. The correlation between cerebrospinal fluid pressure and retrolaminar tissue pressure. *Invest Ophthalmol Vis Sci.* 1998; 39:1419–1428. [PubMed: 9660490]

- Morrison JC, Dorman-Pease ME, Dunkelberger GR, Quigley HA. Optic nerve head extracellular matrix in primary optic atrophy and experimental glaucoma. *Arch Ophthalmol*. 1990; 108:1020–1024. [PubMed: 2369339]
- Morrison JC, L'Hernault NL, Jerdan JA, Quigley HA. Ultrastructural location of extracellular matrix components in the optic nerve head. *Arch Ophthalmol*. 1989; 107:123–129. [PubMed: 2910271]
- Nguyen JV, Soto I, Kim KY, Bushong EA, Oglesby E, Valiente-Soriano FJ, Yang Z, Davis CH, Bedont JL, Son JL, Wei JO, Buchman VL, Zack DJ, Vidal-Sanz M, Ellisman MH, Marsh-Armstrong N. Myelination transition zone astrocytes are constitutively phagocytic and have synuclein dependent reactivity in glaucoma. *Proc Natl Acad Sci U S A*. 2011; 108:1176–1181. [PubMed: 21199938]
- Nguyen TD, Ethier CR. Biomechanical assessment in models of glaucomatous optic neuropathy. *Exp Eye Res*. 2015
- Nork TM, Ver Hoeve JN, Poulsen GL, Nickells RW, Davis MD, Weber AJ, Vaegan, Sarks SH, Lemley HL, Millecchia LL. Swelling and loss of photoreceptors in chronic human and experimental glaucomas. *Arch Ophthalmol*. 2000; 118:235–245. [PubMed: 10676789]
- Norman RE, Flanagan JG, Sigal IA, Rausch SM, Tertinegg I, Ethier CR. Finite element modeling of the human sclera: influence on optic nerve head biomechanics and connections with glaucoma. *Exp Eye Res*. 2011; 93:4–12. [PubMed: 20883693]
- Oda M. A method for evaluating the effect of crack geometry on the mechanical behavior of cracked rock masses. *Mechanics of Materials*. 1983; 2:163–171.
- Odgaard A, Kabel J, van Rietbergen B, Dalstra M, Huiskes R. Fabric and elastic principal directions of cancellous bone are closely related. *J Biomech*. 1997; 30:487–495. [PubMed: 9109560]
- Orgul S, Cioffi GA, Bacon DR, Van Buskirk EM. An endothelin-1-induced model of chronic optic nerve ischemia in rhesus monkeys. *J Glaucoma*. 1996a; 5:135–138. [PubMed: 8795746]
- Orgul S, Cioffi GA, Wilson DJ, Bacon DR, Van Buskirk EM. An endothelin-1 induced model of optic nerve ischemia in the rabbit. *Invest Ophthalmol Vis Sci*. 1996b; 37:1860–1869. [PubMed: 8759355]
- Overby DR, Stamer WD, Johnson M. The changing paradigm of outflow resistance generation: towards synergistic models of the JCT and inner wall endothelium. *Exp Eye Res*. 2009; 88:656–670. [PubMed: 19103197]
- Panda S, Jonas JB. Decreased photoreceptor count in human eyes with secondary angle-closure glaucoma. *Invest Ophthalmol Vis Sci*. 1992; 33:2532–2536. [PubMed: 1634350]
- Patel NB, Lim M, Gajjar A, Evans KB, Harwerth RS. Age-associated changes in the retinal nerve fiber layer and optic nerve head. *Invest Ophthalmol Vis Sci*. 2014a; 55:5134–5143. [PubMed: 25052998]
- Patel NB, Sullivan-Mee M, Harwerth RS. The relationship between retinal nerve fiber layer thickness and optic nerve head neuroretinal rim tissue in glaucoma. *Invest Ophthalmol Vis Sci*. 2014b; 55:6802–6816. [PubMed: 25249610]
- Patel NB, Wheat JL, Rodriguez A, Tran V, Harwerth RS. Agreement between retinal nerve fiber layer measures from Spectralis and Cirrus spectral domain OCT. *Optom Vis Sci*. 2012; 89:E652–666. [PubMed: 22105330]
- Pazos M, Yang H, Gardiner SK, Cepurna WO, Johnson EC, Morrison JC, Burgoyne CF. Expansions of the neurovascular scleral canal and contained optic nerve occur early in the hypertonic saline rat experimental glaucoma model. *Exp Eye Res*. 2016; 145:173–186. [PubMed: 26500195]
- Pijanka JK, Coudrillier B, Ziegler K, Sorensen T, Meek KM, Nguyen TD, Quigley HA, Boote C. Quantitative mapping of collagen fiber orientation in non-glaucoma and glaucoma posterior human sclerae. *Invest Ophthalmol Vis Sci*. 2012; 53:5258–5270. [PubMed: 22786908]
- Povazay B, Hofer B, Hermann B, Unterhuber A, Morgan JE, Glittenberg C, Binder S, Drexler W. Minimum distance mapping using three-dimensional optical coherence tomography for glaucoma diagnosis. *J Biomed Opt*. 2007; 12:041204. [PubMed: 17867793]
- Quigley HA. Ganglion cell death in glaucoma: pathology recapitulates ontogeny. *Aust N Z J Ophthalmol*. 1995a; 23:85–91. [PubMed: 7546696]

- Quigley, HA. Overview and introduction to session on connective tissue of the optic nerve in glaucoma. In: Drance, SM., Anderson, DR., editors. *Optic Nerve in Glaucoma*. Vol. Chapter 2. Kugler Publications; Amsterdam/New York: 1995b. p. 15-36.
- Quigley HA, Addicks EM. Chronic experimental glaucoma in primates. II. Effect of extended intraocular pressure elevation on optic nerve head and axonal transport. *Invest Ophthalmol Vis Sci*. 1980; 19:137–152. [PubMed: 6153173]
- Quigley HA, Addicks EM. Regional differences in the structure of the lamina cribrosa and their relation to glaucomatous optic nerve damage. *Arch Ophthalmol*. 1981; 99:137–143. [PubMed: 7458737]
- Quigley HA, Addicks EM, Green WR, Maumenee AE. Optic nerve damage in human glaucoma. II. The site of injury and susceptibility to damage. *Arch Ophthalmol*. 1981; 99:635–649. [PubMed: 6164357]
- Quigley HA, Anderson DR. The histologic basis of optic disk pallor in experimental optic atrophy. *Am J Ophthalmol*. 1977; 83:709–717. [PubMed: 405870]
- Quigley HA, Brown A, Dorman-Pease ME. Alterations in elastin of the optic nerve head in human and experimental glaucoma. *Br J Ophthalmol*. 1991; 75:552–557. [PubMed: 1911659]
- Quigley HA, Brown AE, Morrison JD, Drance SM. The size and shape of the optic disc in normal human eyes. *Arch Ophthalmol*. 1990; 108:51–57. [PubMed: 2297333]
- Quigley HA, Green WR. The histology of human glaucoma cupping and optic nerve damage: clinicopathologic correlation in 21 eyes. *Ophthalmology*. 1979; 86:1803–1830. [PubMed: 553256]
- Quigley HA, Guy J, Anderson DR. Blockade of rapid axonal transport. Effect of intraocular pressure elevation in primate optic nerve. *Arch Ophthalmol*. 1979; 97:525–531. [PubMed: 84662]
- Quigley HA, Hohman RM, Addicks EM, Green WR. Blood vessels of the glaucomatous optic disc in experimental primate and human eyes. *Invest Ophthalmol Vis Sci*. 1984; 25:918–931. [PubMed: 6746235]
- Quigley HA, Hohman RM, Sanchez R, Addicks EM. Optic nerve head blood flow in chronic experimental glaucoma. *Arch Ophthalmol*. 1985; 103:956–962. [PubMed: 4015488]
- Quigley HA, McKinnon SJ, Zack DJ, Pease ME, Kerrigan-Baumrind LA, Kerrigan DF, Mitchell RS. Retrograde axonal transport of BDNF in retinal ganglion cells is blocked by acute IOP elevation in rats. *Invest Ophthalmol Vis Sci*. 2000; 41:3460–3466. [PubMed: 11006239]
- Quigley HA, Nickells RW, Kerrigan LA, Pease ME, Thibault DJ, Zack DJ. Retinal ganglion cell death in experimental glaucoma and after axotomy occurs by apoptosis. *Invest Ophthalmol Vis Sci*. 1995; 36:774–786. [PubMed: 7706025]
- Quigley HA, Pitha IF, Welsbie DS, Nguyen C, Steinhart MR, Nguyen TD, Pease ME, Oglesby EN, Berlinicke CA, Mitchell KL, Kim J, Jefferys JJ, Kimball EC. Losartan Treatment Protects Retinal Ganglion Cells and Alters Scleral Remodeling in Experimental Glaucoma. *PLoS One*. 2015; 10:e0141137. [PubMed: 26505191]
- Radius RL, Anderson DR. Breakdown of the normal optic nerve head blood-brain barrier following acute elevation of intraocular pressure in experimental animals. *Invest Ophthalmol Vis Sci*. 1980; 19:244–255. [PubMed: 6153639]
- Radius RL, Gonzales M. Anatomy of the lamina cribrosa in human eyes. *Arch Ophthalmol*. 1981; 99:2159–2162. [PubMed: 7030283]
- Reis AS, O'Leary N, Yang H, Sharpe GP, Nicolela MT, Burgoyne CF, Chauhan BC. Influence of clinically invisible, but optical coherence tomography detected, optic disc margin anatomy on neuroretinal rim evaluation. *Invest Ophthalmol Vis Sci*. 2012a; 53:1852–1860. [PubMed: 22410561]
- Reis AS, Sharpe GP, Yang H, Nicolela MT, Burgoyne CF, Chauhan BC. Optic disc margin anatomy in patients with glaucoma and normal controls with spectral domain optical coherence tomography. *Ophthalmology*. 2012b; 119:738–747. [PubMed: 22222150]
- Ren R, Yang H, Gardiner SK, Fortune B, Hardin C, Demirel S, Burgoyne CF. Anterior lamina cribrosa surface depth, age, and visual field sensitivity in the Portland Progression Project. *Invest Ophthalmol Vis Sci*. 2014; 55:1531–1539. [PubMed: 24474264]

- Reynaud J, Cull G, Wang L, Fortune B, Gardiner S, Burgoyne CF, Cioffi GA. Automated quantification of optic nerve axons in primate glaucomatous and normal eyes--method and comparison to semi-automated manual quantification. *Invest Ophthalmol Vis Sci*. 2012; 53:2951–2959. [PubMed: 22467571]
- Reynaud J, Lockwood H, Gardiner SK, Williams G, Yang H, Burgoyne CF. Lamina Cribrosa Microarchitecture in Monkey Early Experimental Glaucoma: Global Change. *Invest Ophthalmol Vis Sci*. 2016; 57:3451–3469. [PubMed: 27362781]
- Roberts MD, Grau V, Grimm J, Reynaud J, Bellezza AJ, Burgoyne CF, Downs JC. Remodeling of the connective tissue microarchitecture of the lamina cribrosa in early experimental glaucoma. *Invest Ophthalmol Vis Sci*. 2009; 50:681–690. [PubMed: 18806292]
- Roberts MD, Liang Y, Sigal IA, Grimm J, Reynaud J, Bellezza A, Burgoyne CF, Downs JC. Correlation between local stress and strain and lamina cribrosa connective tissue volume fraction in normal monkey eyes. *Invest Ophthalmol Vis Sci*. 2010a; 51:295–307. [PubMed: 19696175]
- Roberts MD, Sigal IA, Liang Y, Burgoyne CF, Downs JC. Changes in the biomechanical response of the optic nerve head in early experimental glaucoma. *Invest Ophthalmol Vis Sci*. 2010b; 51:5675–5684. [PubMed: 20538991]
- Saito T, Toriwaki JI. New algorithms for euclidean distance transformation of an n-dimensional digitized picture with applications. *Pattern Recognition*. 1994; 27:1551–1565.
- Schiefer U, Flad M, Stumpp F, Malsam A, Paetzold J, Vonthein R, Denk PO, Sample PA. Increased detection rate of glaucomatous visual field damage with locally condensed grids: a comparison between fundus-oriented perimetry and conventional visual field examination. *Arch Ophthalmol*. 2003; 121:458–465. [PubMed: 12695242]
- Schlamp CL, Li Y, Dietz JA, Janssen KT, Nickells RW. Progressive ganglion cell loss and optic nerve degeneration in DBA/2J mice is variable and asymmetric. *BMC Neurosci*. 2006; 7:66. [PubMed: 17018142]
- See JL, Nicoleta MT, Chauhan BC. Rates of neuroretinal rim and peripapillary atrophy area change: a comparative study of glaucoma patients and normal controls. *Ophthalmology*. 2009; 116:840–847. [PubMed: 19410941]
- Sigal IA, Bilonick RA, Kagemann L, Wollstein G, Ishikawa H, Schuman JS, Grimm JL. The optic nerve head as a robust biomechanical system. *Invest Ophthalmol Vis Sci*. 2012; 53:2658–2667. [PubMed: 22427598]
- Sigal IA, Ethier CR. Biomechanics of the optic nerve head. *Exp Eye Res*. 2009; 88:799–807. [PubMed: 19217902]
- Sigal IA, Flanagan JG, Ethier CR. Factors influencing optic nerve head biomechanics. *Invest Ophthalmol Vis Sci*. 2005a; 46:4189–4199. [PubMed: 16249498]
- Sigal IA, Flanagan JG, Tertinegg I, Ethier CR. Finite element modeling of optic nerve head biomechanics. *Invest Ophthalmol Vis Sci*. 2004; 45:4378–4387. [PubMed: 15557446]
- Sigal IA, Flanagan JG, Tertinegg I, Ethier CR. Reconstruction of human optic nerve heads for finite element modeling. *Technol Health Care*. 2005b; 13:313–329. [PubMed: 16055979]
- Sigal IA, Flanagan JG, Tertinegg I, Ethier CR. Modeling individual-specific human optic nerve head biomechanics. Part I: IOP-induced deformations and influence of geometry. *Biomech Model Mechanobiol*. 2009a; 8:85–98. [PubMed: 18309526]
- Sigal IA, Flanagan JG, Tertinegg I, Ethier CR. Modeling individual-specific human optic nerve head biomechanics. Part II: influence of material properties. *Biomech Model Mechanobiol*. 2009b; 8:99–109. [PubMed: 18301933]
- Sigal IA, Grimm JL. A few good responses: which mechanical effects of IOP on the ONH to study? *Invest Ophthalmol Vis Sci*. 2012; 53:4270–4278. [PubMed: 22570343]
- Sigal IA, Grimm JL, Schuman JS, Kagemann L, Ishikawa H, Wollstein G. A method to estimate biomechanics and mechanical properties of optic nerve head tissues from parameters measurable using optical coherence tomography. *IEEE Trans Med Imaging*. 2014; 33:1381–1389. [PubMed: 24691117]
- Sigal IA, Yang H, Roberts MD, Burgoyne CF, Downs JC. IOP-induced lamina cribrosa displacement and scleral canal expansion: an analysis of factor interactions using parameterized eye-specific models. *Invest Ophthalmol Vis Sci*. 2011; 52:1896–1907. [PubMed: 20881292]

- Soto I, Pease ME, Son JL, Shi X, Quigley HA, Marsh-Armstrong N. Retinal ganglion cell loss in a rat ocular hypertension model is sectorial and involves early optic nerve axon loss. *Invest Ophthalmol Vis Sci.* 2011; 52:434–441. [PubMed: 20811062]
- Spoerl E, Boehm AG, Pillunat LE. The influence of various substances on the biomechanical behavior of lamina cribrosa and peripapillary sclera. *Invest Ophthalmol Vis Sci.* 2005; 46:1286–1290. [PubMed: 15790892]
- Stamer WD, Braakman ST, Zhou EH, Ethier CR, Fredberg JJ, Overby DR, Johnson M. Biomechanics of Schlemm's canal endothelium and intraocular pressure reduction. *Prog Retin Eye Res.* 2014
- Stewart PS, Jensen OE, Foss AJ. A theoretical model to allow prediction of the CSF pressure from observations of the retinal venous pulse. *Invest Ophthalmol Vis Sci.* 2014; 55:6319–6323. [PubMed: 25190664]
- Stowell C, Jang G, Reynaud J, Gardiner S, Zhang L, Crabb JS, Willard B, Crabb JW, Burgoyne CF. Myelin-Related Proteins Are Decreased In The Immediate Retrolaminar Optic Nerve (ON) In Non-Human Primates (NHP) In Early Experimental Glaucoma (EEG). *IOVS.* 2014; 55 ARVO E-Abstract 5034.
- Stowell C, Reynaud J, Gardiner SK, Williams I, Crabb J, Marsh-Armstrong N, Burgoyne CF. Quantitative Immunohistochemistry Method for Comparing Regionally Specific Signal Density within Control, Experimentally Altered and Diseased Tissues. *Invest Ophthalmol Vis Sci.* 2016
- Strouthidis NG, Fortune B, Yang H, Sigal IA, Burgoyne CF. Longitudinal change detected by spectral domain optical coherence tomography in the optic nerve head and peripapillary retina in experimental glaucoma. *Invest Ophthalmol Vis Sci.* 2011; 52:1206–1219. [PubMed: 21217108]
- Strouthidis NG, Girard MJ. Altering the way the optic nerve head responds to intraocular pressure—a potential approach to glaucoma therapy. *Curr Opin Pharmacol.* 2013; 13:83–89. [PubMed: 22999652]
- Strouthidis NG, Grimm J, Williams GA, Cull GA, Wilson DJ, Burgoyne CF. A comparison of optic nerve head morphology viewed by spectral domain optical coherence tomography and by serial histology. *Invest Ophthalmol Vis Sci.* 2010; 51:1464–1474. [PubMed: 19875649]
- Strouthidis NG, Yang H, Fortune B, Downs JC, Burgoyne CF. Detection of optic nerve head neural canal opening within histomorphometric and spectral domain optical coherence tomography data sets. *Invest Ophthalmol Vis Sci.* 2009a; 50:214–223. [PubMed: 18689697]
- Strouthidis NG, Yang H, Reynaud JF, Grimm JL, Gardiner SK, Fortune B, Burgoyne CF. Comparison of clinical and spectral domain optical coherence tomography optic disc margin anatomy. *Invest Ophthalmol Vis Sci.* 2009b; 50:4709–4718. [PubMed: 19443718]
- Sugiyama K, Cioffi GA, Bacon DR, Van Buskirk EM. Optic nerve and peripapillary choroidal microvasculature in the primate. *J Glaucoma.* 1994; 3(Suppl 1):S45–54. [PubMed: 19920587]
- Tatham AJ, Miki A, Weinreb RN, Zangwill LM, Medeiros FA. Defects of the Lamina Cribrosa in Eyes with Localized Retinal Nerve Fiber Layer Loss. *Ophthalmology.* 2013
- Terai N, Spoerl E, Haustein M, Hornykewycz K, Haentzschel J, Pillunat LE. Diabetes mellitus affects biomechanical properties of the optic nerve head in the rat. *Ophthalmic Res.* 2012; 47:189–194. [PubMed: 22156545]
- Tezel G, Wax MB. The immune system and glaucoma. *Curr Opin Ophthalmol.* 2004; 15:80–84. [PubMed: 15021215]
- Tezel G, Yang X, Luo C, Cai J, Powell DW. An astrocyte-specific proteomic approach to inflammatory responses in experimental rat glaucoma. *Invest Ophthalmol Vis Sci.* 2012; 53:4220–4233. [PubMed: 22570341]
- Thomasy SM, Wood JA, Kass PH, Murphy CJ, Russell P. Substratum stiffness and latrunculin B regulate matrix gene and protein expression in human trabecular meshwork cells. *Invest Ophthalmol Vis Sci.* 2012; 53:952–958. [PubMed: 22247475]
- Thornton IL, Dupps WJ, Roy AS, Krueger RR. Biomechanical effects of intraocular pressure elevation on optic nerve/lamina cribrosa before and after peripapillary scleral collagen cross-linking. *Invest Ophthalmol Vis Sci.* 2009; 50:1227–1233. [PubMed: 18952911]
- Trobe JD, Glaser JS, Cassady J, Herschler J, Anderson DR. Nonglaucomatous excavation of the optic disc. *Arch Ophthalmol.* 1980a; 98:1046–1050. [PubMed: 7387507]

- Trobe JD, Glaser JS, Cassady JC. Optic atrophy. Differential diagnosis by fundus observation alone. *Arch Ophthalmol*. 1980b; 98:1040–1045. [PubMed: 7387506]
- Turner CH. On Wolff's law of trabecular architecture. *J Biomech*. 1992; 25:1–9. [PubMed: 1733977]
- Turpin A, Sampson GP, McKendrick AM. Combining ganglion cell topology and data of patients with glaucoma to determine a structure-function map. *Invest Ophthalmol Vis Sci*. 2009; 50:3249–3256. [PubMed: 19324839]
- Wang L, Burgoyne CF, Cull G, Thompson S, Fortune B. Static blood flow autoregulation in the optic nerve head in normal and experimental glaucoma. *Invest Ophthalmol Vis Sci*. 2014a; 55:873–880. [PubMed: 24436190]
- Wang L, Cull G, Burgoyne CF, Thompson S, Fortune B. Longitudinal alterations in the dynamic autoregulation of optic nerve head blood flow revealed in experimental glaucoma. *Invest Ophthalmol Vis Sci*. 2014b; 55:3509–3516. [PubMed: 24812551]
- Wang L, Cull GA, Fortune B. Optic nerve head blood flow response to reduced ocular perfusion pressure by alteration of either the blood pressure or intraocular pressure. *Curr Eye Res*. 2015; 40:359–367. [PubMed: 24911311]
- Wang L, Cull GA, Piper C, Burgoyne CF, Fortune B. Anterior and posterior optic nerve head blood flow in nonhuman primate experimental glaucoma model measured by laser speckle imaging technique and microsphere method. *Invest Ophthalmol Vis Sci*. 2012; 53:8303–8309. [PubMed: 23169886]
- Wang X, Rumpel H, Lim WE, Baskaran M, Perera SA, Nongpiur ME, Aung T, Milea D, Girard MJ. Finite Element Analysis Predicts Large Optic Nerve Head Strains During Horizontal Eye Movements. *Invest Ophthalmol Vis Sci*. 2016; 57:2452–2462. [PubMed: 27149695]
- Wax MB, Tezel G, Yang J, Peng G, Patil RV, Agarwal N, Sappington RM, Calkins DJ. Induced autoimmunity to heat shock proteins elicits glaucomatous loss of retinal ganglion cell neurons via activated T-cell-derived fas-ligand. *J Neurosci*. 2008; 28:12085–12096. [PubMed: 19005073]
- Weber AJ, Kaufman PL, Hubbard WC. Morphology of single ganglion cells in the glaucomatous primate retina. *Invest Ophthalmol Vis Sci*. 1998; 39:2304–2320. [PubMed: 9804139]
- West JB, Fu Z, Deerinck TJ, Mackey MR, Obayashi JT, Ellisman MH. Structure-function studies of blood and air capillaries in chicken lung using 3D electron microscopy. *Respir Physiol Neurobiol*. 2010; 170:202–209. [PubMed: 20038456]
- Wilhelmsson U, Bushong EA, Price DL, Smarr BL, Phung V, Terada M, Ellisman MH, Pekny M. Redefining the concept of reactive astrocytes as cells that remain within their unique domains upon reaction to injury. *Proc Natl Acad Sci U S A*. 2006; 103:17513–17518. [PubMed: 17090684]
- Wyganski T, Desatnik H, Quigley HA, Glovinsky Y. Comparison of ganglion cell loss and cone loss in experimental glaucoma. *Am J Ophthalmol*. 1995; 120:184–189. [PubMed: 7639302]
- Yang D, Fu J, Hou R, Liu K, Jonas JB, Wang H, Chen W, Li Z, Sang J, Zhang Z, Liu S, Cao Y, Xie X, Ren R, Lu Q, Weinreb RN, Wang N. Optic neuropathy induced by experimentally reduced cerebrospinal fluid pressure in monkeys. *Invest Ophthalmol Vis Sci*. 2014a; 55:3067–3073. [PubMed: 24736050]
- Yang H, Downs JC, Bellezza A, Thompson H, Burgoyne CF. 3-D histomorphometry of the normal and early glaucomatous monkey optic nerve head: prelaminar neural tissues and cupping. *Invest Ophthalmol Vis Sci*. 2007a; 48:5068–5084. [PubMed: 17962459]
- Yang H, Downs JC, Burgoyne CF. Physiologic intereye differences in monkey optic nerve head architecture and their relation to changes in early experimental glaucoma. *Invest Ophthalmol Vis Sci*. 2009a; 50:224–234. [PubMed: 18775866]
- Yang H, Downs JC, Girkin C, Sakata L, Bellezza A, Thompson H, Burgoyne CF. 3-D histomorphometry of the normal and early glaucomatous monkey optic nerve head: lamina cribrosa and peripapillary scleral position and thickness. *Invest Ophthalmol Vis Sci*. 2007b; 48:4597–4607. [PubMed: 17898283]
- Yang H, Downs JC, Sigal IA, Roberts MD, Thompson H, Burgoyne CF. Deformation of the normal monkey optic nerve head connective tissue after acute IOP elevation within 3-D histomorphometric reconstructions. *Invest Ophthalmol Vis Sci*. 2009b; 50:5785–5799. [PubMed: 19628739]

- Yang H, He L, Gardiner SK, Reynaud J, Williams G, Hardin C, Strouthidis NG, Downs JC, Fortune B, Burgoyne CF. Age-related differences in longitudinal structural change by spectral-domain optical coherence tomography in early experimental glaucoma. *Invest Ophthalmol Vis Sci*. 2014b; 55:6409–6420. [PubMed: 25190652]
- Yang H, Luo H, Gardiner SK, Hardin C, Sharpe G, Caprioli J, Demirel S, Girkin CA, Liebmann JM, Mardin CY, Quigley HA, Scheuerle A, Fortune B, Chauhan BC, Burgoyne CF. Factors Influencing OCT Peripapillary Choroidal Thickness (ppCT) in a Normal Population: A Multi-Center Study. *IOVS*. 2017
- Yang H, Ren R, Lockwood H, Williams G, Libertiaux V, Downs C, Gardiner SK, Burgoyne CF. The Connective Tissue Components of Optic Nerve Head Cupping in Monkey Experimental Glaucoma Part 1: Global Change. *Invest Ophthalmol Vis Sci*. 2015a; 56:7661–7678. [PubMed: 26641545]
- Yang H, Reynaud J, Gardiner SK, He L, Fortune B, Burgoyne CF. Eye-specific Onset and Spatial Pattern of Longitudinal Change Detected by Spectral Domain Optical Coherence Tomography (SDOCT) Sectoral Analysis in Non-human Primate (NHP) Early Experimental Glaucoma (EG). *IOVS*. 2015b; 56 ARVO E-Abstract.
- Yang, H., Reynaud, J., Lockwood, H., Williams, G., Hardin, C., Reyes, L., Gardiner, SK., Burgoyne, CF. 3D Histomorphometric Reconstruction and Quantification of the Optic Nerve Head Connective Tissues. In: Jacobs, T., editor. *Methods in Glaucoma Research*. Springer; New York, NY: Accepted for publication Nov 2016 Forthcoming 2017
- Yang H, Thompson H, Roberts MD, Sigal IA, Downs JC, Burgoyne CF. Deformation of the early glaucomatous monkey optic nerve head connective tissue after acute IOP elevation in 3-D histomorphometric reconstructions. *Invest Ophthalmol Vis Sci*. 2011a; 52:345–363. [PubMed: 20702834]
- Yang H, Williams G, Downs JC, Sigal IA, Roberts MD, Thompson H, Burgoyne CF. Posterior (outward) migration of the lamina cribrosa and early cupping in monkey experimental glaucoma. *Invest Ophthalmol Vis Sci*. 2011b; 52:7109–7121. [PubMed: 21715355]
- You JY, Park SC, Su D, Teng CC, Liebmann JM, Ritch R. Focal lamina cribrosa defects associated with glaucomatous rim thinning and acquired pits. *JAMA Ophthalmol*. 2013; 131:314–320. [PubMed: 23370812]
- Yuan X, Gu X, Crabb JS, Yue X, Shadrach K, Hollyfield JG, Crabb JW. Quantitative proteomics: comparison of the macular Bruch membrane/choroid complex from age-related macular degeneration and normal eyes. *Mol Cell Proteomics*. 2010; 9:1031–1046. [PubMed: 20177130]
- Yucel YH, Zhang Q, Gupta N, Kaufman PL, Weinreb RN. Loss of neurons in magnocellular and parvocellular layers of the lateral geniculate nucleus in glaucoma. *Arch Ophthalmol*. 2000; 118:378–384. [PubMed: 10721961]
- Yucel YH, Zhang Q, Weinreb RN, Kaufman PL, Gupta N. Atrophy of relay neurons in magno- and parvocellular layers in the lateral geniculate nucleus in experimental glaucoma. *Invest Ophthalmol Vis Sci*. 2001; 42:3216–3222. [PubMed: 11726625]
- Yucel YH, Zhang Q, Weinreb RN, Kaufman PL, Gupta N. Effects of retinal ganglion cell loss on magno-, parvo-, koniocellular pathways in the lateral geniculate nucleus and visual cortex in glaucoma. *Prog Retin Eye Res*. 2003; 22:465–481. [PubMed: 12742392]
- Zhang L, Albon J, Jones H, Gouget CL, Ethier CR, Goh JC, Girard MJ. Collagen microstructural factors influencing optic nerve head biomechanics. *Invest Ophthalmol Vis Sci*. 2015; 56:2031–2042. [PubMed: 25736791]
- Zhang L, Stowell C, Jang G, Crabb JS, Willard B, Burgoyne CF, Crabb JW. Quantitative Proteomic Analysis Of Non-Human Primate (NHP) Optic Nerve (ON) In Early Experimental Glaucoma (EEG). *IOVS*. 2014; 55 ARVO E-Abstract 4519.
- Zhou EH, Krishnan R, Stamer WD, Perkumas KM, Rajendran K, Nabhan JF, Lu Q, Fredberg JJ, Johnson M. Mechanical responsiveness of the endothelial cell of Schlemm’s canal: scope, variability and its potential role in controlling aqueous humour outflow. *J R Soc Interface*. 2012; 9:1144–1155. [PubMed: 22171066]

Highlights

- ONH connective tissue deformation and remodeling define the optic neuropathy of glaucoma
- The lamina cribrosa thickens, migrates into the pia, then thins in monkey experimental glaucoma
- Lamina cribrosa deformation can be detected early in monkey experimental glaucoma by OCT
- There are no experimental models of normal tension glaucoma in the monkey eye
- Retinal ganglion cell axon loss, alone, does not create “glaucomatous” cupping

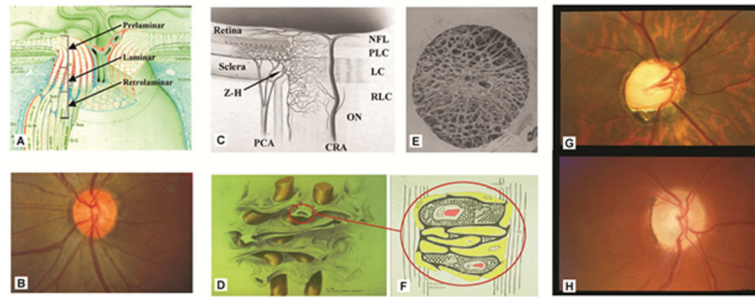


Figure 1. Optic Nerve Head (ONH) Homeostasis is Influenced by Intraocular Pressure (IOP)-related Stress and Strain at all levels of IOP

See Section 2.2 for details. **(A)** Prelaminar, lamellar and retrolaminar ONH regions. **(B)** The clinically visible surface of the normal ONH (referred to as the optic disc). Central retinal vessels enter the eye and RGC axons appear pink due to their capillaries. **(C)** The posterior ciliary arteries (PCA) are the principal blood supply to the ONH (see Figures 4 and 5). **(D)** The lamina cribrosa (LC) is (schematically depicted with axon bundles in **(D)**), isolated by trypsin digest in a scanning electron micrograph in **(E)** and drawn with stippled extracellular matrix (ECM), central capillary (red) and surrounding astrocytes (yellow with basement membranes in black) **(F)**. The clinical manifestation of IOP-induced damage to the ONH is most commonly “deep cupping” **(G)** but in some eyes cupping can be shallower accompanied by pallor **(H)**. Z-H = circle of Zinn-Haller; PCA= posterior ciliary arteries; NFL = nerve fiber layer; PLC = prelaminar region; LC = lamina cribrosa; RLC = retrolaminar region; ON = optic nerve; CRA = central retinal artery.

A - Reproduced with permission from Arch Ophthalmol.1969;82:800–814. Copyright © (1969) American Medical Association. All rights reserved (Anderson and Hoyt, 1969). B, G, H – Reprinted from J Glaucoma. 2008;17(4):318–28, with permission from Wolters Kluwer Health, Inc. (Burgoyne and Downs, 2008). C - Reprinted courtesy of J. Cioffi and M. Van Buskirk, from The Glaucomas. St. Louis, Mosby: Basic Sciences; 1996:177–197 (Cioffi and Van Buskirk, 1996). D –Reprinted courtesy of Harry Quigley, from Optic Nerve in Glaucoma. Amsterdam: Kugler Publications; 1995:15–36(Quigley, 1995b). E - Reproduced with permission from Arch Ophthalmol. 1990;108:51–57. Copyright © (1990) American Medical Association. All rights reserved (Morrison et al., 1989). F - Reproduced with permission from Arch Ophthalmol. 1989;107:123–129. Copyright © (1989) American Medical Association. All rights reserved (Quigley et al., 1990).

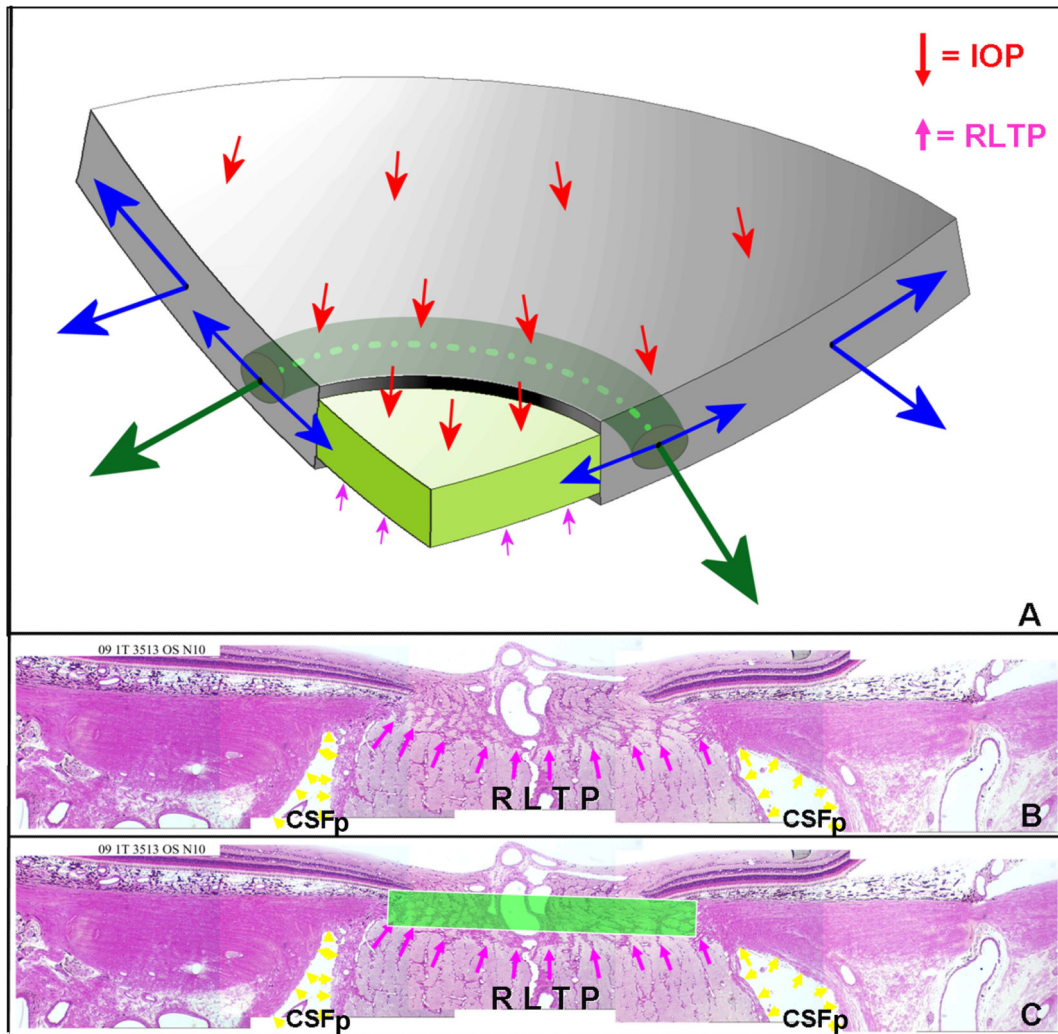


Figure 2. Principle distribution of forces, pressures and the translaminar pressure gradient within the optic nerve head (ONH)

See section 2.3 for details. (A) Cut-away diagram of intraocular pressure (IOP)-induced mechanical stress in an idealized spherical scleral shell. **Red arrows:** IOP/orbital pressure difference; **Green arrows:** peripapillary scleral hoop stress generated by IOP; **Blue arrows:** peripapillary tensile stress that is generated by the lamina and delivered to the lamellar beams. (B) **Pink arrows:** retrolaminar tissue pressure (RLTP) which is higher than cerebrospinal fluid pressure (**Yellow arrows**). (C) The difference between IOP and the retrolaminar tissue pressure is the translaminar pressure difference which generates both a net posterior (outward) force on the surface of the lamina (the red arrows over the lamina) and a hydrostatic pressure gradient (the translaminar pressure gradient - schematically shown in green) within the neural and connective tissues of the pre-laminar and lamellar regions.

Panel A - Adapted from Downs JC, Roberts MD, Burgoyne CF. Mechanical Strain and Restructuring of the Optic Nerve Head. In: Shaarawy T, Sherwood MB, Hitchings RA, Crowston JG, editors. Glaucoma. 1 ed. London: Saunders, Copyright 2009, with permission from Elsevier (Downs et al., 2009).

Panels B & C - Reprinted from Exp Eye Res, 93(2), Burgoyne CF, A biomechanical paradigm for axonal insult within the optic nerve head in aging and glaucoma, 120–32, Copyright 2011, with permission from Elsevier (Burgoyne, 2011).

Author Manuscript

Author Manuscript

Author Manuscript

Author Manuscript

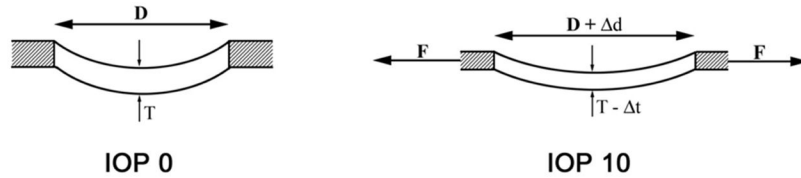


Figure 3. Schematic Representation of the Lamina/Scleral Dynamic as Experimentally Observed in Non-pressurized (Intraocular Pressure (IOP) 0, left) and pressurized (IOP 10, right) Monkey Control Eyes (Bellezza et al., 2003a)

See Section 2.4 for details. **(Left):** Thickness (T) of the lamina cribrosa and diameter (D) of the scleral canal opening in an unpressurized (IOP 0) eye. **(Right):** Pressure within the globe generates an expansion of the scleral shell which, in turn, generates (and is resisted by) tensile forces within the sclera. These forces (F) act on the scleral canal wall, causing the scleral canal opening to expand (Δd), which in turn stretches the lamina within the canal. Thus, the lamina is taut (more anteriorly positioned) and thinned (Δt) in the IOP 10 eye, compared with the IOP 0 eye.

Reproduced from Br J Ophthalmol, Bellezza AJ, Rintalan CJ, Thompson HW, Downs JC, Hart RT, Burgoyne CF. Anterior scleral canal geometry in pressurised (IOP 10) and non-pressurised (IOP 0) normal monkey eyes, 87(10):1284–90, copyright 2003 with permission from BMJ Publishing Group Ltd (Bellezza et al., 2003a).

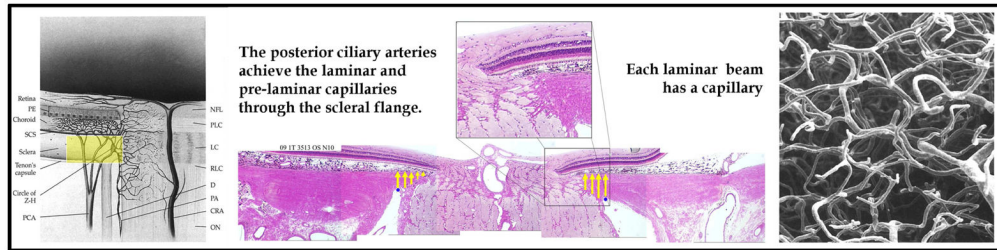


Figure 4. The Volume Flow of Blood within the Posterior Ciliary Arteries should be affected by Intraocular Pressure (IOP)-related Stress and Strain within the Peripapillary Sclera (pp-sclera) and Scleral Flange

See Section 2.5 for details. The posterior ciliary arteries pass through the pp-sclera (yellow, left and center panel) immediately adjacent to the scleral portion of the neural canal. We refer to this portion of the sclera as the scleral flange (Yang et al., 2007b) (yellow arrows, middle figure). Each laminar beam contains a capillary (Panel F, Figure 1) which are here shown in a vascular casting of a monkey eye (Cioffi and Van Buskirk, 1996).

Left and right panels reprinted courtesy of J. Cioffi and M. Van Buskirk, from *The Glaucomas*. St. Louis, Mosby: Basic Sciences; 1996:177–197 (Cioffi and Van Buskirk, 1996).

Middle Panel reprinted from *Exp Eye Res*, 93(2), Burgoyne CF, A biomechanical paradigm for axonal insult within the optic nerve head in aging and glaucoma, 120–32, Copyright 2011, with permission from Elsevier (Burgoyne, 2011).

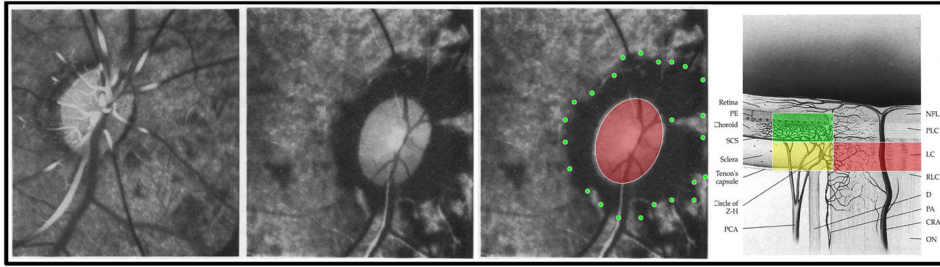


Figure 5. Hayreh (Hayreh et al., 1970) demonstrated Sensitivity of the Peripapillary Choroidal Circulation (green) to Acute Intraocular Pressure (IOP) elevation in the Monkey Optic Nerve Head (ONH)

See Section 2.5 for details. Fluorescence fundus angiogram of the right eye of a cynomolgus monkey after experimental central retinal artery occlusion at normal (far left) and 70 mm Hg IOP (middle left and right). The non-perfused region of the peripapillary choroid is schematically highlighted in green (middle right). We and others have hypothesized that IOP-related stress and strain within the scleral flange (Figure 4, above) may contribute to this phenomenon and that similar effects may occur within the lamellar capillary beds (red) (middle and far right).

The far right panel is reprinted courtesy of J. Cioffi and M. Van Buskirk, from *The Glaucomas*. St. Louis, Mosby: Basic Sciences; 1996:177–197 (Cioffi and Van Buskirk, 1996).

The far left, middle left and middle right panels are reproduced from *Br J Ophthalmol*, Hayreh SS, Revie IH, Edwards J., 54(7), 461–72, copyright 1970 with permission from BMJ Publishing Group Ltd (Hayreh et al., 1970).

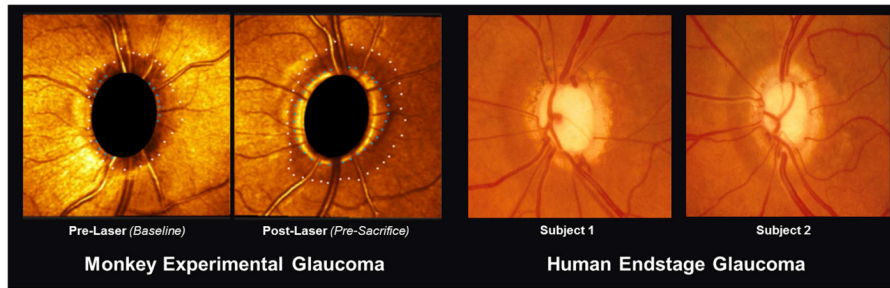


Figure 6. Peripapillary Hypo and Hyper-reflectance Changes are Manifestations of Outward Bowing of the Peripapillary Sclera (pp-sclera) and Decreased Peripapillary Choroidal Blood Flow, respectively

See Section 2.5 for details. **(Left Panels)** A hypo-reflective shadow (white dots) is present in a (future) EG eye prior to laser (Baseline, far left panel) and is seen to enlarge through the course of experimental glaucoma (“Post-laser” middle left panel). At Baseline there is no hyper-reflectance (i.e. RPE atrophy, blue dots) but this is clearly present in the Pre-sacrifice image to the right. **(Right Panels)** Two end-stage glaucoma eyes from two different human subjects demonstrate a similar peripapillary shadow and classic peripapillary atrophy (white and blue dots not deployed).

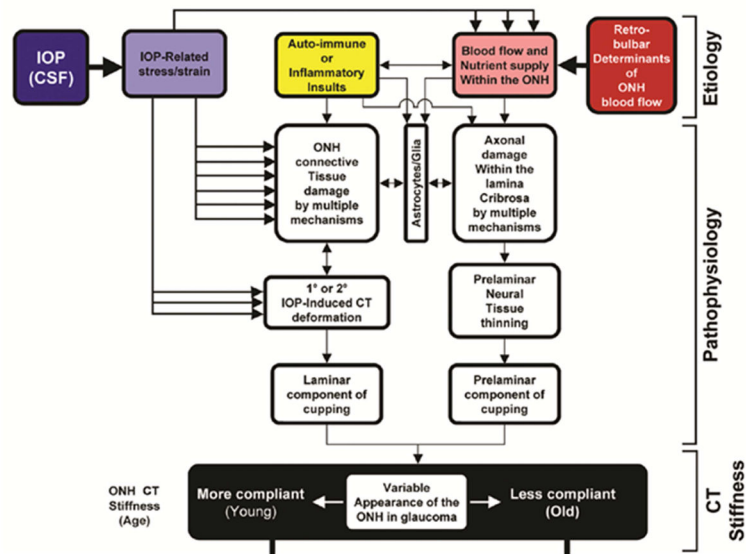


Figure 7. Damage to the Neural and Connective Tissues of the Optic Nerve Head (ONH) is multifactorial in Glaucoma

See section 2.6 for details. Intraocular pressure (IOP)-related stress and strain (dark purple, upper left) influence the ONH connective tissues, the volume flow of blood within the posterior ciliary arteries (light pink, upper central) (primarily) and the delivery of nutrients (secondarily), through chronic alterations in connective tissue stiffness and diffusion properties (explained in Figures 1 and 2). Non-IOP related effects such as auto-immune or inflammatory insults (yellow) and retrobulbar determinants of ocular blood flow (red) can primarily damage the ONH connective tissues and/or axons, leaving them vulnerable to secondary damage by IOP-related mechanisms at normal or elevated levels of IOP. All of these events play out on ONH connective tissues which are more or less compliant prior to insult, based on their geometry and material properties. In general young ONH connective tissues have been shown to be more compliant than old connective tissues for both the lamina and sclera (see Sections 3.6 and 3.9 for details).

Reprinted from Burgoyne CF, Downs JC. Premise and prediction-how optic nerve head biomechanics underlies the susceptibility and clinical behavior of the aged optic nerve head. *J Glaucoma*. 2008;17(4):318–28, with permission from Wolters Kluwer Health, Inc. (Burgoyne and Downs, 2008).

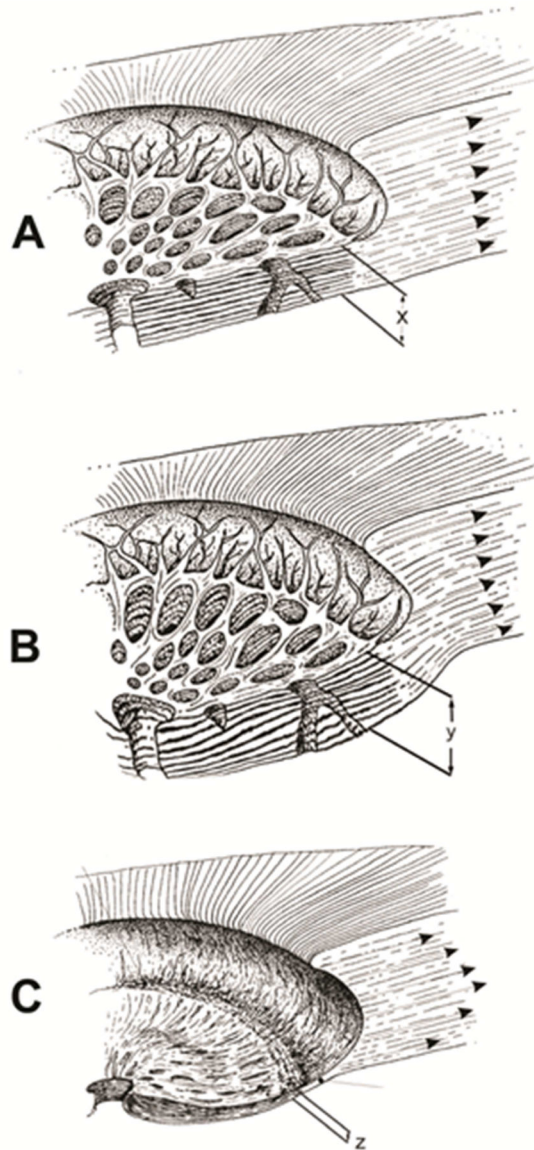


Figure 8. Connective Tissue Deformation, Remodeling and Mechanical failure underlie the “Laminar” Component of Glaucomatous Cupping

See Sections 2.7 and 3.0 for details. (A) Schematic of normal lamellar thickness (x) within the scleral canal with scleral tensile forces acting on the scleral canal wall (arrows). (B) Early IOP-related damage in the monkey eye (Figure 7) includes posterior bowing of the lamina and pp-sclera accompanied by scleral canal expansion (mostly within the posterior (outer) scleral portion), thickening (not thinning) of the lamina (y) and outward migration of the lamellar insertion from the sclera into the pia mater (not depicted here but seen in Figure 12). (C) Progression to end-stage damage is thus along and within the canal wall and includes profound scleral canal wall expansion (clinical excavation) and posterior deformation and thinning of the lamina (z).

Reprinted from Yang, H., et al. (2015). “The Connective Tissue Components of Optic Nerve Head Cupping in Monkey Experimental Glaucoma Part 1: Global Change.” Invest

Ophthalmol Vis Sci 56(13): 7661–7678, with permission from Association for Research in Vision and Ophthalmology (Yang et al., 2015a).

Author Manuscript

Author Manuscript

Author Manuscript

Author Manuscript

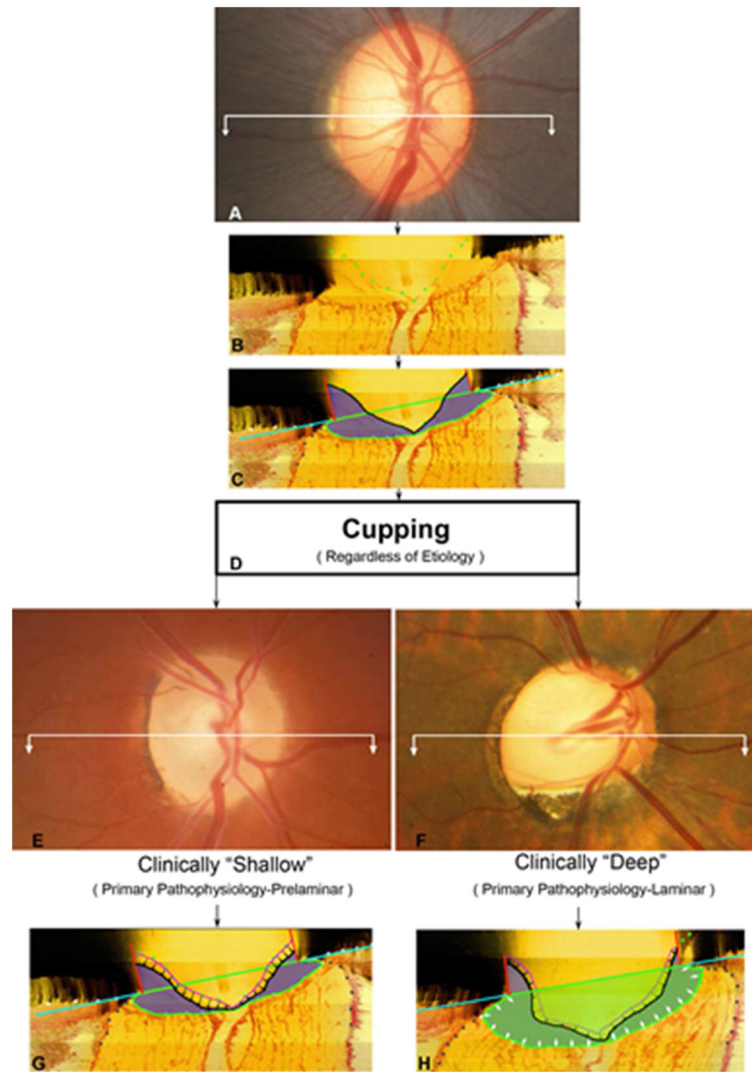


Figure 9. All Clinical Optic Nerve Head (ONH) Cupping, Regardless of Etiology, manifests “Prelaminar” and “Laminar” Components

See Section 2.8 for details. (A) normal ONH. To understand the two pathophysiologic components of clinical cupping, start with (B) a representative digital central horizontal section image from a post-mortem 3D reconstruction of this same eye (white section line in (A)) - vitreous top, orbital optic nerve bottom, lamina cribrosa between the sclera and internal limiting membrane (ILM) delineated with green dots. (C) The same section is delineated into principle surfaces and volumes (Black – ILM; purple - prelaminar neural and vascular tissue; cyan blue line – Bruch’s Membrane Opening (BMO)-zero reference plane cut in section; green outline – Post-BMO Total Prelaminar area or a measure of the space below BMO and the anterior laminar surface). (D) Regardless of the etiology, clinical cupping can be “shallow” (E) or “deep” (F) (these clinical photos are representative and are not of the eye in (A)).

Reproduced from Yang H, Downs JC, Bellezza A, et al. 3-D histomorphometry of the normal and early glaucomatous monkey optic nerve head: prelaminar neural tissues and

cupping. Invest Ophthalmol Vis Sci 2007;48:5068–5084, with permission from the Association for Research in Vision and Ophthalmology (Yang et al., 2007a).

Author Manuscript

Author Manuscript

Author Manuscript

Author Manuscript

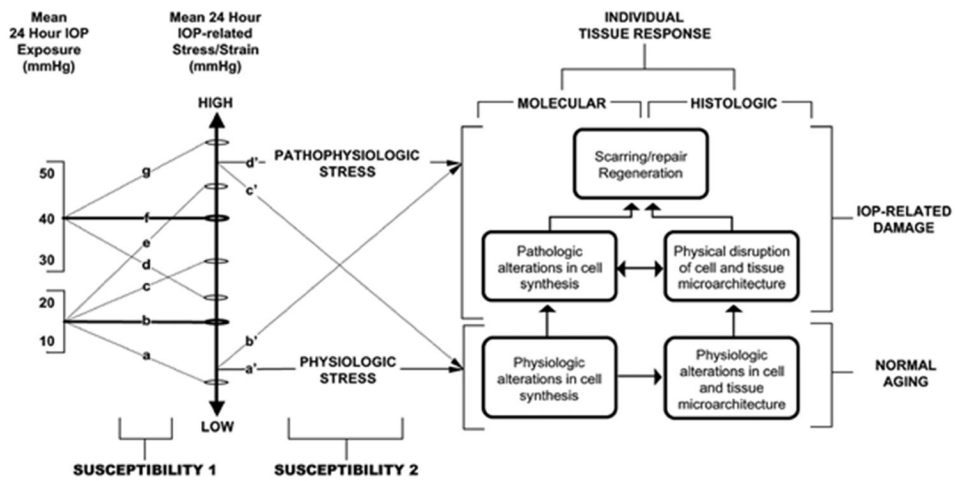


Figure 10. Over the Course of a Lifetime, an Eye Demonstrates the “Neuropathy of Aging” or the Neuropathy of Glaucoma Based on ONH Susceptibility

See Section 2.9 for details. (**Susceptibility 1, Left**) For a given ONH, IOP (at all levels of IOP) generates low or high levels of stress depending upon the 3D architecture (geometry) of the ONH connective tissues (size and shape of the canal, thickness of the lamina and sclera). (**Susceptibility 2, middle**). Some ONHs will have relatively low stress at high IOP (d). Others will have high stress at low IOP (e). Whether a given level of IOP-related stress is physiologic or pathophysiologic depends upon the ONH’s microenvironment. (**Right Bottom**). Strong connective tissues, a robust blood supply and stable astrocytes and glia increase the chance of “normal” ONH Aging (right – bottom). (**Right Top**). However, even at low levels of engineering stress/strain (b’), some eyes will achieve enough “age-related” axon loss to achieve the diagnosis of glaucoma in the setting of a statistically “normal” levels of IOP.

Reprinted from *Prog Retin Eye Res*, 24, Burgoyne CF, Downs JC, Bellezza AJ, Suh JK, Hart RT., The optic nerve head as a biomechanical structure: a new paradigm for understanding the role of IOP-related stress and strain in the pathophysiology of glaucomatous optic nerve head damage, 39–73, Copyright 2005, with permission from Elsevier (Burgoyne et al., 2005).

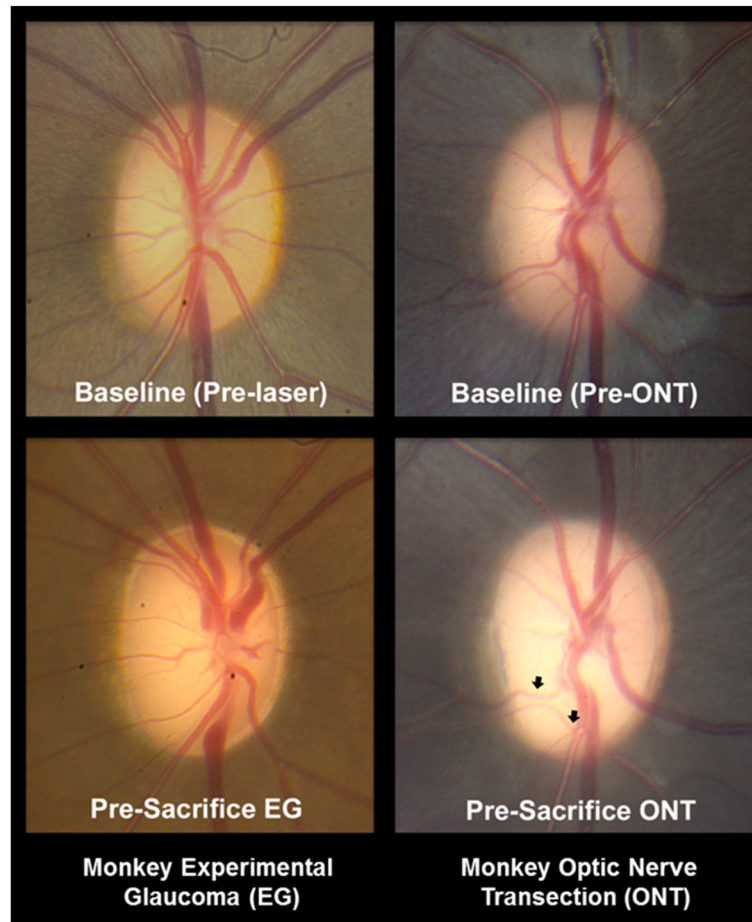


Figure 11. The Clinical Appearance of Cupping in a Representative Monkey Experimental Glaucoma (EG, left) and Optic Nerve Transection (ONT) Eye (Ing et al., 2016)

See Section 2.10 for details. **(Left)** Representative EG eye at baseline (prior to laser – above) and near the time of euthanasia (below) from an old (16.1 years of age) animal with 58% axon loss at the time of death. **(Right)** Representative young adult ONT eye (7.8 years old) with 51% axon loss. Both eyes are shown in right eye orientation. In the EG eye, (left panels), note the posterior deformation and early excavation of the central retinal artery and veins as they leave the lamina and cross the clinical disc margin. Early “nasalization” of the vessels and “bayoneting” of the inferior vein as well as diffuse loss of the retinal nerve fiber layer (RNFL) striations are also apparent. In the ONT eye, (right panels) diffuse pallor and RNFL loss (–41% by OCT) is apparent, as is OCT-detected prelaminar and rim tissue thinning. While the presence of clinical cupping is not obvious it is suggested by a slight change in the trajectory of the inferior temporal vessels (black arrows). No eye-specific change in anterior lamina cribrosa surface depth was detected by OCT in this eye (see Figures 38–39).

Reproduced from Ing, E., Ivers, K.M., Yang, H., Gardiner, S.K., Reynaud, J., Cull, G., Wang, L., Burgoyne, C.F., 2016. Cupping in the Monkey Optic Nerve Transection Model Consists of Prelaminar Tissue Thinning in the Absence of Posterior Lamina Deformation.

Invest Ophthalmol Vis Sci 57, 2598–2611, under the CC BY-NC-ND 4.0 license (Ing et al., 2016).

Author Manuscript

Author Manuscript

Author Manuscript

Author Manuscript

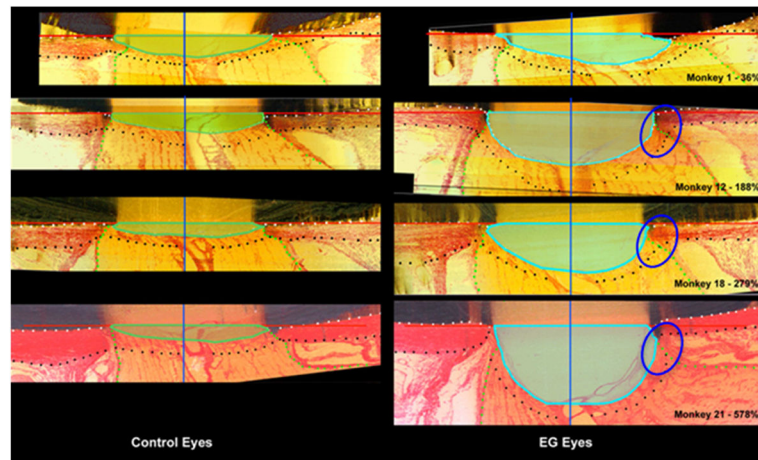


Figure 12. Connective Tissue Deformation, Remodeling and Mechanical failure in the Monkey Experimental Glaucoma (EG) model (Burgoyne, 2015a; Yang et al., 2015a)

See sections 2.10 and 3.1 for details. Five morphologic phenomena underlie ONH cupping in monkey experimental glaucoma (EG): 1) laminar deformation; 2) scleral canal expansion; 3) laminar insertion migration; 4) laminar thickness change; and 5) posterior bowing of the pp-sclera. The following landmarks are delineated within representative superior temporal (ST) to inferior nasal (IN) digital sections from the Control (**left**) and EG (**right**) eye of 4 representative unilateral EG animals (Monkeys 1, 12, 18 and 21, respectively, from the above study): anterior scleral/laminar surface (white dots), posterior scleral/laminar surface (black dots), neural boundary (green dots), BMO reference plane (red line) and BMO centroid (vertical blue line). For each animal, our parameter *Post-BMO Total Prelaminar Volume* is outlined in both the Control (light green, left) and EG (light blue) eye for qualitative comparison. EG eye *Post-BMO Total Prelaminar Volume* expansion is due to the combination of posterior lamellar deformation, scleral canal expansion and outward migration of the anterior lamellar insertion. Because it captures three of the five deformation/remodeling phenomena, we use it as a surrogate measure of overall ONH lamellar/scleral canal deformation within a given EG eye. *Post-BMO Total Prelaminar Volume* expansion is present within Monkey 1 and progresses through more advanced stages of connective tissue deformation and remodeling (Monkeys 12, 18 and 21). The phenomena that underlie *Post-BMO Total Prelaminar Volume* expansion are accompanied by lamellar thickening in the EG eyes with the least *Post-BMO Total Prelaminar Volume* change (Monkeys 1 and 12), thickening that is progressively diminished in magnitude in eyes with moderate *Post-BMO Total Prelaminar Volume* change (Monkey 18) and lamellar thinning in the eyes with the largest *Post-BMO Total Prelaminar Volume* change (Monkey 21). Outward migration of the lamellar insertions from the sclera into the pia is apparent in Monkeys 12, 18 and 21 (blue ovals). See Figures 16 – 19 for greater details.

Reprinted from Burgoyne C. The morphological difference between glaucoma and other optic neuropathies. *J Neuroophthalmol.* 2015;35 Suppl 1:S8–S21, with permission from Wolters Kluwer Health, Inc. (Burgoyne, 2015a).

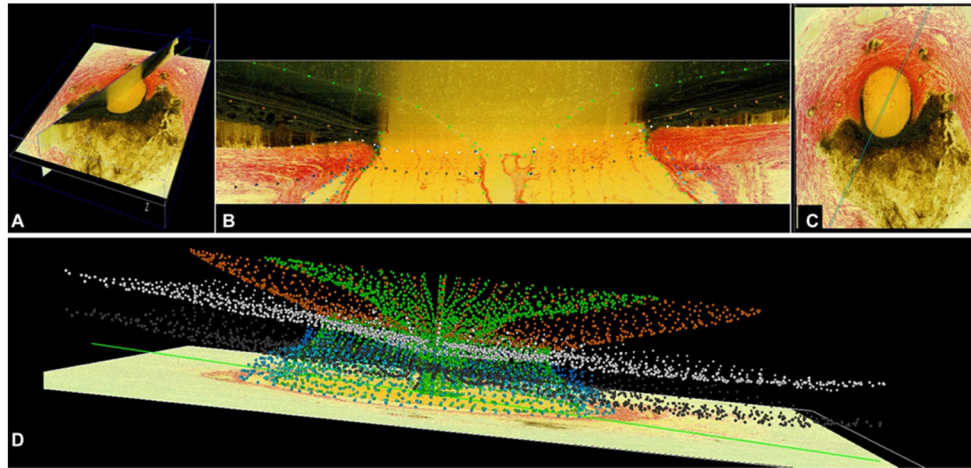


Figure 13. 3D Delineation within the 3D Histomorphometric Reconstruction (HMRN) of a single Optic Nerve Head (ONH)

See Section 3.2 for details. **(A)** A total of 40 serial digital radial sagittal slices, each 7 voxels thick, are served to the delineator at 4.5° intervals. **(B)** A representative digital sagittal slice, showing all 13 landmarks which are 3D delineated. Delineation is performed using linked, simultaneous, colocalization of the sagittal slice (shown) and the transverse section image through a given delineated point **(C)**. **(D)** Representative 3D point cloud showing all delineated points for a normal monkey ONH relative to the posterior serial section image (vitreous *top*, orbital optic nerve *bottom*). See Figure 14 for landmark and parameter descriptions.

Reproduced from Yang, H., Williams, G., Downs, J.C., Sigal, I.A., Roberts, M.D., Thompson, H., Burgoyne, C.F., 2011. Posterior (outward) migration of the lamina cribrosa and early cupping in monkey experimental glaucoma. *Invest Ophthalmol Vis Sci* 52, 7109–7121, with permission from the Association for Research in Vision and Ophthalmology (Yang et al., 2011b).

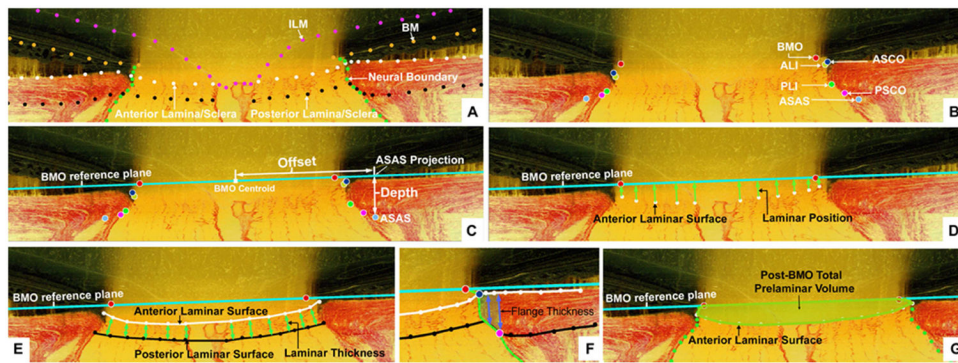


Figure 14. 3D Histomorphometric Reconstruction (HMRN) Optic Nerve Head (ONH) Connective Tissue Parameter Definitions

See Section 3.2 for details. **(A)** A representative digital sagittal slice showing the internal limiting membrane (ILM, pink dots), Bruch's membrane (BM, orange dots), anterior lamina/sclera (white dots), posterior lamina/sclera (black dots) and neural boundary (green dots). **(B)** A representative digital sagittal slice showing neural canal architectures. The neural canal includes neural canal opening (BMO, the opening in the Bruch's Membrane/Retinal Pigment Epithelial complex, *red*), the anterior scleral canal opening (ASCO, *dark blue*), the anterior lamina insertion (ALI, *dark yellow*, partly hidden behind the ASCO in dark blue), the posterior lamina insertion (PLI, *green*), the posterior scleral canal opening (PSCO, *pink*). The anterior-most aspect of the subarachnoid space (ASAS, *light blue*) was also delineated. **(C)** Definitions of the offset and depth using ASAS as an example. Right ASAS point was projected to BMO zero reference plane (cyan line), the distance between BMO centroid to the projection of ASAS is defined as **offset**. The distance between the ASAS to the projection is defined as **depth** of ASAS. The offset and depth of all other neural canal architectures were defined in the same way. **(D)** **Laminar position** (*green arrow*) is defined as the shortest distance from the delineated anterior lamina surface point (white dot) to the BMO zero reference plane. **(E)** **Lamina cribrosa thickness** at each delineated anterior surface point is determined by fitting a continuous surface (*white line*) to all anterior surface points and then measuring the distance along a normal vector of the anterior surface (*green arrow*) from each anterior delineated point to the posterior surface. **(F)** The thickness of the scleral flange at each delineated anterior surface point (*white dots*) is defined as the distance between the neural canal boundary points (*green line*), along a vector parallel to the PSCO normal vector (*blue arrow*). **(G)** **Post-BMO Total Prelaminar Volume** (*light green*): a measure of the lamina or connective tissue component of cupping) is the volume beneath the BMO zero reference plane in cyan, above the lamina cribrosa and within the neural canal wall.

Reproduced from Yang H, Downs JC, Sigal IA, Roberts MD, Thompson H, Burgoyne CF. Deformation of the normal monkey optic nerve head connective tissue after acute IOP elevation within 3-D histomorphometric reconstructions. *Invest Ophthalmol Vis Sci*. 2009;50(12):5785–99, with permission from the Association for Research in Vision and Ophthalmology (Yang et al., 2009b).

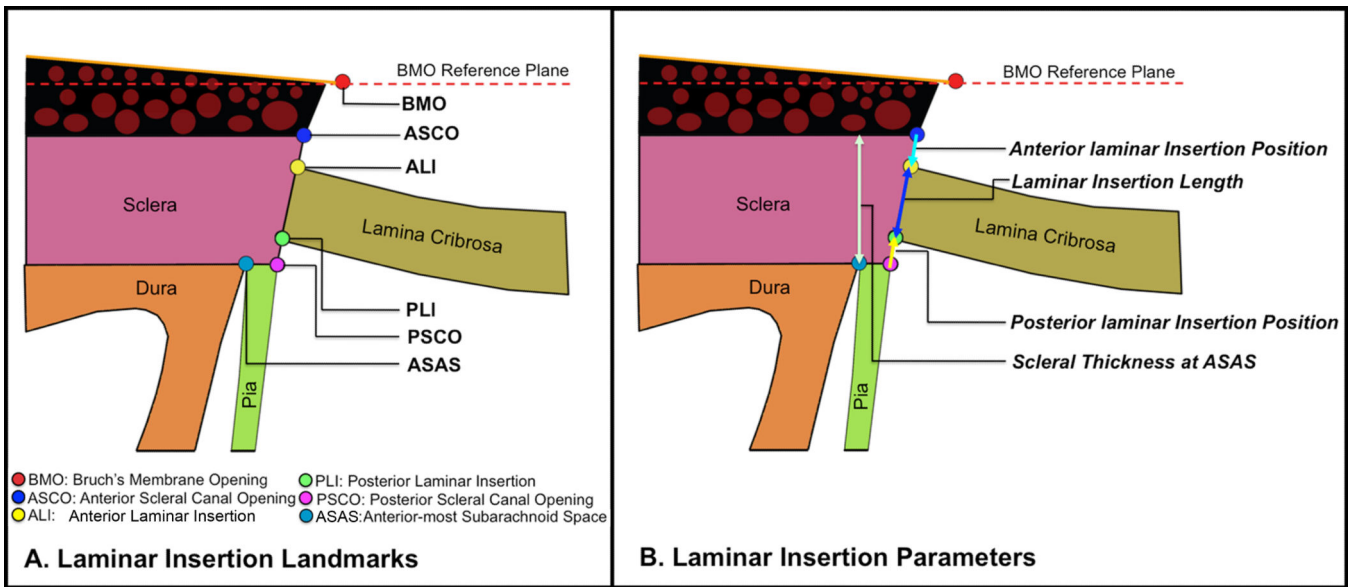


Figure 15. 3D Histomorphometric Reconstruction (HMRN) Laminar Insertion Parameters
 See Section 3.2 for details. The principal Laminar Insertion Landmarks (depicted within a digital histomorphometric section image in Figure 14) are schematically depicted in (A). Four Laminar Insertion Parameters are depicted in (B) and are italicized throughout the manuscript to distinguish them from the landmarks they measure. *Anterior Laminal Insertion Position* to ASCO (*ALIP*) is the position of the anterior lamina insertion (ALI) relative to the anterior scleral canal opening (ASCO). *ALIP* is positive (not shown) when the anterior lamina inserts into the Border Tissues of Elshnig and negative (cyan arrow) when the anterior lamina inserts into the sclera. *Posterior Laminal Insertion Position* to PSCO (*PLIP*) is the position of the posterior lamina insertion (PLI) relative to the PSCO. *PLIP* is positive (red arrow) when the posterior lamina inserts to the sclera and negative when the posterior lamina inserts to the pia. *Scleral Thickness at ASAS* - light green arrow) is the minimum scleral thickness measured from the anterior most aspect of the subarachnoid space.

Reproduced from Yang, H., Williams, G., Downs, J.C., Sigal, I.A., Roberts, M.D., Thompson, H., Burgoyne, C.F., 2011. Posterior (outward) migration of the lamina cribrosa and early cupping in monkey experimental glaucoma. *Invest Ophthalmol Vis Sci* 52, 7109–7121, with permission from the Association for Research in Vision and Ophthalmology (Yang et al., 2011b).

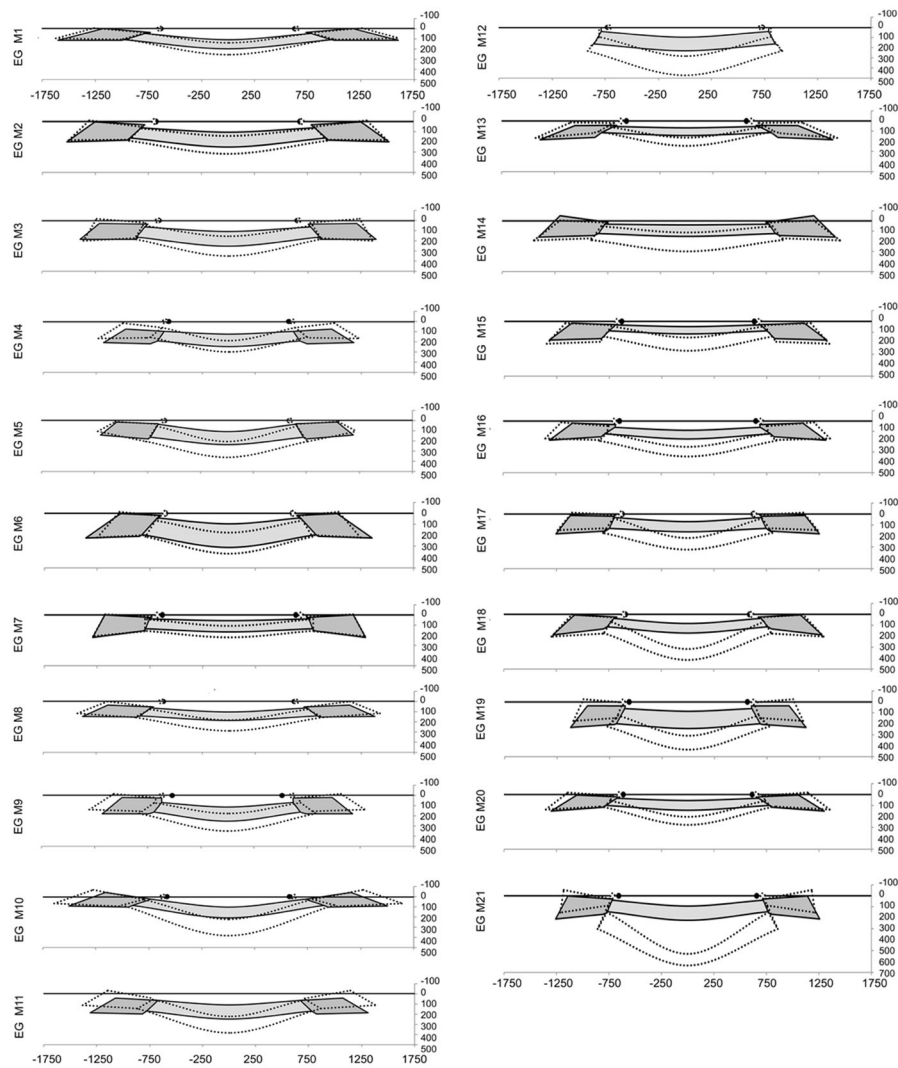


Figure 16. 3D Histomorphometric Reconstruction (HMRN) Macroarchitectural Experimental Glaucoma (EG) Study - Schematic Depiction of the Global Data for the Control (solid grey colors) and EG (dotted lines) Optic Nerve Head (ONH) of each animal

See Section 3.2 for details. Animals are ordered (1–21) by increasing overall ONH connective tissue deformation as characterized by the parameter *Post-BMO Total Prelaminar Volume* (see Figure 17). The lamina is consistently thickened in the eyes with the least deformation and consistently thinned in the most profoundly deformed eyes. These changes are accompanied by anterior and posterior laminal insertion migration, scleral canal expansion, and pp-scleral bowing (Figures 17 – 19). The relationship between overall deformation and these related phenomena can be better appreciated within the data plots of these figures.

Reproduced from Yang, H., Ren, R., Lockwood, H., Williams, G., Libertiaux, V., Downs, C., Gardiner, S.K., Burgoyne, C.F., 2015. The Connective Tissue Components of Optic Nerve Head Cupping in Monkey Experimental Glaucoma Part 1: Global Change. *Invest Ophthalmol Vis Sci* 56, 7661–7678, with permission from the Association for Research in Vision and Ophthalmology (Yang et al., 2015a).

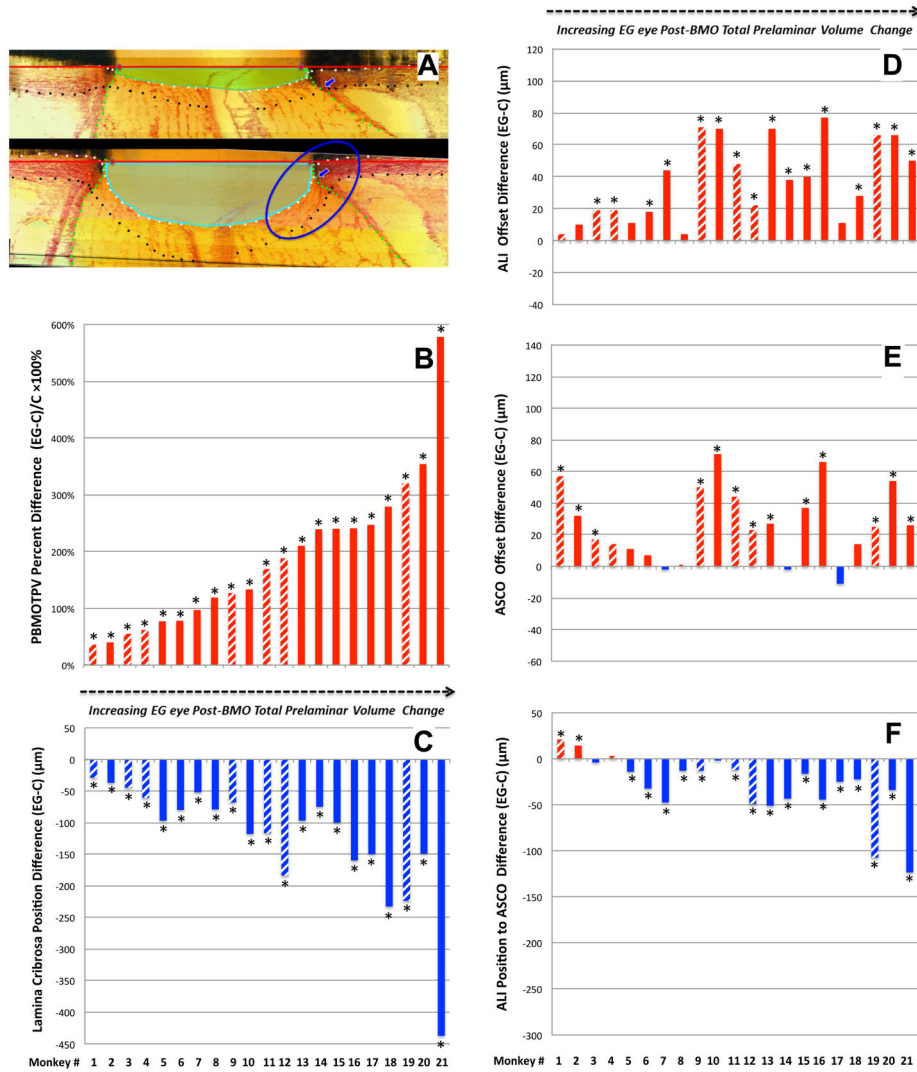


Figure 17. Experimental Glaucoma (EG) Eye *Post-BMO Total Prelaminar Volume* expansion (A and B) captures three components of ONH connective tissue change in Monkey EG in a single parameter: 1) Posterior Laminar Deformation (C); 2) Scleral Canal Expansion (D and E); and 3) Posterior (Outward) Migration of the anterior laminar insertion (F)

See Section 3.2 for details. Animal order (1–21) for this study was determined by the magnitude of the EG versus Control eye *Post-BMO Total Prelaminar Volume %* difference. *Post-BMO Total Prelaminar Volume %* difference progressively increases through all 21 EG eyes. While posterior laminar deformation (C) and anterior laminar insertion migration, (F) also appear progressive through this range of *Post-BMO Total Prelaminar Volume* expansion, scleral canal expansion at the level of the anterior scleral canal opening (D) and anterior laminar insertion (E) appear to achieve their maximum values by the magnitude of *Post-BMO Total Prelaminar Volume* Expansion present in Animal 12 (approximately 127%, (B)). (*) indicates the EG versus Control eye difference exceeds the *PIDmax* or *PIPDmax* value for this parameter in this animal. Data are **hatched** for the 7 animals in which the EG eye was perfusion-fixed at IOP 30 or 45 mmHg and are **solid** for the 14 animals in which the

EG eye was perfusion-fixed at intraocular pressure (IOP) 10 mmHg. Positive EG versus Control eye difference are red, negative are blue.

Reproduced from Yang, H., Ren, R., Lockwood, H., Williams, G., Libertiaux, V., Downs, C., Gardiner, S.K., Burgoyne, C.F., 2015. The Connective Tissue Components of Optic Nerve Head Cupping in Monkey Experimental Glaucoma Part 1: Global Change. *Invest Ophthalmol Vis Sci* 56, 7661–7678, with permission from the Association for Research in Vision and Ophthalmology (Yang et al., 2015a).

Author Manuscript

Author Manuscript

Author Manuscript

Author Manuscript

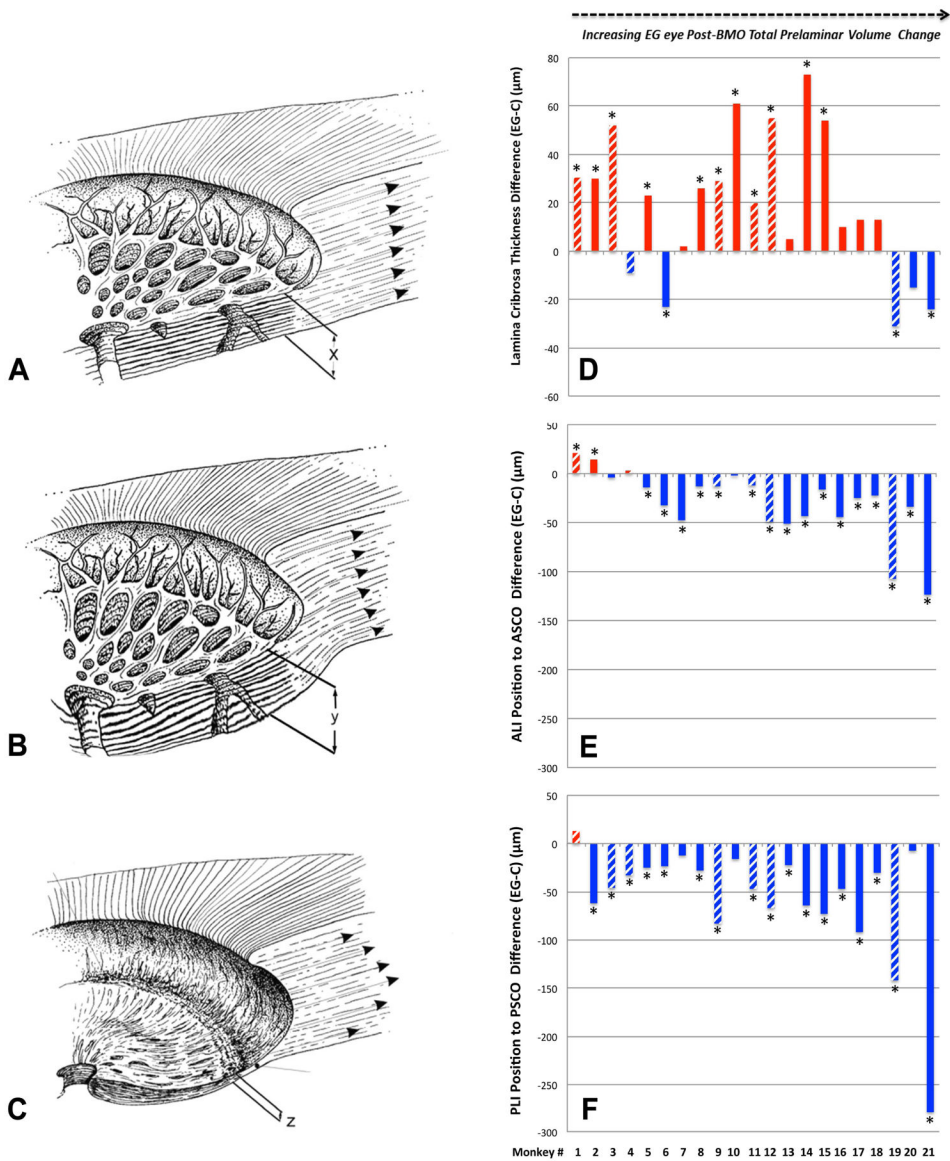


Figure 18. Lamina Cribrosa Thickness Alteration in Monkey Experimental Glaucoma (EG) (A–C)
 See Section 3.2 and Figure 8, above for additional details. (A–C) Schematic depiction of the lamina in a normal (A), early EG (B) and endstage EG (C) eye. EG vs Control eye difference in *Lamina Cribrosa Thickness* (D), *Anterior laminal insertion (ALI) position* (E), and *posterior laminal insertion (PLI) position* (F) are also shown. While laminal thickness was increased in most EG eyes with early deformation, it was either less thickened or thinned in the most deformed eyes. Anterior (inward) migration of the anterior laminal insertion (E) was present in the 2 EG eyes with the least deformation. Progressive posterior (outward) migration of the anterior laminal insertion was detected in the 17 EG eyes demonstrating the largest deformation. Posterior laminal insertion migration (F) was outward in early deformation though its magnitude diminished in moderate deformation then progressively increased in the EG eyes with the greatest deformation. **Hatched** color bars in

(D)–(F) represent EG eyes perfusion fixed at 30 or 45 mmHg and **solid** color bars represent EG eyes perfusion fixed at an intraocular pressure of 10 mmHg. (*) indicates the EG vs Control eye difference exceeds the *PIDmax* for this parameter in this animal. Positive EG versus Control Eye differences are red, negative are blue.

Panels A, B, C reprinted from Yang, H., et al. (2015). “The Connective Tissue Components of Optic Nerve Head Cupping in Monkey Experimental Glaucoma Part 1: Global Change.” *Invest Ophthalmol Vis Sci* 56(13): 7661–7678, with permission from Association for Research in Vision and Ophthalmology (Yang et al., 2015a)

Panels D, E, F Reproduced from Yang, H., Ren, R., Lockwood, H., Williams, G., Libertiaux, V., Downs, C., Gardiner, S.K., Burgoyne, C.F., 2015. The Connective Tissue Components of Optic Nerve Head Cupping in Monkey Experimental Glaucoma Part 1: Global Change. *Invest Ophthalmol Vis Sci* 56, 7661–7678, with permission from the Association for Research in Vision and Ophthalmology (Yang et al., 2015a).

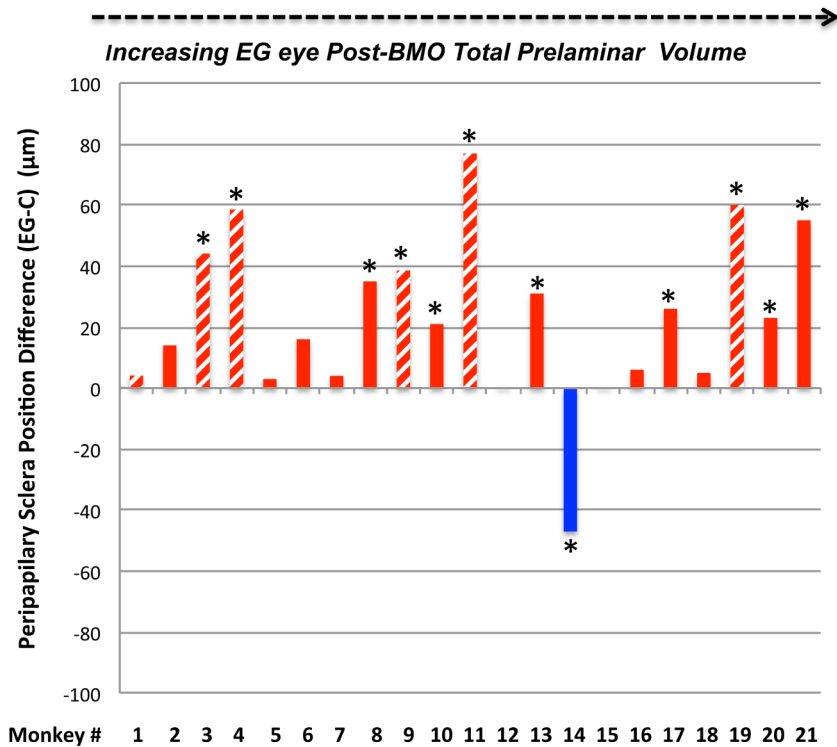


Figure 19. Experimental Glaucoma (EG) Eye Peripapillary Scleral Posterior Bowing achieves its maximum value at moderate levels of Post-BMO Total Prelaminar Volume Expansion and is not progressive beyond this point

See Section 3.2 for details. Hatched color bars in (D)–(G) represent EG eyes perfusion fixed at intraocular pressures (IOPs) of 30 or 45 mmHg and solid color bars represent EG eyes perfusion fixed at 10 mmHg. (*) indicates the EG vs Control eye difference exceeds the *PIDmax* for this parameter in this animal. By convention, a positive EG vs Control eye difference (green bars) is present when the EG eye peripapillary sclera is more anterior relative to the BMO reference plane of the EG eye than in the control eye (see EG 11 and EG 21 data of Figure 10). This finding is indirect evidence of posterior peripapillary scleral bowing in the EG eye because as the sclera bows outward BMO and its reference plane assume a position that is “more posterior to” the peripapillary scleral. By convention, a negative EG vs Control eye difference (pink bar) is present when the EG eye peripapillary sclera is more posterior relative to the BMO reference plane of the EG eye than in the control eye. Only one animal demonstrates this change (Monkey 14). Finally, of all of the connective tissue parameters, *Peripapillary Scleral Position* may have been most influenced by the level of IOP at the time of fixation. If the hatched bars are removed, the number of eyes demonstrating EG vs Control Eye differences exceeding 40 μm is reduced from 5 to 1 (Monkey 21, only). While the large values among the IOP 30 and 45 mmHg may also represent fixed deformation (i.e. we cannot be certain they would be smaller at IOP 10 mmHg), they are compatible with the concept that the range of peripapillary scleral deformation we report may include a reversible component.

Reproduced from Yang, H., Ren, R., Lockwood, H., Williams, G., Libertiaux, V., Downs, C., Gardiner, S.K., Burgoyne, C.F., 2015. The Connective Tissue Components of Optic Nerve

Head Cupping in Monkey Experimental Glaucoma Part 1: Global Change. Invest Ophthalmol Vis Sci 56, 7661–7678, with permission from the Association for Research in Vision and Ophthalmology (Yang et al., 2015a).

Author Manuscript

Author Manuscript

Author Manuscript

Author Manuscript

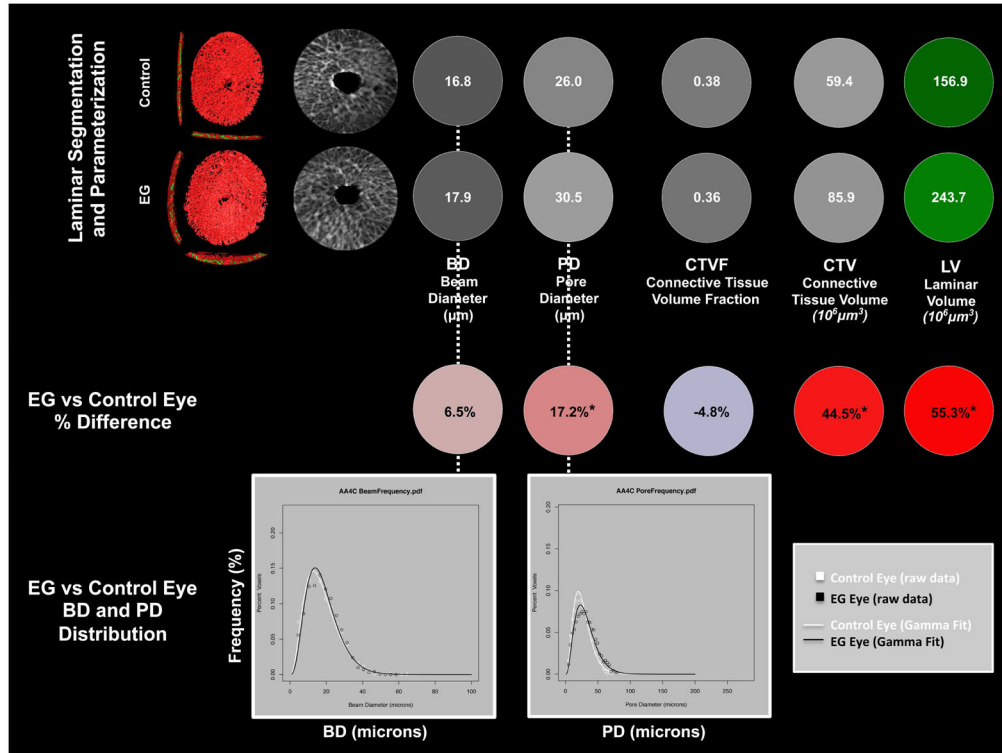


Figure 20. Laminar Microarchitecture (LMA) in early Experimental Glaucoma (EG) - Method Overview (Reynaud et al., 2016)

See Section 3.3 for details. **Upper two rows.** For both the control and EG eye of Animal 11, segmented lamina cribrosa (LC) (Figures 21 and 22) with beam and pore diameters (Figure 22) assigned to each beam and pore voxel are cylinderized (Figures 23 – 24) in right eye orientation (Figure 40 and 41). The global mean *beam diameter (BD)*, mean *pore diameter (PD)*, *Connective Tissue Volume Fraction (CTVF)*, *Connective Tissue Volume (CTV)* and *Laminar Volume (LV)* are reported in white font for each eye on a grey or green scale background (grey and green scales not shown). For all connective tissue and pore parameters, scaling is adjusted so that white suggests more and black suggests less connective tissue. *LV* is depicted in green because it is not solely related to connective tissue. **Middle Row.** Global EG versus Control eye differences in each parameter are reported in black font on a red (increased) or blue (decreased) background (color scales not shown). Asterisks (*) denote that the EG versus Control eye difference for this parameter exceeds the *maximum Physiologic Inter-eye Percent Difference Value (PIPD_{max})* for that parameter as determined by 6 bilateral normal animals (Reynaud et al., 2016). An additional analysis considers EG versus Control eye comparisons that are confined to the inner (1/3), middle (1/3) and outer (1/3) LC layers (not shown). **Bottom Row.** *BD* and *PD* frequency data (Figure 25) are fitted with Gamma distribution to more robustly assess if there is a shape or scale change in the distribution of beam and pore diameters within the EG compared to the Control eye of each animal.

Reproduced from Reynaud, J., Lockwood, H., Gardiner, S.K., Williams, G., Yang, H., Burgoyne, C.F., 2016. Lamina Cribrosa Microarchitecture in Monkey Early Experimental

Glaucoma: Global Change. Invest Ophthalmol Vis Sci 57, 3451–3469, under the CC BY-NC-ND 4.0 license (Reynaud et al., 2016).

Author Manuscript

Author Manuscript

Author Manuscript

Author Manuscript

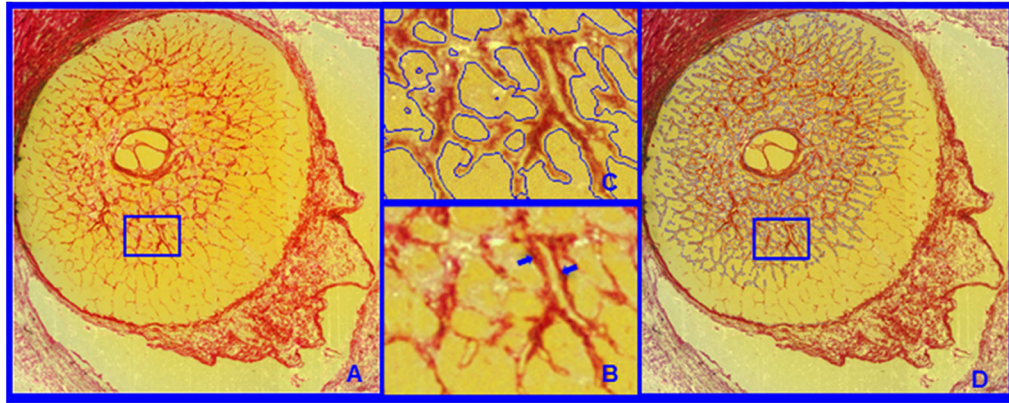


Figure 21. Laminar Microarchitecture (LMA) in early Experimental Glaucoma (EG) - Representative Segmentation Endpoints for the High Resolution 3D Histomorphometric (HMRN) Data Sets (Lockwood et al., 2015; Reynaud et al., 2016)

See Section 3.3 for details. **(A)** Representative digital section image from a high resolution 3D HMRN are shown. Magnified regions of unsegmented LC beams are shown in **(B)**. An LC beam with its central capillary is shown by blue arrows. Note that an algorithm may easily segment this single beam as two (smaller) beams if the capillary space is considered an LC pore. Because they contain more detail, this is more likely to occur within high-resolution HMRNs. Since our initial report (Grau et al., 2006) we adjusted the segmentation algorithm to achieve consistent inclusion of the capillary within the LC beam by visual inspection **(C)**. Note that LC beam segmentation is a 3D process in that data from 7 section images on either side of a given section image are included in the assignment of beam borders **(D)**. Once segmented, the algorithm fills in the LC beam capillary space by classifying each capillary lumen as connective tissue. See Figure 22 for a higher magnified version of LC beam segmentation within C and D.

Reproduced from Lockwood, H., Reynaud, J., Gardiner, S., Grimm, J., Libertiaux, V., Downs, J.C., Yang, H., Burgoyne, C.F., 2015. Lamina cribrosa microarchitecture in normal monkey eyes part 1: methods and initial results. *Invest Ophthalmol Vis Sci* 56, 1618–1637, with permission from the Association for Research in Vision and Ophthalmology (Lockwood et al., 2015).

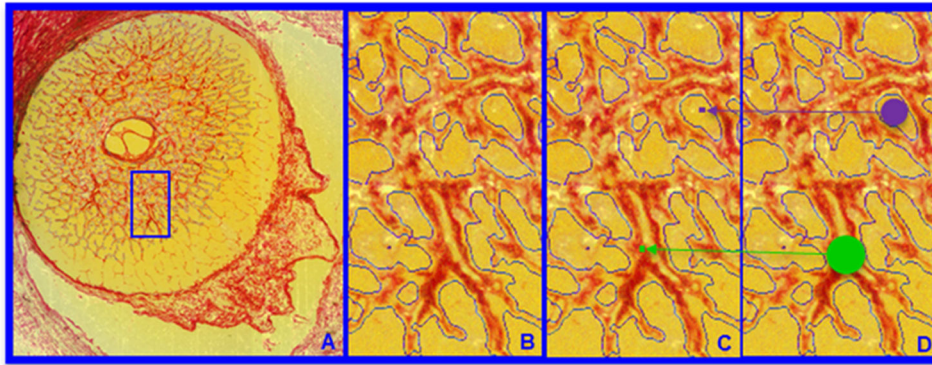


Figure 22. Laminar Microarchitecture (LMA) in early Experimental Glaucoma (EG) – Lamina Cribrosa (LC) Beam and Pore Diameter (Lockwood et al., 2015; Reynaud et al., 2016)

See Section 3.3 for details. Within each LC 3D HMRN reconstruction, beam voxels are segmented (shown within a single section image in (A) - and magnified in (B)). All beam voxels are identified as connective tissue (one representative beam voxel is represented by a green dot in (C)). All remaining voxels are “pore” voxels (one representative pore voxel is represented by a purple dot in (C)). Each beam or pore voxel is assigned a beam or pore diameter which is the diameter of the largest sphere that contains that voxel and fits into either the beam or pore in which it sits (D) (Dougherty and Kunzelmann, 2007; Hildebrand and Rüegsegger, 1997; Saito and Toriwaki, 1994). Beam or pore diameter for a given beam or region is defined by the population of beam or pore diameters of the constituent voxels. Reproduced from Lockwood, H., Reynaud, J., Gardiner, S., Grimm, J., Libertiaux, V., Downs, J.C., Yang, H., Burgoyne, C.F., 2015. Lamina cribrosa microarchitecture in normal monkey eyes part 1: methods and initial results. *Invest Ophthalmol Vis Sci* 56, 1618–1637, with permission from the Association for Research in Vision and Ophthalmology (Lockwood et al., 2015).

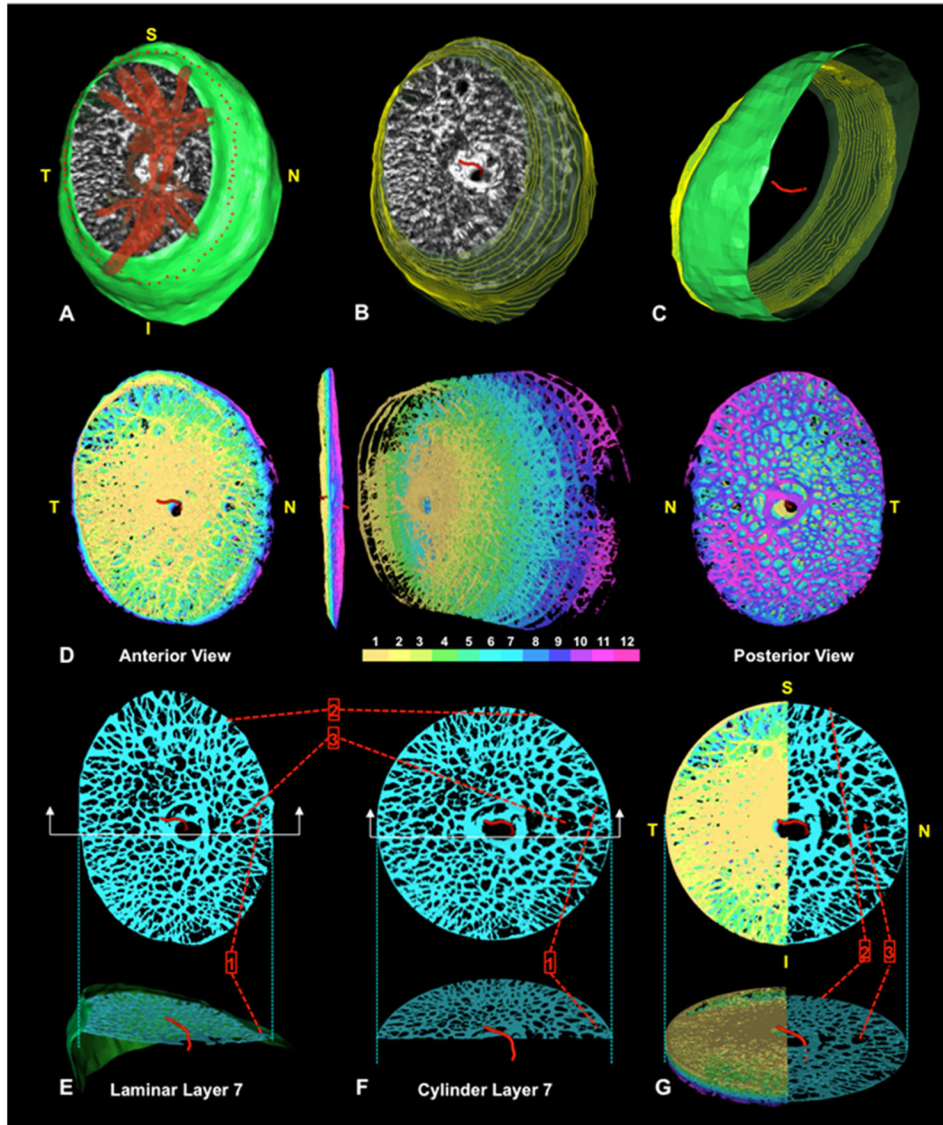


Figure 23. Laminar Microarchitecture (LMA) in early Experimental Glaucoma (EG) - Transformation of Each Lamina Cribrosa Voxel to a Common Cylinder (Lockwood et al., 2015; Reynaud et al., 2016)

See Section 3.3 for details. Panels A–G are screen captures of live data from control eye of Study Animal 11 during cylinderization. **(A)** Isolated LC segmentation and vessel tree with its neural boundary surface (green). The delineated anterior LC insertion (ALI) points are shown in red along the neural boundary surface. **(B)** Vessel tree removed to reveal the anterior neural boundary centroid spline (red) and neural boundary contours projected as faint yellow lines through the neural boundary surface. **(C)** View from the underside with the LC removed to reveal the posterior extent of the neural boundary centroid spline relative to the inner neural boundary surface (contours again shown in yellow). The centroid spline passes through the center of mass of each neural boundary contour. **(D)** To cylinderize the data, each LC voxel is assigned to one of 12 layers. Anterior (left), side (middle left), exploded (middle right) and posterior (right) views are shown. **(E)** Layer 7 voxels in pre-

cylinder orientation depicting specific voxel locations within the LC structure using pointers 1, 2, and 3. Below the corresponding side cutout view is shown with pointer 1 identifying three pores along the border of the nasal neural boundary. **(F and G)** Layer 7 voxels after cylinderization. Figure 23, explains the voxel specific calculations that underlie this transformation. Note the location of 3 corresponding individual voxel locations shown with pointers in (E), (F) and (G). Note that the central and peripheral location of voxels pre-cylinderization remain after they are cylinderized. **(G)** All 12 layers of cylinderized LC voxels are shown to the left of the superior/inferior axis. Layer 7 is isolated to the right. Below is a side view of the same rendering. Note that every beam or pore voxel has a diameter assigned (Figure 22) prior to cylinderization that is retained throughout the cylinderization process. Voxel size is not modified. Only voxel locations are modified during cylinderization. In polar coordinates (r, theta), theta is held constant while r is adjusted as depicted in Figure 24.

Reproduced from Lockwood, H., Reynaud, J., Gardiner, S., Grimm, J., Libertiaux, V., Downs, J.C., Yang, H., Burgoyne, C.F., 2015. Lamina cribrosa microarchitecture in normal monkey eyes part 1: methods and initial results. *Invest Ophthalmol Vis Sci* 56, 1618–1637, with permission from the Association for Research in Vision and Ophthalmology (Lockwood et al., 2015).

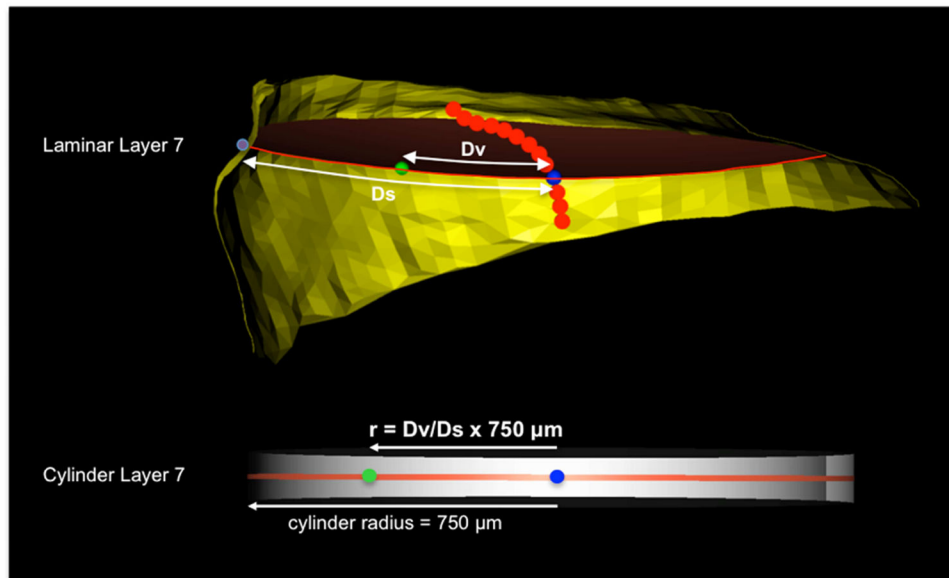


Figure 24. Laminar Microarchitecture (LMA) in early Experimental Glaucoma (EG) - Cylinderization of a Representative LC Voxel Assigned to Layer 7 of a control eye (Lockwood et al., 2015; Reynaud et al., 2016)

See Section 3.3 for details. **(Upper)** All LC voxels within LC layer 7 of the pre-cylinderized LC, Figure 23, above), are assigned a polar coordinate (D_v , θ) where D_v is the distance along the mid-layer reference surface (red) from the neural boundary centroid spline (red dots) centroid (blue dot) and D_s is the radial distance along the surface of the mid-layer reference surface from the centroid to the neural boundary (yellow). **(Lower)** Within cylinder layer 7, θ is held constant, but r is proportionally adjusted using the precylinder ratio of D_v/D_s and the cylinder radius of $750 \mu\text{m}$. Distances D_v and D_s are calculated along a pre-cylinderized reference layer surface contour (curve) that is obtained for every LC voxel. It is not a straight-line measurement in a plane.

Reproduced from Lockwood, H., Reynaud, J., Gardiner, S., Grimm, J., Libertiaux, V., Downs, J.C., Yang, H., Burgoyne, C.F., 2015. Lamina cribrosa microarchitecture in normal monkey eyes part 1: methods and initial results. *Invest Ophthalmol Vis Sci* 56, 1618–1637, with permission from the Association for Research in Vision and Ophthalmology (Lockwood et al., 2015).

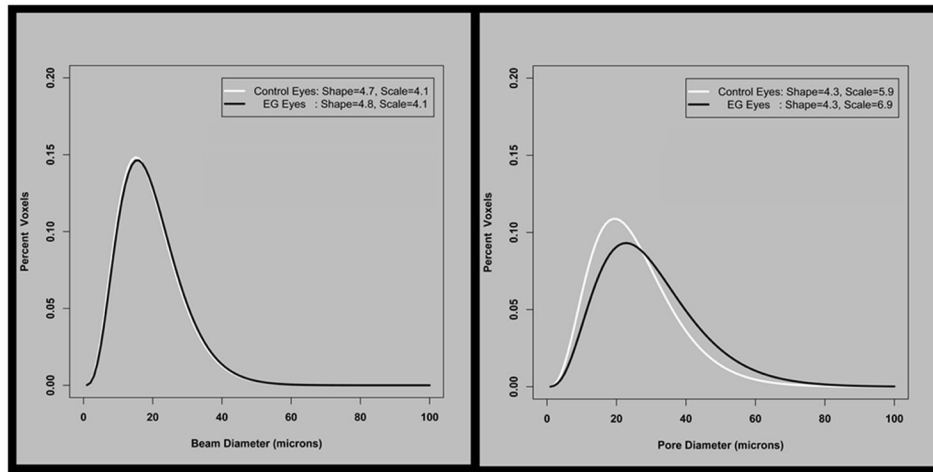


Figure 25. Laminar Microarchitecture (LMA) in early Experimental Glaucoma (EG) - The Frequency Distribution of *Beam* and *Pore* Diameters for the 14 EG Animals, fit to a Gamma Distribution (Reynaud et al., 2016)

See Section 3.3 for details. The two fitted parameters that describe the Gamma distribution are in the corner of each plot. For beam diameter, neither *Shape* nor *Scale* change significantly. For pore diameter, there is no difference in *Shape*, but *Scale* has increased, equivalent to all pores being 17% larger) in the EG eyes.

Reproduced from Reynaud, J., Lockwood, H., Gardiner, S.K., Williams, G., Yang, H., Burgoyne, C.F., 2016. Lamina Cribrosa Microarchitecture in Monkey Early Experimental Glaucoma: Global Change. *Invest Ophthalmol Vis Sci* 57, 3451–3469, under the CC BY-NC-ND 4.0 license (Reynaud et al., 2016).

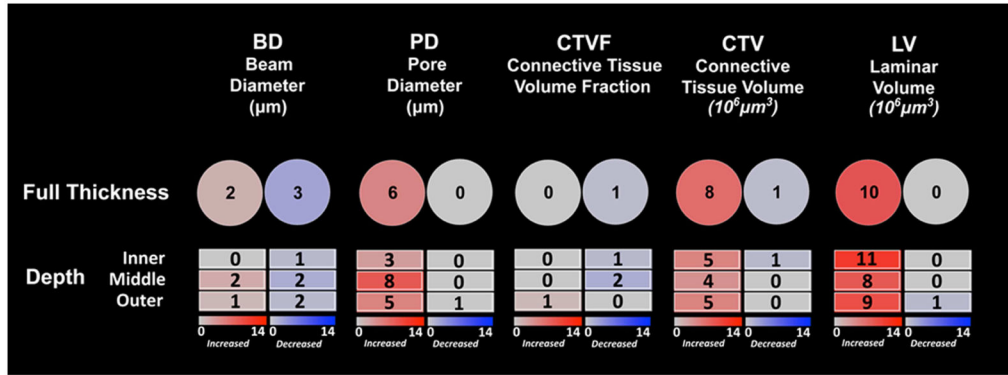


Figure 26. Laminar Microarchitecture (LMA) in early Experimental Glaucoma (EG) - Frequency and Direction of Animal Specific LMA Parameter Change by Depth (Reynaud et al., 2016)

See Section 3.3 for details. The total number of animals demonstrating EG versus Control eye increases (red) and decreases (blue) exceeding the *Physiologic Inter-eye Percent Difference maximum (PIPDmax)* for each parameter are reported. **Lower Three Rows.** Similar data for the inner, middle and outer LC layers are reported.

Reproduced from Reynaud, J., Lockwood, H., Gardiner, S.K., Williams, G., Yang, H., Burgoyne, C.F., 2016. Lamina Cribrosa Microarchitecture in Monkey Early Experimental Glaucoma: Global Change. *Invest Ophthalmol Vis Sci* 57, 3451–3469, under the CC BY-NC-ND 4.0 license (Reynaud et al., 2016).

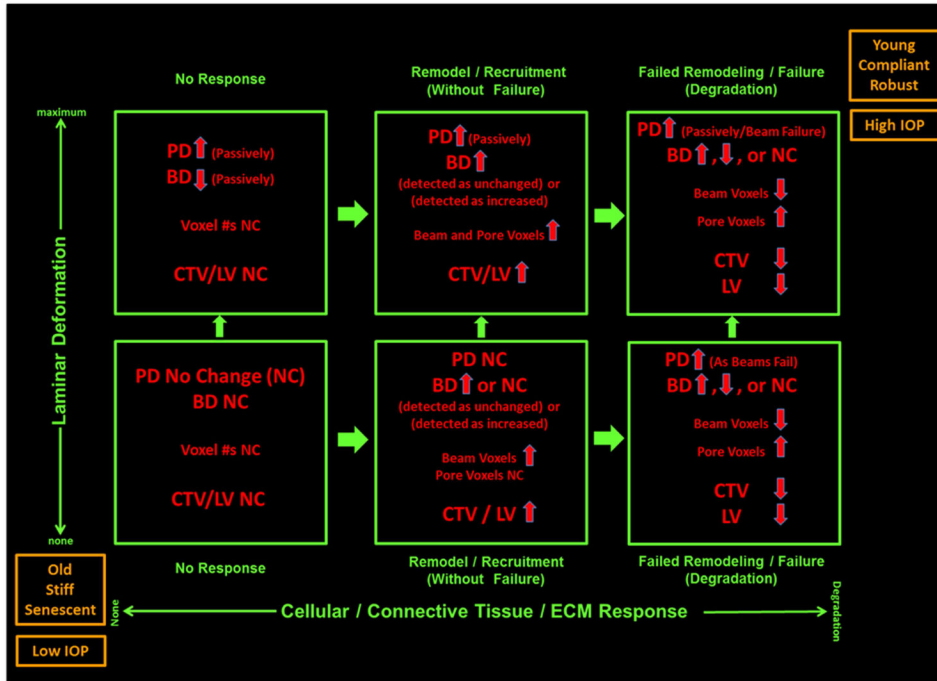


Figure 27. Post-mortem EG versus Control Eye Differences in Laminar Microarchitecture (LMA) Reflect Both Passive Connective Tissue Deformation (vertical axis) and Active Connective Tissue Synthesis, Remodeling and Mechanical Failure (horizontal axis) (Reynaud et al., 2016)

See Section 3.3 for details. For a given optic nerve head (ONH) the magnitude of deformation (increasing up) and the magnitude of connective tissue synthesis and remodeling (increasing to the right) govern the character of detected post-mortem EG versus Control eye differences in LC microarchitecture. Animal age (as a surrogate for stiff versus compliant tissues and/or senescent versus robust cells at any age) and the magnitude of IOP insult (both bottom left and upper right) independently influence both the magnitude of deformation and the character of the connective tissue response. *IOP* – *intraocular pressure*; *PD* – *pore diameter*; *BD* – *beam diameter*; *CTV* – *connective tissue volume*; *LV* – *Lamina Cribrosa volume*; *ECM* – *extracellular matrix*; *NC* – *no (detectable) change*.

Reproduced from Reynaud, J., Lockwood, H., Gardiner, S.K., Williams, G., Yang, H., Burgoyne, C.F., 2016. Lamina Cribrosa Microarchitecture in Monkey Early Experimental Glaucoma: Global Change. *Invest Ophthalmol Vis Sci* 57, 3451–3469, under the CC BY-NC-ND 4.0 license (Reynaud et al., 2016).

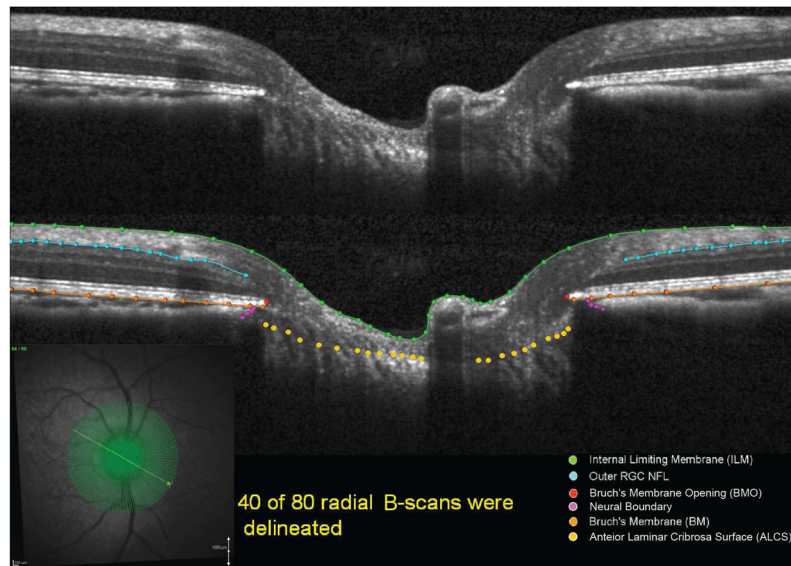


Figure 28. Optical Coherence Tomography (OCT) Methods - Original and Delineated OCT Optic Nerve Head (ONH) data sets in a Normal Monkey Eye

See Section 3.5 for details. Green lines/points: internal limiting membrane (ILM); blue lines/points: outer boundary of the RNFL; orange lines/points: Bruch's membrane/retinal pigment epithelium (BM/RPE); red points: Bruch's membrane opening (BMO); purple points: Border Tissue of Elschnig (BTE); yellow points: anterior lamina cribrosa surface (ALCS). Eighty radial B-scans are acquired (bottom left in green) and 40 (every other B-scan) are delineated.

Reproduced from He, L., Yang, H., Gardiner, S.K., Williams, G., Hardin, C., Strouthidis, N.G., Fortune, B., Burgoyne, C.F., 2014. Longitudinal detection of optic nerve head changes by spectral domain optical coherence tomography in early experimental glaucoma. *Invest Ophthalmol Vis Sci* 55, 574–586, with permission from the Association for Research in Vision and Ophthalmology (He et al., 2014b).

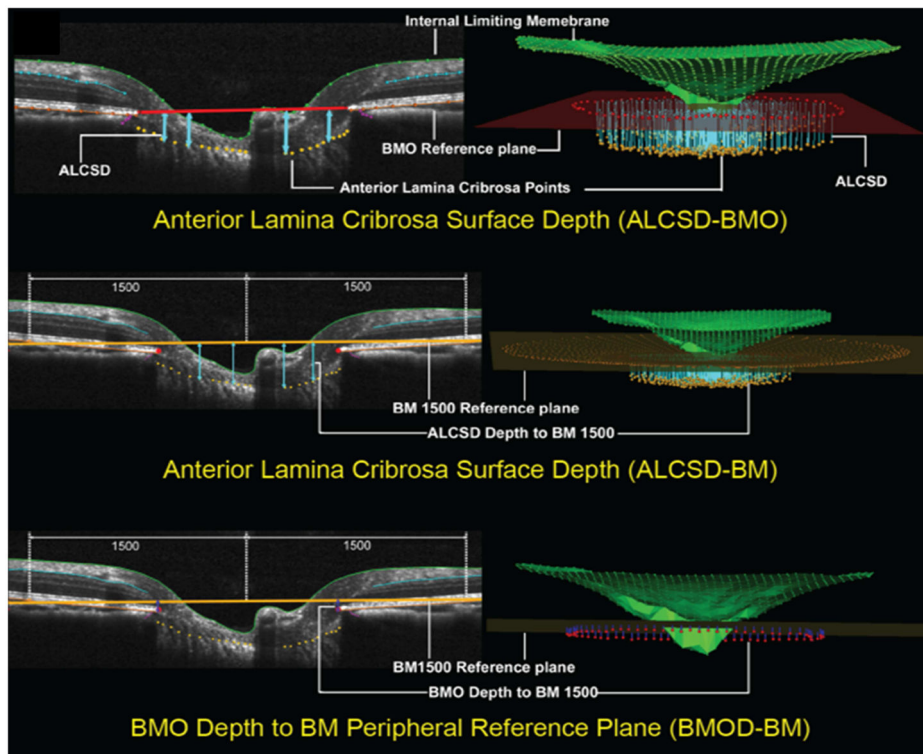


Figure 29. Optical Coherence Tomography (OCT) Parameters Grouped by Target Tissue –Optic Nerve Head (ONH) Connective Tissues

See Section 3.5 for details. OCT ONH connective tissue parameters are designed to detect connective tissue deformation (reversible) and or remodeling (permanent). *Anterior lamina cribrosa surface (ALCS) depth* (blue arrows) is measured at each delineated ALCS point as the perpendicular distance from the BMO reference plane (red line) (*Top*) and BM reference plane (orange line) defined by two delineated BM points at 1500 μm eccentricity from the BMO centroid (*Middle*). *BMO Depth* is measured at each delineated BMO point as the perpendicular distance from the BM reference plane (orange line) (*Bottom*). Movement of BMO, relative to a peripheral BM reference plane can be due to choroidal thinning and/or outward bowing of the peripapillary sclera.

Reproduced from He, L., Yang, H., Gardiner, S.K., Williams, G., Hardin, C., Strouthidis, N.G., Fortune, B., Burgoyne, C.F., 2014. Longitudinal detection of optic nerve head changes by spectral domain optical coherence tomography in early experimental glaucoma. *Invest Ophthalmol Vis Sci* 55, 574–586, with permission from the Association for Research in Vision and Ophthalmology (He et al., 2014b).

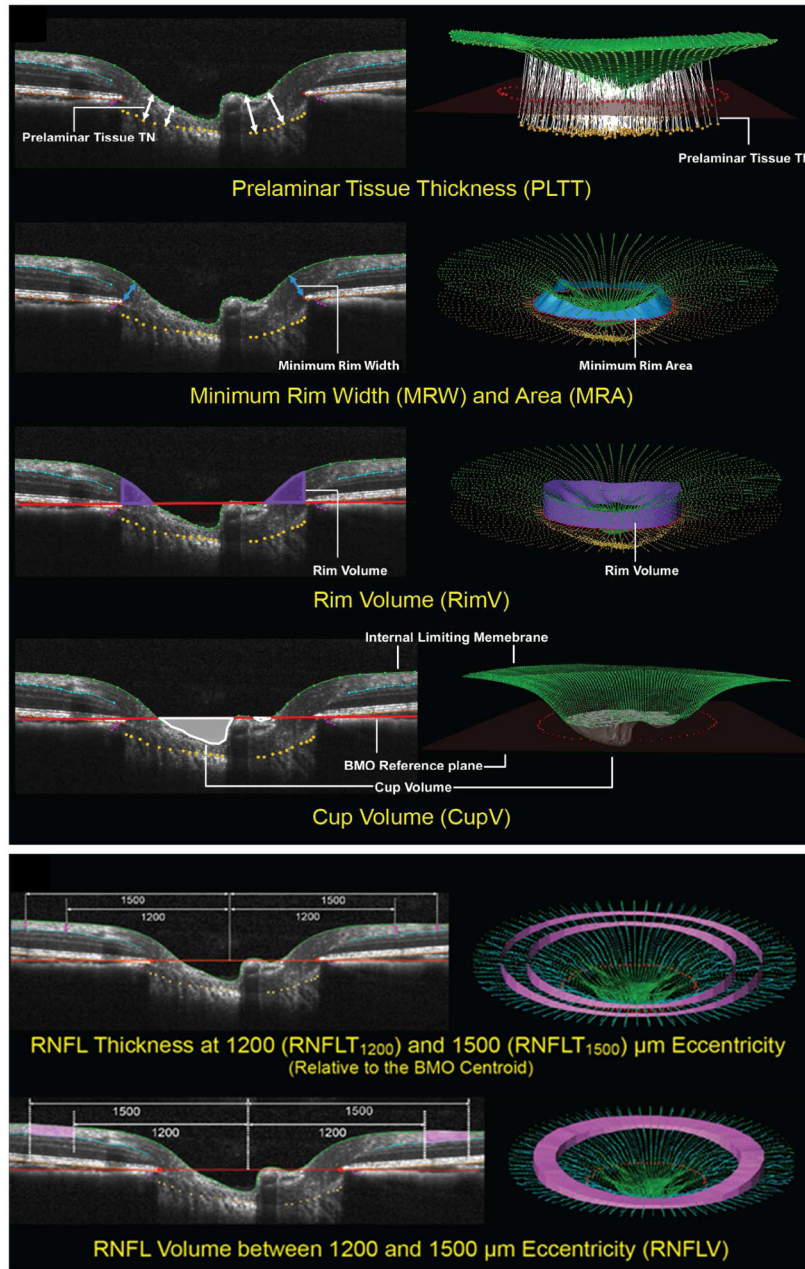


Figure 30. Optical Coherence Tomography (OCT) Parameters Grouped by Target Tissue – Neural Tissues

See Section 3.5 for details. **(Upper) ONH Neural Tissues.** Neural tissue parameters are designed to detect neural tissue changes that occur either due to neural tissue damage or secondary to connective tissue deformation. *Prelaminar tissue thickness (PLTT)* is measured as the normal from the tangent to the anterior lamina cribrosa surface (ALCS) to the internal limiting membrane (ILM, green line) (*Top*). *Minimum Rim Width (MRW)* - blue arrows) is measured at each delineated BMO point (red) as the minimum distance to ILM (*upper middle*). When viewed in a 3-D domain, the *MRW* can be translated into *Minimum Rim Area (MRA)*. *Rim volume* (purple) is calculated from the volume bounded by ILM (green),

BMO reference plane (red) and perpendicular line through the BMO (*lower middle*). *Cup volume* (grey) is generated from the volume between ILM B-spline surface and the BMO reference plane (*Bottom*). **(Lower) Non-Standard Peripapillary RNFL.** *Retinal nerve fiber layer thickness (RNFLT) 1200* is measured on either side of the posterior RNFL boundary (turquoise line) at ILM points that are 1200 μm from the centroid of the 80 delineated BMO points (the BMO centroid). Similarly, *RNFLT1500* is measured at 1500 μm from the BMO centroid (*Top*). The volume between *RNFLT*₁₂₀₀ and *RNFLT*₁₅₀₀ is defined as *RNFL volume* (pink) (*Bottom*).

Reproduced from He, L., Yang, H., Gardiner, S.K., Williams, G., Hardin, C., Strouthidis, N.G., Fortune, B., Burgoyne, C.F., 2014. Longitudinal detection of optic nerve head changes by spectral domain optical coherence tomography in early experimental glaucoma. *Invest Ophthalmol Vis Sci* 55, 574–586, with permission from the Association for Research in Vision and Ophthalmology (He et al., 2014b).

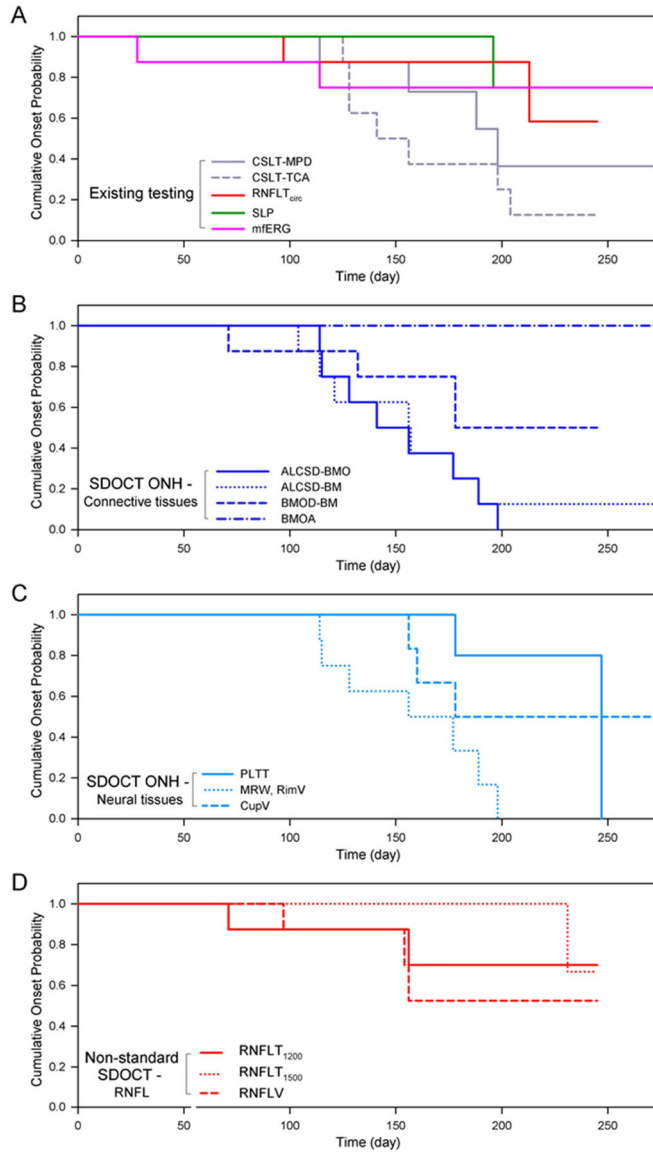


Figure 31. Optical Coherence Tomography (OCT) in early Experimental Glaucoma (EG) Result - Kaplan-Meier analysis of event-based onset in the 8 EG eyes by post-laser time, testing modality and OCT parameter type

See Section 3.5 for details. **(A)** Existing Testing Modalities including CSLT, SLP and mfERG. **(B)** OCT ONH Connective Tissue parameters. **(C)** OCT ONH Neural Tissue Parameters. **(D)** OCT RNFL parameters. When compared at similar post-laser days, change detection in the OCT ONH parameters ALCSD-BMO and *MRW/rim volume* and in the CSLT ONH surface parameters occurred earliest and was most frequent in these 8 EG eyes. Reproduced from He, L., Yang, H., Gardiner, S.K., Williams, G., Hardin, C., Strouthidis, N.G., Fortune, B., Burgoyne, C.F., 2014. Longitudinal detection of optic nerve head changes by spectral domain optical coherence tomography in early experimental glaucoma. *Invest Ophthalmol Vis Sci* 55, 574–586, with permission from the Association for Research in Vision and Ophthalmology (He et al., 2014b).

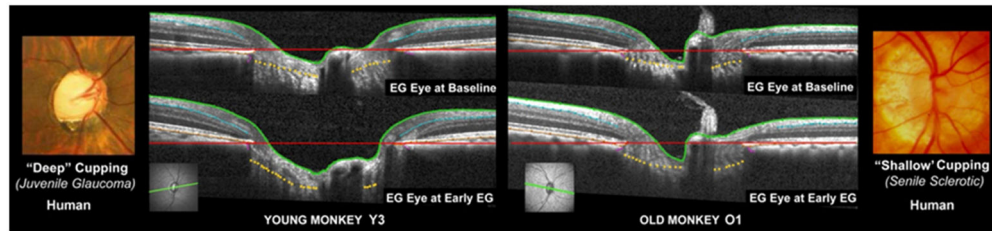


Figure 32. Differences in Optic Nerve Head (ONH) Connective Tissue Structural Stiffness and/or Remodeling may underlie “Deep” (left) and “Shallow” (right) Forms of Glaucomatous Cupping in Monkeys and Humans

See Section 3.6 for details. OCT ONH B-scans from the same location (green, lower left) from the EG eye of a young (left) and old (right) monkey, when the eye was normal (upper) and at the second confirmation of CSLT detection of ONH surface change in the young eye (lower left) and at the (later) pre-sacrifice data set in the old eye (lower right). All images were obtained after 30 minutes of manometer controlled IOP (10 mm Hg). In both eyes, while prelaminar neural tissue thickness alterations are present, laminar deformation is also apparent as an increase in the magnitude of space between the Bruch’s membrane opening reference plane (red line) and the anterior lamina cribrosa surface (gold dots). Laminar deformation in the old eye is far less than in the young eye and this profound difference in laminar deformation occurred in the setting of a cumulative IOP insult that was approximately 5 times greater in the old eye.

Reproduced from Yang, H., He, L., Gardiner, S.K., Reynaud, J., Williams, G., Hardin, C., Strouthidis, N.G., Downs, J.C., Fortune, B., Burgoyne, C.F., 2014. Age-related differences in longitudinal structural change by spectral-domain optical coherence tomography in early experimental glaucoma. *Invest Ophthalmol Vis Sci* 55, 6409–6420, with permission from the Association for Research in Vision and Ophthalmology (Yang et al., 2014b).

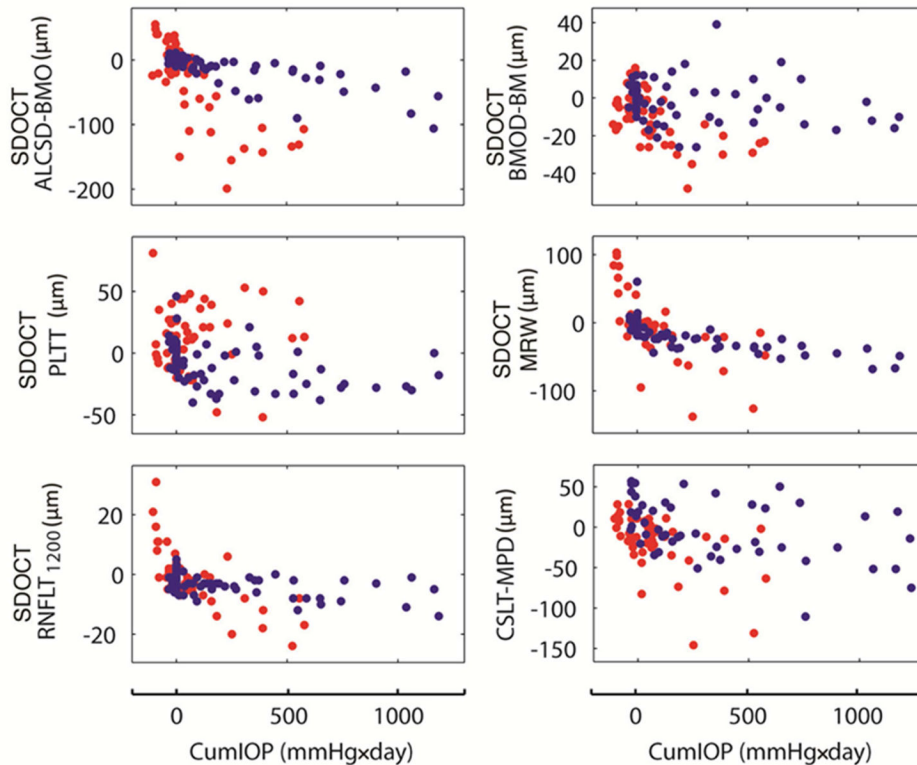


Figure 33. Age related differences in Optical Coherence Tomography (OCT) in early Experimental Glaucoma (EG)

See Section 3.6 for details. Change from baseline for selected testing modalities and parameters at each post-laser testing session in young (red) and old (blue) EG eyes plotted relative to *Cumulative Intraocular Pressure (IOP) Insult* (Yang et al., 2014b). Testing sessions are ordered by EG eye *Cumulative IOP insult* (bottom of each column). Change from Baseline for each parameter at each post-laser testing session is plotted for all 4 young (red dots) and all 4 old (blue dots) EG eyes. Note the following. First, in general, the young eyes were followed to lower levels of *cumulative IOP insult* than the old eyes (red dots end at less than 600 mmHg× day and blue dots extend to more than 1200 mmHg×day) reflecting the fact that ONH surface change as detected by CSLT occurred at lower levels of *cumulative IOP insult* in young eyes. Second, age-related differences in the overall rates of change are apparent qualitatively for a majority of the parameters and were confirmed as statistically significant for a subset of parameters.

Reproduced from Yang, H., He, L., Gardiner, S.K., Reynaud, J., Williams, G., Hardin, C., Strouthidis, N.G., Downs, J.C., Fortune, B., Burgoyne, C.F., 2014. Age-related differences in longitudinal structural change by spectral-domain optical coherence tomography in early experimental glaucoma. *Invest Ophthalmol Vis Sci* 55, 6409–6420, with permission from the Association for Research in Vision and Ophthalmology (Yang et al., 2014b).

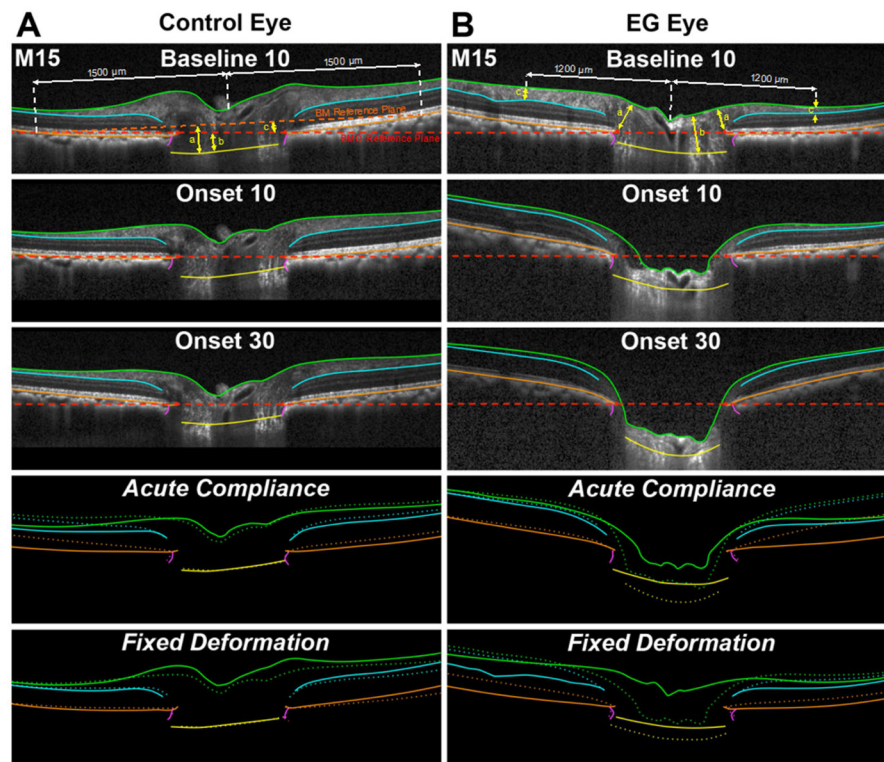


Figure 34. Optic Nerve Head (ONH) Hypercompliance in Early Experimental Glaucoma (EG) (Ivers et al., 2016)

See Section 3.7 for details. Representative B-scans from the Control (**Left**) and EG (**Right**) eyes of a representative unilateral EG monkey, with ONH and retinal anatomy delineated at baseline (pre-Laser) IOP of 10 mmHg (Baseline 10) and at EG onset at IOP 10 (Onset 10) and 30 mmHg (Onset 30) showing *Fixed Deformation* and *Acute Compliance* at EG onset. Green lines: internal limiting membrane (ILM); blue lines: outer boundary of the retinal nerve fiber layer (RNFL); orange lines: Bruch’s membrane/retinal pigment epithelium (BM/RPE); red points: Bruch’s membrane opening (BMO); purple lines: Neural Boundary; yellow points: anterior lamina cribrosa surface (ALCS). Dotted lines represent *Fixed Deformation* and *Acute Compliance* at EG onset. (**A**) Connective tissue parameters: (a) *ALCSD-BM*, (b) *ALCSD-BMO*, and (c) *BMOD-BM*. (**B**) Neural tissue parameters: (a) *MRW*, (b) *PLTT*, and (c) *RNFLT*. A substantially larger *Acute Compliance* and *Fixed Deformation* can be seen in the EG eye at EG onset compared to the fellow control eye. Comparisons in bottom 4 panels were aligned using BMO reference plane. Reproduced from Ivers, K.M., Yang, H., Gardiner, S.K., Qin, L., Reyes, L., Fortune, B., Burgoyne, C.F., 2016. In Vivo Detection of Lamellar and Peripapillary Scleral Hypercompliance in Early Monkey Experimental Glaucoma. *Invest Ophthalmol Vis Sci* 57, OCT388-403, under the CC BY-NC-ND 4.0 license (Ivers et al., 2016).

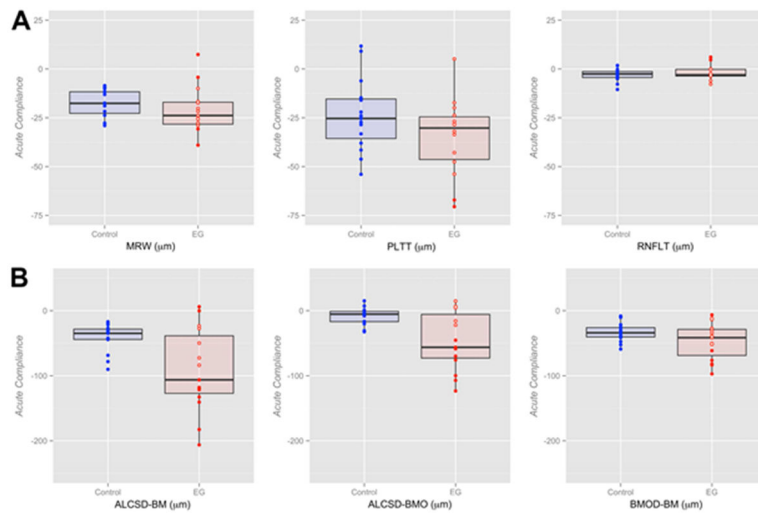


Figure 35. Box Plots Representing Distributions (Median, Interquartile Range, and Extremes) of EG (red) and Control Eye (blue) Acute Compliance at EG Onset for all Optical Coherence Tomography (OCT) Neural (A) and Connective Tissue (B) Parameters (Ivers et al., 2016)

See Section 3.7 for details. (A) The scale extends from -75 to 25 μm across all neural tissue parameters and from -250 to 50 μm across all (B) connective tissue parameters. EG eyes that fall outside the range of control eye parameters are shown as filled red circles; whereas EG eyes that are within the range of control eye parameters are shown as empty red circles (some circles overlap and appear as one). Eye-specific hypercompliance in EG eyes occurred in *MRW* (3 of 15 eyes), *PLTT* (2 of 15 eyes), *ALCSDBM* (8 of 15 eyes), *ALCSDBMO* (9 of 15 eyes), and *BMOBMBM* (4 of 15 eyes). An eye-specific decrease in compliance in EG eyes was seen in *MRW* (2 eyes), *RNFLT* (2 eyes), *ALCSDBM* (2 eyes), and *BMOBMBM* (1 eye).

Reproduced from Ivers, K.M., Yang, H., Gardiner, S.K., Qin, L., Reyes, L., Fortune, B., Burgoyne, C.F., 2016. In Vivo Detection of Lamellar and Peripapillary Scleral Hypercompliance in Early Monkey Experimental Glaucoma. *Invest Ophthalmol Vis Sci* 57, OCT388-403, under the CC BY-NC-ND 4.0 license (Ivers et al., 2016).

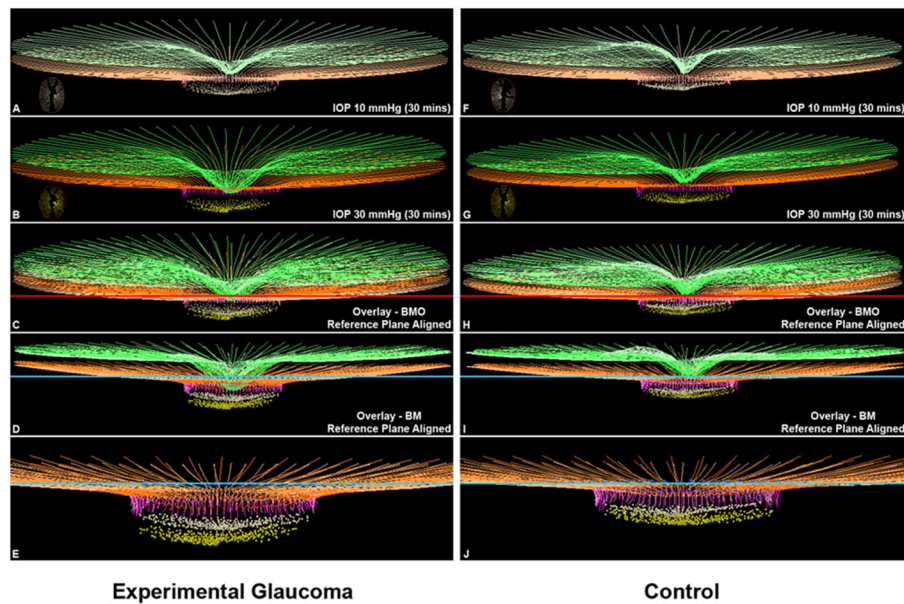


Figure 36. EG Eye Acute Compliance (left) Exceeds Control Eye Acute Compliance (right) in the Animal that Demonstrates the Greatest Control Eye Acute Compliance (Ivers et al., 2016)
 See section 3.7 for details. Delineated structures within the Intraocular Pressure (IOP) 10 (A and F) and IOP 30 mmHg (B and G) optical coherence tomography (OCT) data sets of the EG (left) and control (right) eyes of one experimental glaucoma (EG) animal. Insets in these panels are en face views of the delineated Bruch's Membrane Opening (BMO) and Anterior Lamina Cribrosa Surface (ALCS) points of each data set. In (C) and (H) the IOP 10 and IOP 30 OCT data sets have been overlaid by anchoring them to their shared BMO reference plane shown in red. In (D) and (I), the same IOP 10 and IOP 30 OCT data sets have been overlaid by anchoring them to their shared Bruch's Membrane (BM) reference plane shown in blue. Note that posterior deformation of the IOP 30 ALCS (yellow dots) is present relative to the IOP 10 ALCS (off-white dots) in (C), and this deformation is larger in (D) because it also includes posterior deformation of BM relative to its reference plane (blue line). No adjustments to z-axis magnification have been made to these images. Magnified views of Panels D and I are shown in Panels (E) and (J) absent the internal limiting membrane (ILM, green) so as to make the laminar and pp-scleral deformation components more apparent. Structures shown are ILM (green), BM (orange), BMO (red points), and ALCS (yellow points). To differentiate the structures in the overlaid images, the colors at 10 mmHg have been washed out. The control eye of this animal demonstrated the largest control eye *Acute Compliance* change in the OCT connective tissue parameters *BMOD-BM*, *ALCSD-BM*, and *ALCSD-BM*. It therefore set the upper range of control eye *Acute Compliance* used for the definition of EG eye hypercompliance ($-59\ \mu\text{m}$, $-90.1\ \mu\text{m}$, and $-32\ \mu\text{m}$, respectively). The EG eye of this animal demonstrates substantial hypercompliance for the same three parameters ($-82.0\ \mu\text{m}$, $-140.5\ \mu\text{m}$, and $-58.6\ \mu\text{m}$, respectively). The distinction between *ALCSD-BM* (which captures both pp-scleral and laminar deformation, relative to peripheral BM) and *ALCSD-BMO* (which captures laminar deformation relative to BMO, alone) can be clearly seen for both eyes by overlaying the IOP 10 and IOP 30 data sets using the BMO

reference plane (in panels C and H) or by overlapping the IOP 10 and IOP 30 data sets using the BM reference plane (in panels D and I).

Reproduced from Ivers, K.M., Yang, H., Gardiner, S.K., Qin, L., Reyes, L., Fortune, B., Burgoyne, C.F., 2016. In Vivo Detection of Lamellar and Peripapillary Scleral Hypercompliance in Early Monkey Experimental Glaucoma. *Invest Ophthalmol Vis Sci* 57, OCT388-403, under the CC BY-NC-ND 4.0 license (Ivers et al., 2016).

Author Manuscript

Author Manuscript

Author Manuscript

Author Manuscript

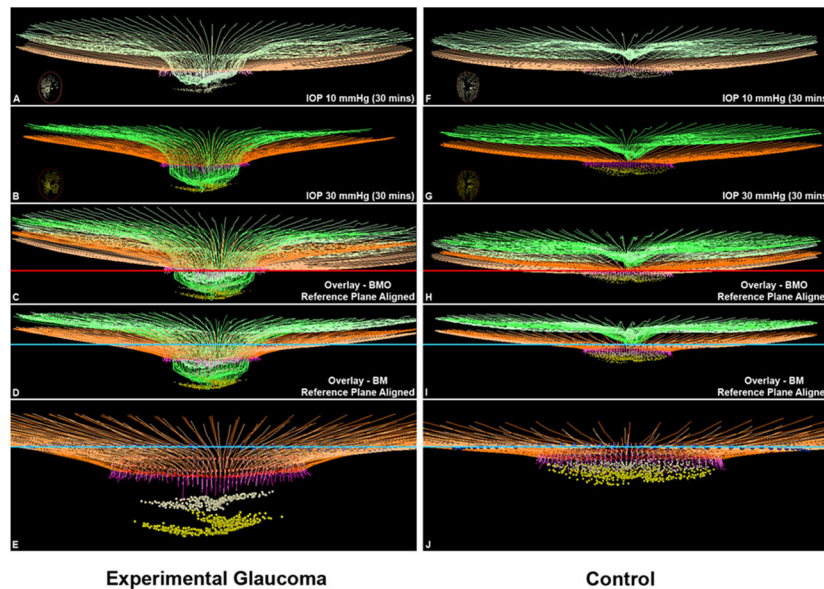


Figure 37. EG Eye Acute Compliance (left) Far Exceeds Control Eye Acute Compliance (right) in the Animal That Demonstrates the Greatest EG Eye Acute Compliance (Ivers et al., 2016)

See Section 3.7 for details. Delineated structures within the Intraocular Pressure (IOP) 10 (A and F) and IOP 30 mmHg (B and G) optical coherence tomography (OCT) data sets of the EG (left) and control (right) eyes of Animal 15. Insets in these panels are en face views of the delineated Bruch's Membrane Opening (BMO) and Anterior Lamina Cribrosa Surface (ALCS) points of each data set. In (C) and (H) the IOP 10 and IOP 30 OCT data sets have been overlaid by anchoring them to their shared BMO reference plane shown in red. In (D) and (I), the same IOP 10 and IOP 30 OCT data sets have been overlaid by anchoring them to their shared Bruch's Membrane (BM) based reference plane shown in blue. Note that posterior deformation of the IOP 30 ALCS (yellow dots) is present relative to the IOP 10 ALCS (off-white dots) in (C), and this deformation is larger in (D) because it also includes posterior deformation of BM relative to its reference plane (blue line). No adjustments to z-axis magnification have been made to these images. Magnified views of Panels D and I are shown in Panels (E) and (J) absent the internal limiting membrane (ILM, green) so as to make the laminar and pp-scleral deformation components more apparent. The structures shown are the ILM, (green), BM (orange), BMO (red points), and ALCS (yellow points). To differentiate the structures in the overlaid images, the colors at 10 mmHg have been washed out. The EG eye of this animal demonstrates the largest magnitude of EG versus control eye difference in *ALCSD-BM Acute Compliance* which was the measure used to rank the animals 1 – 15 ($-136.6 \mu\text{m}$). It also demonstrated the largest magnitude of EG versus control eye difference in *BMOD-BM* ($-44.8 \mu\text{m}$) and *ALCSD-BMO* ($-137.6 \mu\text{m}$). It therefore demonstrates the greatest magnitude of ONH laminar and pp-scleral connective tissue hypercompliance among the 15 EG eyes.

Reproduced from Ivers, K.M., Yang, H., Gardiner, S.K., Qin, L., Reyes, L., Fortune, B., Burgoyne, C.F., 2016. In Vivo Detection of Laminar and Peripapillary Scleral Hypercompliance in Early Monkey Experimental Glaucoma. *Invest Ophthalmol Vis Sci* 57, OCT388-403, under the CC BY-NC-ND 4.0 license (Ivers et al., 2016).

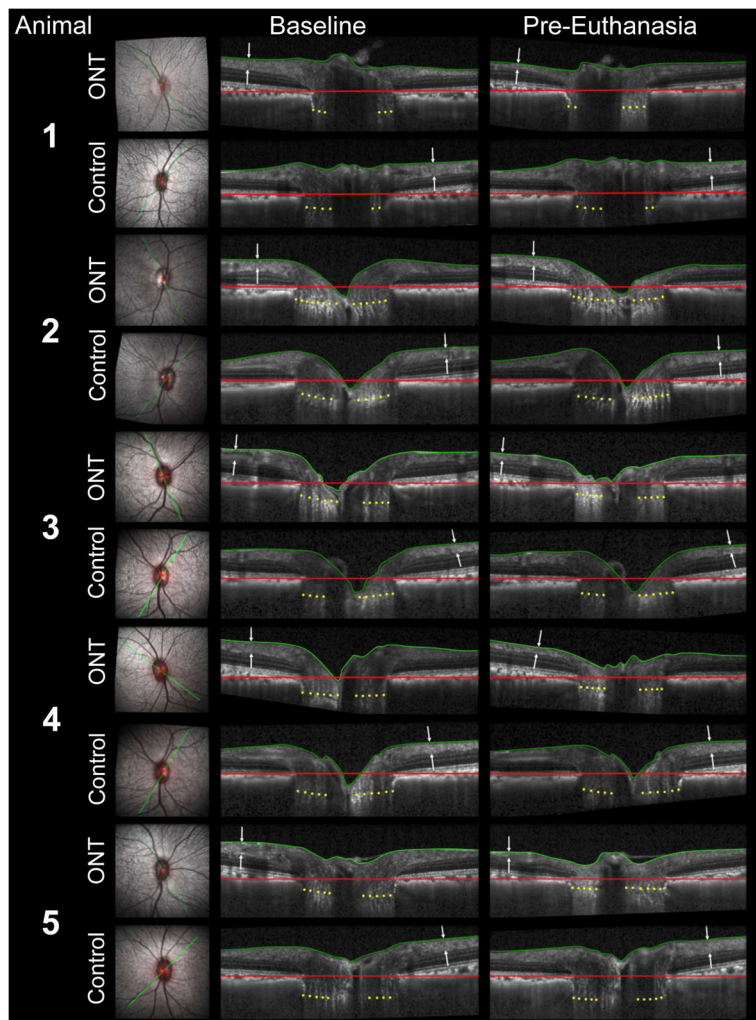


Figure 38. Representative Baseline (left) and Pre-Euthanasia (right) Radial B-scans From the Optic Nerve Transection (ONT) (upper) and Control Eyes (lower) of 5 unilateral ONT Monkeys (Ing et al., 2016)

See Section 4.0 for Details. Scanning laser ophthalmoscopy image (left) showing radial B-scan location in each eye (green line). Within each Baseline and Pre-euthanasia radial B-scan the following landmarks are delineated: Internal Limiting Membrane (ILM, green line); Bruch's membrane opening (BMO) reference plane (red line); and the anterior lamina cribrosa surface (ALCS, yellow dots). ONT-eye retinal nerve fiber layer thickness (RNFLT, white arrows) is markedly thinned within the pre-euthanasia compared to the baseline B-scans, while control eye RNFLT remains unchanged in all animals. ONT-eye ALCS position relative to the BMO reference plane remains unchanged in M1 & M2 (and moves anteriorly in M3, M4, and M5), while lamina position remains unchanged in all control eyes. Reproduced from Ing, E., Ivers, K.M., Yang, H., Gardiner, S.K., Reynaud, J., Cull, G., Wang, L., Burgoyne, C.F., 2016. Cupping in the Monkey Optic Nerve Transection Model Consists of Prelaminar Tissue Thinning in the Absence of Posterior Lamina Deformation. *Invest Ophthalmol Vis Sci* 57, 2598–2611, under the CC BY-NC-ND 4.0 license (Ing et al., 2016).

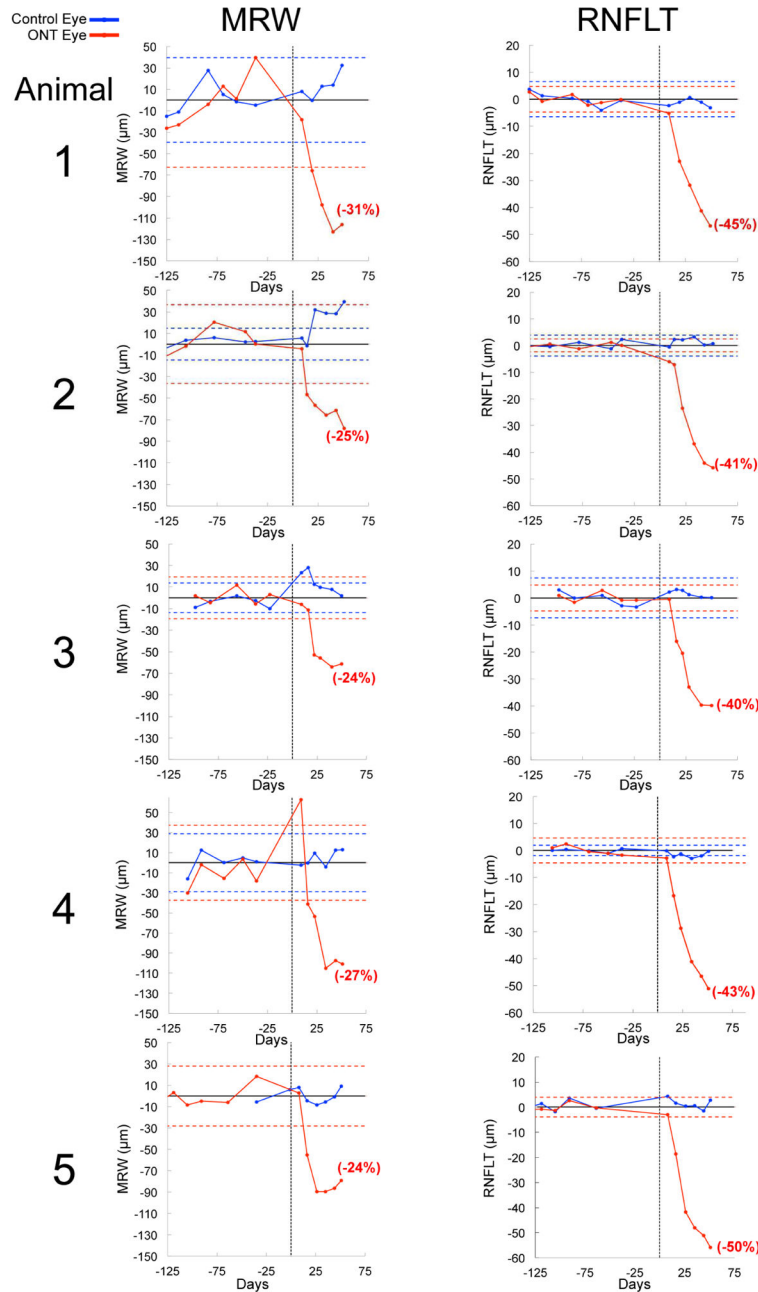


Figure 39. Optical Coherence Tomography (OCT) Global *Minimum Rim Width (MRW)* and *Retinal Nerve Fiber Layer Thickness (RNFLT)* Pre- and Post-Optic Nerve Transection (ONT) (Ing et al., 2016)

See section 4.0 for details. Data for both the ONT and control eyes are normalized to the baseline mean for that eye by subtracting the baseline mean value at each imaging time-point. For each animal, the following data is displayed: vertical dashed black line - day 0 = date of ONT; horizontal black line - for each eye zero change from its baseline mean value; horizontal dashed blue lines - the 95% confidence interval for the control eye based on the baseline sessions; horizontal dashed red lines - the 95% confidence interval for the (future) ONT eyes based on the baseline sessions. The percent change (calculated from the mean of

the baseline time-points) for *RNFLT* and *MRW* are listed in red parentheses for each ONT eye at their final imaging sessions. Negative values for *RNFLT* and *MRW* indicate thinning. Positive values for *RNFLT* and *MRW* indicate thickening. Note that a 95% confidence interval could not be generated for the control eye of Animal 5.

Reproduced from Ing, E., Ivers, K.M., Yang, H., Gardiner, S.K., Reynaud, J., Cull, G., Wang, L., Burgoyne, C.F., 2016. Cupping in the Monkey Optic Nerve Transection Model Consists of Prelaminar Tissue Thinning in the Absence of Posterior Lamina Deformation. *Invest Ophthalmol Vis Sci* 57, 2598–2611, under the CC BY-NC-ND 4.0 license (Ing et al., 2016).

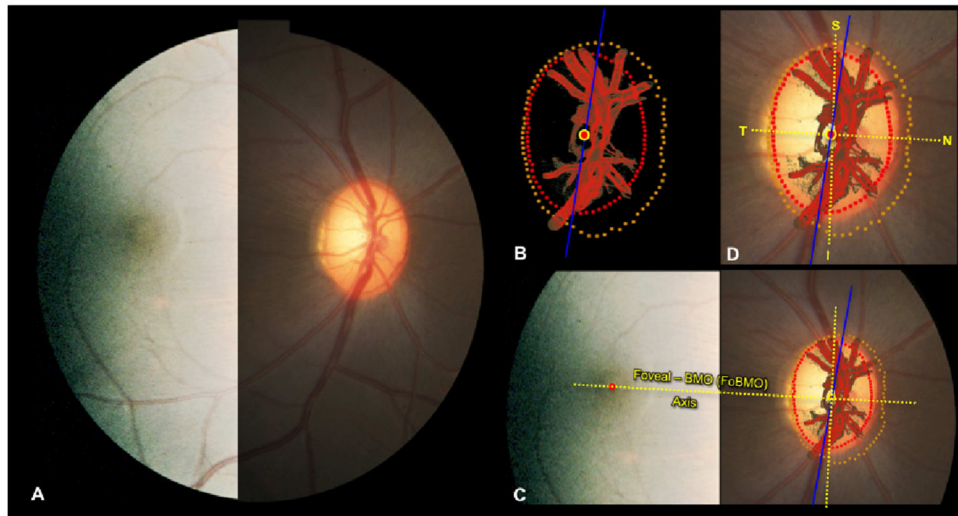


Figure 40. Estimating the Foveal-BMO (FoBMO) Axis Within the 3D HMRN BMO Reference Plane of Each ONH

See Section 5.1 for details. **(A)** A fundus photo, (here with brightness enhanced temporally to better see the fovea), confocal scanning laser reflectance image (not shown), or post-mortem fundus photo (not shown) was used to establish the axis between the fovea and the centroid of BMO for each eye as follows. **(B)** Delineated neural canal point clouds (Bruch's Membrane Opening (BMO) – red; Anterior Laminal Insertion (ALI) – Dark Yellow) and surfaced central retinal vessels (red) accompanied by the BMO centroid (red circle with yellow outline) and the embedded tissue block vertical (blue line) orientation are colocalized to the clinical fundus photo **(C)** using the vascular tree and BMO points (in this image BMO reference plane is slightly rotated out of the plane of the image to enhance visualization). The center of the fovea (red dot, **(C)**) is assigned to be the center of the dark foveal reflex or the center of the foveal capillaries. The axis connecting the center of the fovea to the BMO centroid (yellow with red center) is the FoBMO axis **(C)**. Using the FoBMO axis as the nasal temporal (horizontal) midline, a FoBMO vertical axis is established perpendicular to it **(C)** allowing anatomically consistent, FoBMO superior, inferior, nasal and temporal landmarks **(D)** within the BMO reference plane of each studied eye to be established. The regional characterization of LMA occurs within a reference plane based on the ALI insertion points (rather than BMO). The FoBMO vertical and horizontal axes are thus projected from the BMO reference plane to the ALI reference plane at the time of cylinderization (see Figures 23 and 24, and section 2.0). Finally, unlike OCT in which both the FoBMO centroid and Foveal center can be determined within OCT anatomy at the time of image acquisition (Chauhan and Burgoyne, 2013; Chauhan et al., 2015), the FoBMO axis within our 3D HMRNs is an estimate because the fovea is not included within the ONH trephine. Reproduced from Lockwood, H., Reynaud, J., Gardiner, S., Grimm, J., Libertiaux, V., Downs, J.C., Yang, H., Burgoyne, C.F., 2015. Lamina cribrosa microarchitecture in normal monkey eyes part 1: methods and initial results. *Invest Ophthalmol Vis Sci* 56, 1618–1637, with permission from the Association for Research in Vision and Ophthalmology (Lockwood et al., 2015).

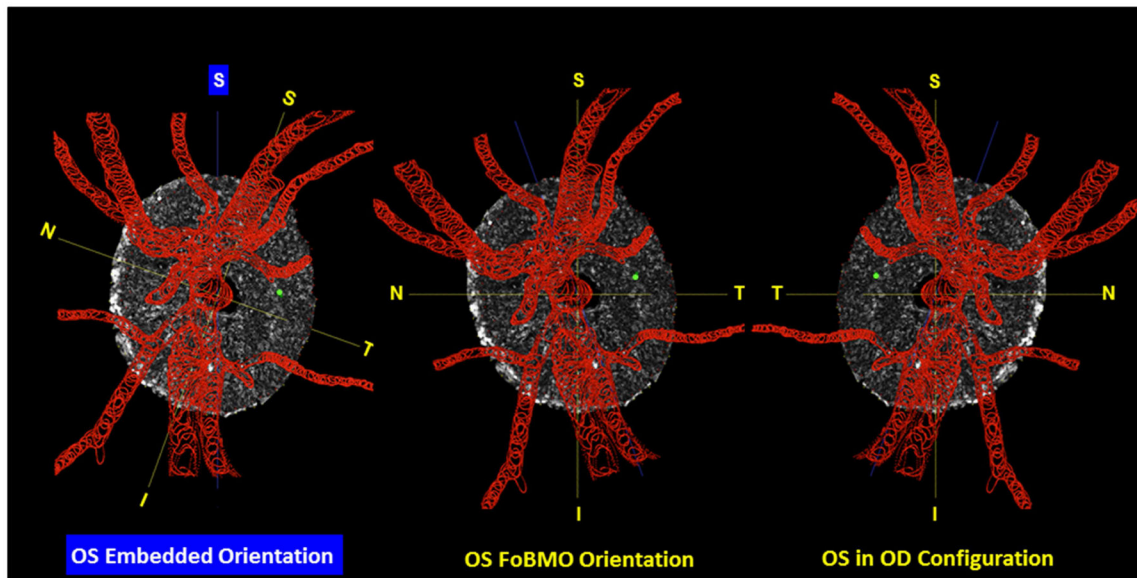


Figure 41. Converting Left Eye (OS) Segmented Lamina Cribrosa from “Embedded” to Foveal – Bruchs Membrane Opening (“FoBMO”) orientation and from Left to Right Eye (OD) configuration

See Section 5.1 for details. **(Left)** The FoBMO vertical axis is established relative to the embedded tissue vertical as depicted for a right eye in Figure 40, above. **(Middle)** The embedded data set is rotated (in this eye, counterclockwise 19.8° to bring the FoBMO vertical optic nerve head anatomy into the vertical coordinate position. **(Right)** FoBMO oriented left eye data is translated to FoBMO right eye configuration, by shifting the x axis location of each voxel to a position that is equal in distance but opposite in direction from the y (FoBMO vertical) axis while holding the y and z axis positions (not shown) constant. The position of a representative group of surface voxels is shown through each step of the process by a green dot.

Reproduced from Lockwood, H., Reynaud, J., Gardiner, S., Grimm, J., Libertiaux, V., Downs, J.C., Yang, H., Burgoyne, C.F., 2015. Lamina cribrosa microarchitecture in normal monkey eyes part 1: methods and initial results. *Invest Ophthalmol Vis Sci* 56, 1618–1637, with permission from the Association for Research in Vision and Ophthalmology (Lockwood et al., 2015).

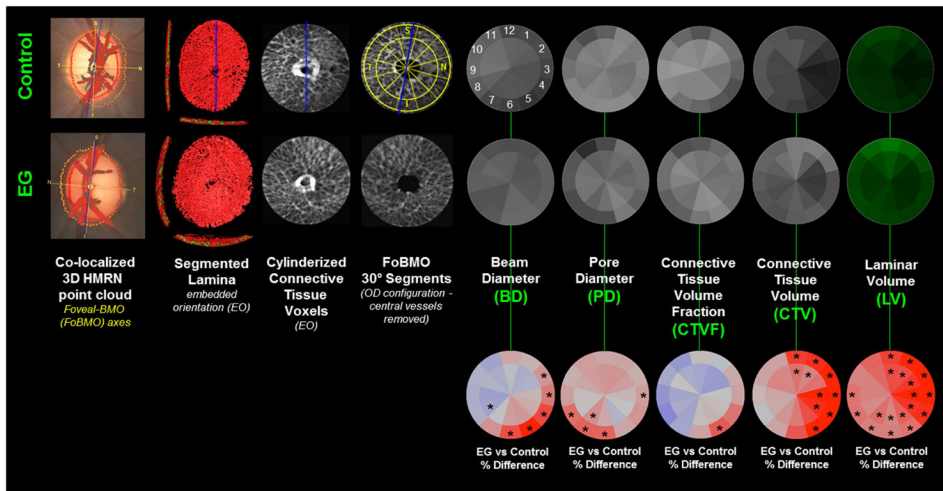


Figure 42. Foveal-BMO (FoBMO) Sub-Sectoral Laminar Microarchitectural (LMA) Change in Monkey early Experimental Glaucoma (EG) - Method Overview

See Sections 5.1 and 5.2 for details. **Upper two rows.** For both the control and EG eye of a representative study animal, the FoBMO axis (Figures 40 and 41) is determined and defined to be the nasal temporal axis of the Optic Nerve Head (ONH) 3D histomorphometric reconstruction (3D HMRN) relative to the embedded orientation (EO) of the tissues (embedded vertical axis depicted by blue line) by co-localizing the reconstructed vessels to a fundus photo (fovea not shown – see Figure 40). Lamina is isolated (not shown), the beams are segmented (**2nd column, details in Figure 21**) and each beam voxel and pore voxel have the associated diameter values assigned (Figure 22). Each voxel is then translated to a common cylinderized space (**3rd column, detail in Figures 26, 27**). The cylinder is rotated to establish FoBMO-oriented 30 degree (centered on the clinical clock-hours) sectors which straddle the FoBMO nasal-temporal and superior-inferior axes. All left eye data are converted into right eye orientation (**4th column, detail in Figure 41**). The three principal laminar microarchitecture outcome parameters are (**5th column**) *beam diameter (BD)* (with right eye, clock-hour, 30° sector designations) (**6th column**) *pore diameter (PD)* and (**7th column**) *Connective Tissue Volume Fraction (CTVF)*. Secondary volumetric outcome parameters include (**8th column**) *Connective Tissue Volume (CTV)* and (**9th column**) *Laminar Volume (LV)*. For all connective tissue and pore parameters, scaling is adjusted so that white suggests more and black suggests less connective tissue. *Laminar volume* is depicted in green because it is not related to connective tissue. All parameters are reported within 12 central and 12 peripheral FoBMO oriented 30 degree sub-sectors. **Bottom Row.** EG versus Control eye differences in each parameter and each sub-sector are reported in black font on a red (increased) or blue (decreased) background (color scales not shown). Asterisks (*) denote that the EG versus Control eye difference for this parameter exceeds the *maximum Physiologic Inter-eye Percent Difference Value (PIPDmax)* for that parameter in this sub-sector as determined by 6 bilateral normal animals, (data not shown, manuscript in preparation). Two separate analysis are not shown here, the first one considers inner (1/3), middle (1/3) and outer (1/3) laminal layers and the second only considers 12 sectors (sector analysis).

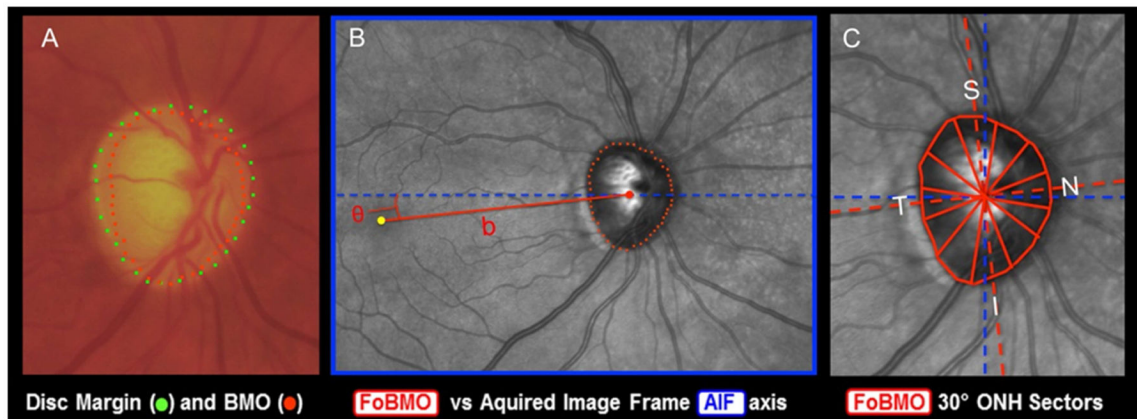


Figure 43. Optical Coherence Tomography (OCT) Phenotyping in the Monkey Experimental Glaucoma (EG) Model - Part 1: Bruch's Membrane Opening (BMO) and Foveal –BMO (FoBMO) Axis Anatomy vs the Clinical Disc Margin and the Acquired Image Frame (AIF) See Section 5.3 for details. **(A)** While in the monkey eye, OCT-detected BMO (red points) can be the same as the clinically visible Disc Margin (green points) (Strouthidis et al., 2009b), BMO can also be regionally invisible and anatomically different from the Disc Margin (Reis et al., 2012b; Strouthidis et al., 2009b). **(B)** The Foveal –BMO centroid (FoBMO) (red) vs *Acquired Image Frame* (AIF - blue) Temporal-Nasal axis (He et al., 2014a). **(C)** FoBMO ONH 30° sectors (He et al., 2014a). By colocalizing all forms of fundus imaging to the infrared image acquired at the time of OCT data set acquisition, FoBMO axis anatomy and regionalization can be superimposed upon all in-vivo and post-mortem data sets (Lockwood et al., 2015). Digitally converting all left eye data sets into right eye (OD) configuration, (Figures 40 and 41) and using FoBMO regionalization allows the most anatomically consistent EG vs. control eye comparisons within and between animals.

Reprinted from Exp Eye Res, 141, Burgoyne CF, The non-human primate experimental glaucoma model, 57–73, Copyright 2015, with permission from Elsevier (Burgoyne, 2015b).

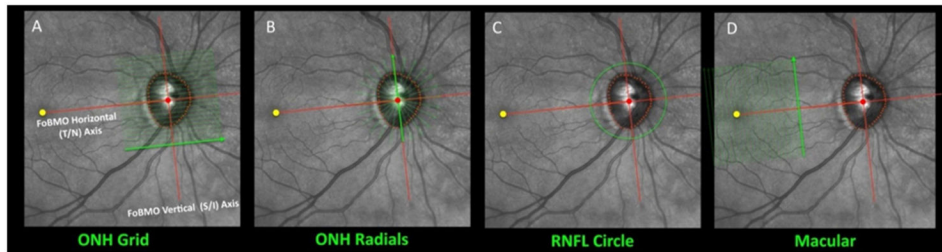


Figure 44. Optical Coherence Tomography (OCT) Phenotyping in the Monkey Experimental Glaucoma (EG) Model - Part 2: Acquisition of Optic Nerve Head (ONH), Retinal Nerve Fiber Layer (RNFL) and Macula data sets relative to the Foveal-Bruch's Membrane Opening (BMO) (FoBMO) Axis

See Section 5.3 for details. OCT acquisition software can now utilize eye-tracking technology (Helb et al., 2010) to automatically acquire ONH, (A and B) RNFL (C) and macula (D) images (datasets) relative to the OCT-detected FoBMO axis. This anatomy is determined the first time an eye is imaged and each A-scan of each subsequent scan (of the same scan type) are acquired in the same location. If an OCT device is utilized that does not have these features, post-hoc assignment of FoBMO anatomy and ONH regionalization can be accomplished (He et al., 2014a; He et al., 2014b; Lockwood et al., 2015). In our work we have chosen to emphasize radial B-scan data sets for the ONH (B) because we have shown it to efficiently capture ONH anatomy within 3D HMRNs and, in avoiding interpolation, allows improved signal to noise ratio through averaging 9 to 100 repetitions of each B-scan. Reprinted from Burgoyne C. The morphological difference between glaucoma and other optic neuropathies. *J Neuroophthalmol.* 2015;35 Suppl 1:S8–S21, with permission from Wolters Kluwer Health, Inc. (Burgoyne, 2015a).



Figure 45. Optical Coherence Tomography (OCT) Phenotyping in the Monkey Experimental Glaucoma (EG) Model - Part 3: Automated and manually-corrected *segmentation* for the Optic Nerve Head (ONH) rim (left and middle), Retinal Nerve Fiber Layer (RNFL, upper right) and Macula (lower right)

See Section 5.3 for details. A large literature now supports the concept of a minimum rim measurement made from BMO in humans and monkeys (Chen, 2009; He et al., 2014a; Patel et al., 2014a; Patel et al., 2014b; Povazay et al., 2007; Strouthidis et al., 2011). The logic for this approach has also been articulated (Chauhan and Burgoyne, 2013; Chauhan et al., 2013; Reis et al., 2012a). OCT manufacturers are now automatically segmenting BMO-MRW (left, and by clinical clock-hour - left middle), peripapillary RNFL (upper right) and macula (lower right) anatomy which can then be manually corrected and exported for analysis. Reprinted from *Exp Eye Res*, 141, Burgoyne CF, The non-human primate experimental glaucoma model, 57–73, Copyright 2015, with permission from Elsevier (Burgoyne, 2015b).

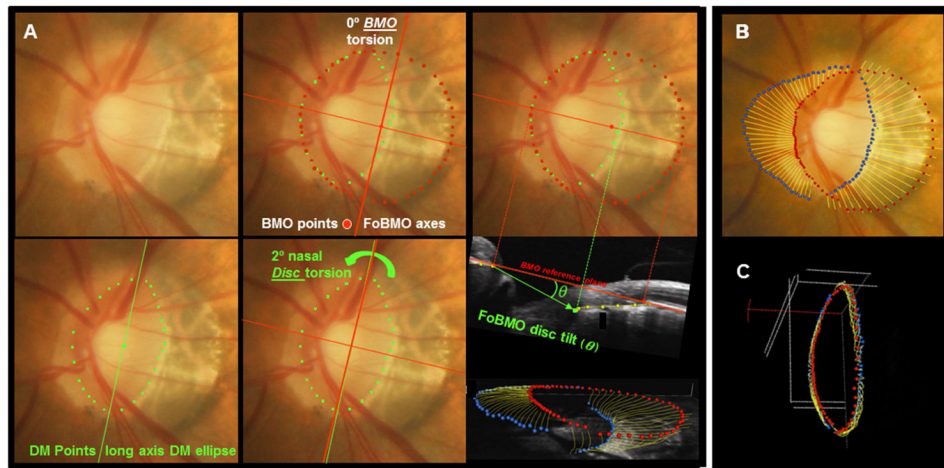


Figure 46. Optical Coherence Tomography (OCT) phenotyping of the Optic Nerve Head (ONH) Part 4: ONH tilt and torsion

See Section 5.3 for details. OCT definitions of ONH tilt and torsion are evolving and examples of how to define each are shown in (A). *Disc torsion* defines the angle of the long axis of the disc margin (DM) ellipse (marked by green dots) relative to the vertical foveal-to-Bruch's Membrane Opening (FoBMO) axis (A - lower center). *BMO torsion* defines the angle of the long axis of the BMO ellipse relative to the FoBMO vertical axis (A - upper middle) (because BMO is near to a circle, as indicated by the subtle red dots, it is hard to appreciate its long axis). *ONH tilt* defines the angle between a line connecting the nasal BMO point and the temporal OCT projection of the DM) within the FoBMO B-scan (A - lower right). The *neural canal minimum* defines the smallest cross-sectional area through which the retinal ganglion cell (RGC) axons pass enclosed by all BMO (red) and anterior scleral canal opening (blue) points (A - lower right, seen also in B and C). In (B) OCT delineated BMO points (again in red) and Anterior Scleral Canal Opening (ASCO) points (blue) are projected onto the colocalized disc photograph for reference. (C) However the 3D complexity of this anatomy can only be appreciated if these points are rotated in space to reveal the actual shape of the neural canal which is a slender oval (the smallest cross-sectional area of which represents the actual neural canal minimum, mentioned above). Reprinted from: Burgoyne CF, Ivers KM, Yang H, et al. OCT Anatomy for Glaucoma – Emerging Relationships of Interest. In: Optic Nerve Head and Retinal Nerve Fibre Analysis, 2nd Edition, Iester M, Lemij H, Garway-Heath D (eds). Italy: PubliComm. Forthcoming 2017.

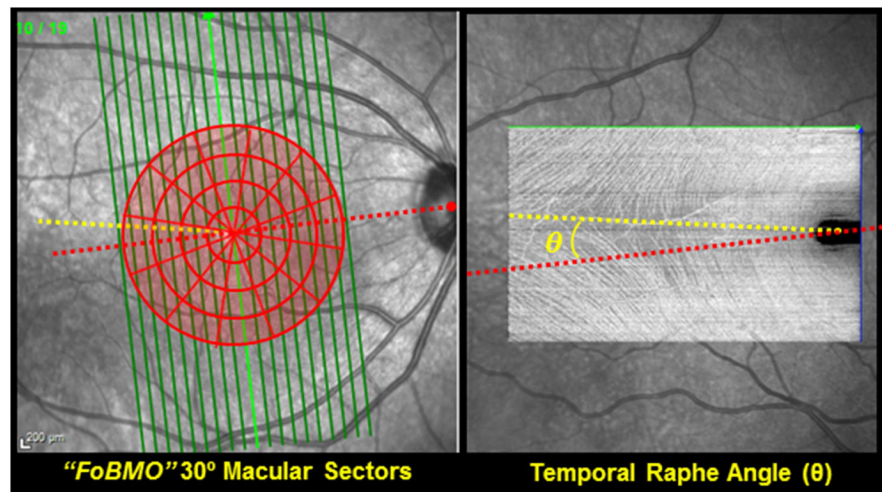


Figure 47. Optical Coherence Tomography (OCT) Phenotyping in the Monkey Experimental Glaucoma (EG) Model - Part 5: The Macula

See Section 5.3 for details. Automated Segmentation is available to make the following thickness measurements on most instruments: Nerve Fiber Layer (NFL), RGC complex (defined to be the distance between the internal limiting membrane (ILM) and the outer nuclear layer), RGC layer (RGC cell thickness, alone) and retinal thickness (ILM to Bruch's membrane thickness). When high density grid scans are obtained, the temporal raphe (yellow dotted line left and right) can be identified within "enface" (C-scan) views of the NFL (right) (Chauhan et al., 2014). The effect of using the temporal raphe versus the FoBMO axis as the "midline" for macula regionalization as well as multiple regionalization schemes (30° sectors & 500 micron intervals are shown - left) are being explored. Reprinted from *Exp Eye Res*, 141, Burgoyne CF, The non-human primate experimental glaucoma model, 57–73, Copyright 2015, with permission from Elsevier (Burgoyne, 2015b).

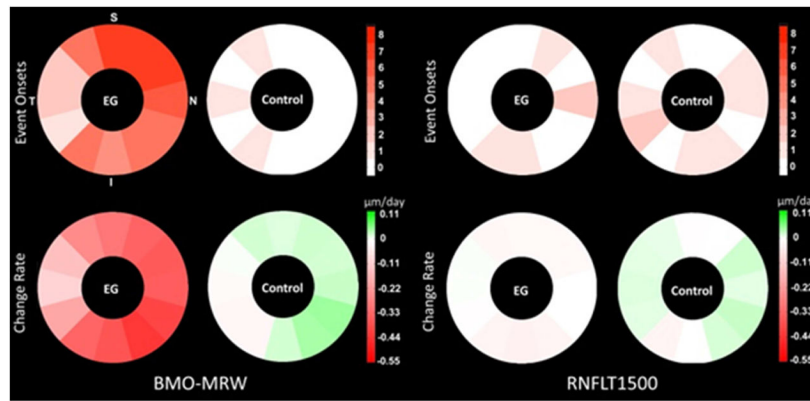


Figure 48. Foveal –Bruch’s Membrane Opening (FoBMO) 30° sectoral onset and rate data from the 8 Experimental Glaucoma (EG) eyes of our recent report (He et al., 2014b) confirm early Optic Nerve Head (ONH) onset and suggest Superior (S), Inferior (I) and nasal (N) ONH Susceptibility

See Section 5.4 for details. The number of event-based onset events (upper) and the average post-laser rate of change ($\mu\text{m}/\text{day}$) (lower) for OCT *Minimum Rim Width (MRW)* (left) and OCT *Retinal Nerve Fiber Layer Thickness (RNFLT)* (right) are shown. Note that while change events and rates are substantial for *BMO-MRW* in the EG eyes (left) change events and rates are absent or minimal for *RNFLT* (right). While change events and rates are greatest for *BMO-MRW* superiorly and inferiorly, nasal change is also substantial (Manuscript in Preparation (Yang et al., 2015b)).

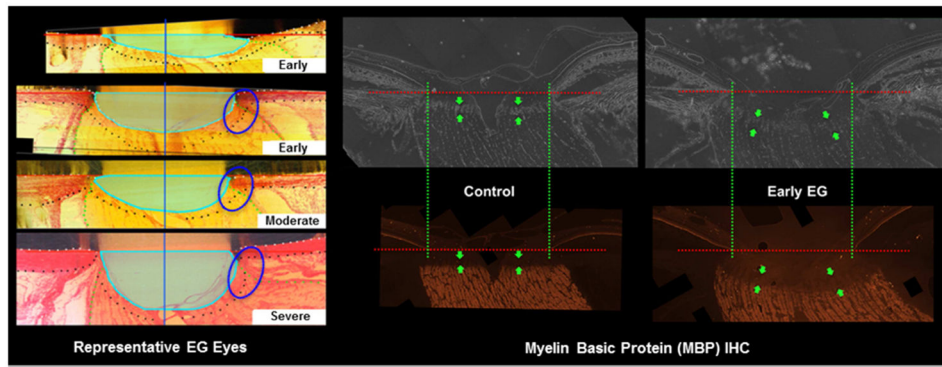


Figure 49. Optic Nerve Head (ONH) connective tissue deformation and remodeling is accompanied by decreased retrolaminar myelin basic protein (MBP) Immunohistochemistry (IHC) signal (right) early in the optic neuropathy of Monkey Experimental Glaucoma (EG) See Section 5.7 for details. **(Left)** 3D histomorphometric section images from the same 4 early-to-end stage glaucoma monkeys (Yang et al., 2015a) depicted in Figure 12, are used here to depict the extent of connective tissue deformation and remodeling throughout early to endstage monkey EG. In early EG, the lamina thickens in part because of new connective tissue synthesis (Reynaud et al., 2016) but also because retrolaminar orbital septa are “remodeled” into “new” posterior laminar beams in a process called “retrolaminar septal recruitment” (Roberts et al., 2009). It is thus in the outer lamina and retrolaminar myelin transition zone that the cell biology of connective tissue remodeling and myelin remodeling should overlap. **(Middle and Right)** Polarized (above) and red fluorescent IHC images (of the same section, below) for MBP demonstrate decreased EG eye retrolaminar optic nerve signal density (lower right) vs its Control eye in a monkey with -1.7% post-mortem EG eye axon loss. **Red lines** - Bruch’s Membrane Opening (**BMO**) reference plane. **Green lines** – BMO in the polarized and red light image of the same section. **Green Arrows** – lamina cribrosa. A total of 8 myelin related proteins demonstrate lower EG eye expression within the proteomics data described in Section 5.8. Retrolaminar EG eye decreased expression of three myelin related proteins has been confirmed by quantitative IHC as outlined in Section 5.9 (manuscript in preparation).

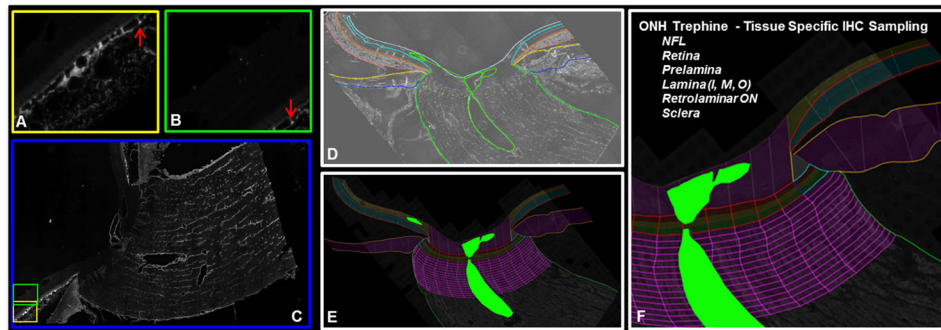


Figure 50. Quantitative Optic Nerve Head IHC

See section 5.9 for details. Each 10.0 mm ONH trephine is serial sectioned parallel to the Foveal-BMO (FoBMO) axis (Figure 40). Polarized (10×), blue, red, far red and green 40X primary images, are acquired (yellow (A) and green (B), boxes above - red arrows demonstrate overlap) using an autofocus algorithm to determine the best focal plane among 21 z-axis locations. (C) For each light source, 10× or 40× primary images (lower left with 10% overlap) are stitched into a composite image. (D) Standard ONH anatomic landmarks are manually delineated within the polarized light composite using published techniques, (Figures 13 and 14) allowing an anatomically consistent, tissue specific sampling box and vessel masking strategy (green (E) and (F)) to be identically imposed on the four individual color (antibody) images of each section. Inner (I), vs middle (M) vs outer (O) laminar and central vs peripheral comparisons are also undertaken.

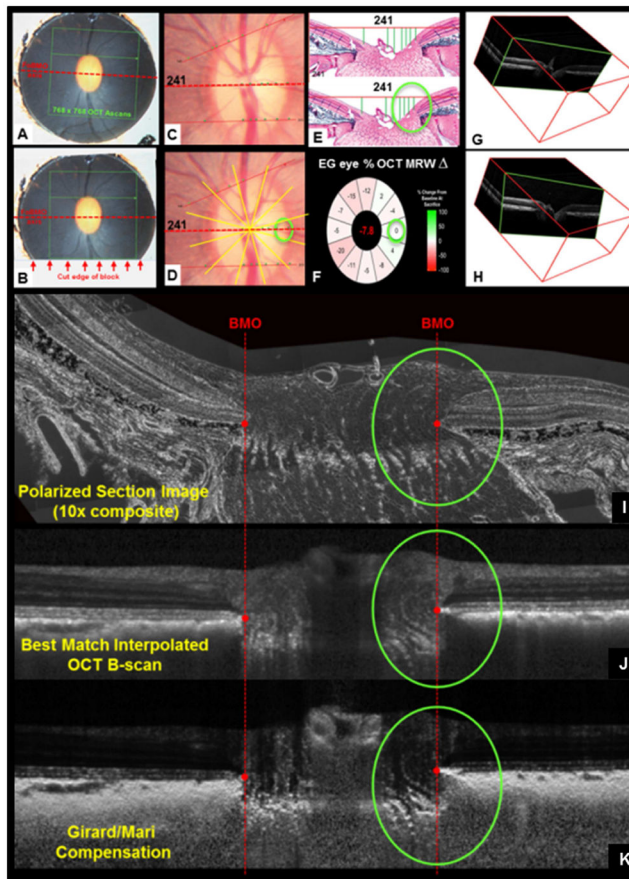


Figure 51. Optical Coherence Tomography (OCT) Co-localized Quantitative Immunohistochemistry (IHC) in Monkey early Experimental Glaucoma (EG)

See Section 5.9 for details. **(A)** Location of a sacrifice-day, high resolution (768×768 A scan grid) OCT data set acquired relative to the axis between the OCT-detected Bruch's Membrane Opening (BMO) and the fovea (the FoBMO axis). Here the outline of the grid has been projected onto the 10 mm post-mortem ONH trephine. **(B)** Serial paraffin (5µm) sections are cut parallel to the FoBMO axis. **(C and D)** Section 241 has been colocalized (red dotted line) using techniques outlined in previous publications (Strouthidis et al., 2010) and panel **(E)**. **(D)** Twelve FoBMO oriented 30° (clock hour) sectors are projected onto the disc photo, allowing the sectoral OCT longitudinal change data **(F)** to be estimated for the section to be studied. **(F)** Data are sacrifice-day percent change from baseline values for the OCT parameter *BMO-minimum rim width (MRW)* (He et al., 2014b). The green oval in **D**, **E** and **F** can also be linked to post-mortem optic nerve axons counts, which have also been regionalized relative to the FoBMO axis (not shown) (Reynaud et al., 2012). **(G)** and **(H)** Custom software generates "best-matched" interpolated B-scans from the OCT grid scan for each polarized light image (panel **I**). **(I – K)** Compositing polarized light image of a representative paraffin section (not section 241, shown in **(E)**) along with the best-matched interpolated B-scan **(J)** and the Girard/Mari adaptive compensation version (Mari et al., 2013) of the same B-scan with enhanced visualization of the deep ONH tissues **(K)**. Once target protein signal density is determined within a given paraffin section, longitudinal

change in the anatomy of that section can be determined within equivalent OCT best-matched sections from each baseline (pre-laser) and post-laser imaging session up to and including the sacrifice day images shown above. Comparisons between protein expression and anatomic change in the EG eyes can then be compared to Control eyes, to seek links between clinically detected OCT structural change and protein expression signal density change in monkey EG.

Author Manuscript

Author Manuscript

Author Manuscript

Author Manuscript

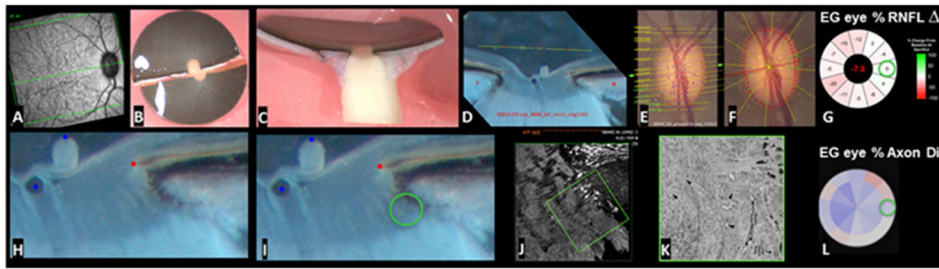


Figure 52. Optical Coherence Tomography (OCT) Co-localized Quantitative Scanning Block Face Electron Microscopy (SBFEM) in Monkey early Experimental Glaucoma (EG)

See sections 5.10 for details. **(A)** The OCT detected Foveal-BMO (FoBMO) axis (green line) (Figures 43–44) extends from the OCT-determined center of the fovea (not visible) through the OCT-determined center of BMO (green points). **(B)** Manual transection of the perfusion fixed 10.0 mm ONH trephine along a line approximating the FoBMO axis. **(C)** The cut surface of superior hemi-trephine. **(D)** Vibratome section (100 μm) cut parallel to the cut surface. For each vibratome section, BMO points (red dots) and vessel locations (blue dots) are projected to the BMO reference plane (here shown as a parallel yellow line floating above) and used to identify the section's precise location within a disc photo (for this section, green arrows in **(E)**). **(F)** Colocalizing OCT FoBMO sectors to the disc photo (He et al., 2014a) allows comparison to longitudinal OCT RNFL thinning (0% for this clock-hour). **(H)** Close up of the nasal (N) side of the scleral canal (red dot - BMO), (blue dot – vessel and Burgemeisters papilla - visible in photo but not at this magnification). The lamina and its insertion are faintly visible. **(I)** (estimated) location of the SBFEM reconstruction to include the posterior lamina and retrolaminar (myelinated) optic nerve. **(J)** A microscopic x-ray computed tomography (μCT) movie of the entire vibratome section (500 serial optical scans) used to finalize the location (green box) of the SBFEM reconstruction. **(K)** Transmission EM (TEM) of the block face at the starting point of SBFEM reconstruction. **(L)** FoBMO sectoral EG vs Control eye axon count differences (-8.8% for this sector, green circle) will be determined for each EM-studied, early EG monkey. EM measures of axon cytoarchitecture disruption will be quantified within each studied ONH sector.

Table 1

Commonly Used Abbreviations/Acronyms/Terms and their Description

| Acronyms/Terms | Meaning/Definition |
|------------------------|---|
| 3D | Three dimensional |
| ALCSD | Anterior lamina cribrosa surface depth |
| ALI | Anterior laminar insertion |
| Animal-Specific | Animal-specific EG vs Control eye difference |
| BD | Beam diameter |
| BM | Bruch's membrane |
| BMO | Bruch's membrane opening |
| Control Eye | Contralateral control eye of a unilateral optic neuropathy study animal – not assumed to be “normal” |
| CSFp | Cerebrospinal fluid pressure |
| CSLT | Confocal scanning laser tomography |
| CTV | Connective tissue volume – the sum of all connective tissue voxels |
| CTVF | Connective tissue volume fraction – the ratio of <i>CTV/LV</i> expressed without units |
| EG | Experimental glaucoma |
| FoBMO | Axis between the foveal center and the $BMO_{centroid}$ |
| Global Data | Data for a single ONH that includes all sectors, sub-sectors and depths |
| HMRN | Histomorphometric reconstruction |
| IHC | Immunohistochemistry |
| IOP | Intraocular pressure |
| LC | Lamina cribrosa |
| LMA | Lamina cribrosa microarchitecture – as characterized by <i>BD, PD, CTV, CTVE, LV</i> |
| LV | Lamina cribrosa volume – the sum of all beam and pore voxels |
| mfERG | Multifocal electroretinography |
| MPD | Mean position of the disk, CSLT parameter – average position of the ONH ILM relative to CSLT ref plane |
| MRW | Minimum rim width |
| Normal Eye | An eye that has no evidence of disease and is not the unilateral control for a contralateral intervention |
| OCT | Optical coherence tomography |
| ONH | Optic nerve head |
| Overall Data | Data from all monkeys considered together, i.e. experiment wide results |
| PD | Pore diameter |
| PID, PIDmax | Physiologic inter-eye difference (Difference between the two eyes of a bilaterally normal monkey), and the maximum value of this difference among a group of bilaterally normal monkeys |
| PIPD, PIPDmax | Physiologic inter-eye percent difference, and its maximum value among a group (see PID, above) |
| PLI | Posterior laminar insertion |
| pp-sclera | Peripapillary sclera |
| RGC | Retinal ganglion cell |
| RimV | Rim volume |
| RNFL | Retinal nerve fiber layer |

| Acronyms/Terms | Meaning/Definition |
|----------------|-------------------------------------|
| RNFLT | Retinal nerve fiber layer thickness |
| RPE | Retinal pigment epithelium |
| SLP | Scanning laser polarimetry |

Note that all *parameters* are italicized so as to distinguish them from the anatomic landmark or structure or phenomenon they measure

Author Manuscript

Author Manuscript

Author Manuscript

Author Manuscript